UNIVERSITÀ DEGLI STUDI FIRENZE

PhD in
Atomic and Molecular Photonics

CYCLE XXXVII

Coordinator: Prof. Diederik Wiersma

# Quad-SPIM: a novel light-sheet microscope for high-throughput imaging of human brain tissue

Academic discipline (SSD) FIS/03


Doctoral Candidate

**Franco Cheli**

Supervisor

**Prof. Francesco Saverio Pavone**

Coordinator

**Prof. Diederik Wiersma**

Co-Supervisor

**Prof. Francesco Vanzi**


Years 2021/2024

# Quad-SPIM: a novel light-sheet microscope for high-throughput imaging of human brain tissue

# Table of Contents

# 1. Abstract

Light-sheet fluorescence microscopy (LSFM) represents a crucial advancement in the field of optical imaging, enabling high-resolution and fast imaging with minimal photodamage. This doctoral research focuses on the development and characterization of a novel quad-SPIM (Selective Plane Illumination Microscopy) system, which demonstrates significant enhancements in imaging speed, resolution, and multicolor capabilities. The quad-SPIM system achieves a 12-fold increase in imaging speed compared to previous dual-SPIM systems, allowing for volumetric imaging of human brain tissue at a rate of 2.1 $cm^3/h$ in four different fluorescence channels. This improved speed is crucial for large-scale studies of human brain tissue, facilitating comprehensive neural circuit mapping and accelerating research into neurodegenerative diseases.

The system's capacity for simultaneous multicolor imaging, with lateral and axial resolutions in the range of 2.6 μm to 3.9 μm, further enhances its utility in detecting multiple biomarkers within complex biological samples. Applications of this system include the study of fiber dispersion in brain tissues, tracing neuronal pathways, and understanding cellular interactions. This research not only addresses the current challenges in high-throughput imaging but also opens the way for future innovations in large-scale biological studies.

# 2. Introduction

Light-sheet fluorescence microscopy (LSFM), also known as selective plane illumination microscopy (SPIM), represents one of the most significant advancements in optical imaging of the last two decades. Differently from traditional microscopy techniques, LSFM illuminates the specimen with a thin sheet of light, recording images one plane at a time, drastically reducing photodamage and photobleaching while providing high-resolution and high signal-to-background images. This innovative approach allows scientists to study living organisms over time with minimal impact on their biological processes. The development of this technique and its increasing customization, have revolutionized the fields of developmental biology, neurobiology, and various other disciplines where the dynamics of living systems are studied at cellular and subcellular levels.

The origin of LSFM dates back to the early 20th century, when Siedentopf and Zsigmondy (1903) introduced their "Ultramicroscope" (Figure 1), but it was only in the early 2000s that the technique was adopted for broad biological application. The first major breakthrough came with the development of a method that combined thin light sheets with digital microscopy, allowing for high-resolution imaging of live zebrafish embryos (Huisken et al. 2004). Since then, advances in optical technologies, digital sCMOS sensors, and fluorescent probes have further increased the capabilities of LSFM. Modern implementations, such as digitally scanned light sheets (Keller et al. 2008) and dual-objective configurations (Tomer et al. 2012), have enhanced the resolution, contrast

and speed, enabling complex, volumetric imaging of fixed samples or biological processes in real-time.

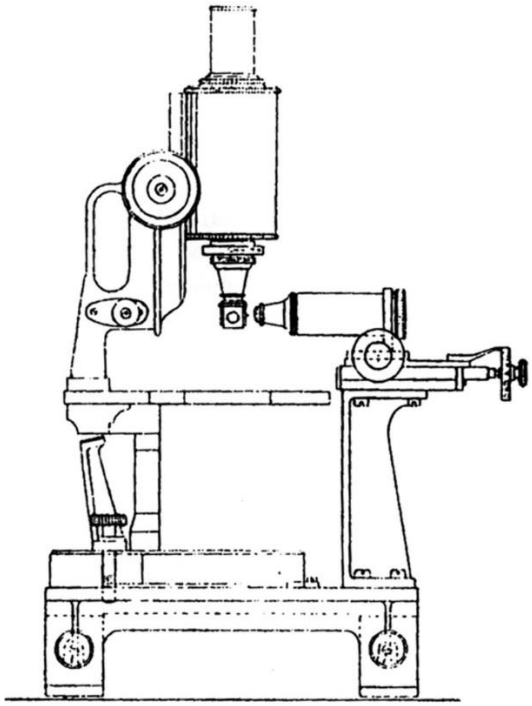

*Figure 1. Siedentopf and Zsigmondy's Ultramicroscope.*

While confocal microscopy has been the state-of-the-art technique for decades, LSFM offers several advantages that make it preferable for specific scientific studies. Firstly, LSFM minimizes light exposure outside the focal plane, making it optimal for live imaging, where temporal resolution and low photobleaching are crucial. In fact, light sheet microscopy provides both rapid imaging and volumetric data acquisition, making it particularly well-suited for capturing dynamic biological processes. In addition, the orthogonal illumination approach of LSFM enables deeper tissue penetration with lower light scattering, making it ideal for reconstructing large volumes of thick specimens (Santi 2011; Power and Huisken 2017).

Recent innovations in LSFM technology include the development of miniaturized and automated systems that expand its usability in diverse research settings, from large-scale bioimaging facilities to smaller laboratory environments. The introduction of adaptive optics, like liquid lenses, in LSFM setups has addressed issues of optical aberration caused by heterogeneous tissue composition, significantly improving image quality in deeper tissue layers (Hampson et al. 2021). Additionally, advancements in computational methods for image reconstruction and real-time processing, especially with the advent of machine learning and neural networks, have allowed researchers to handle typically large datasets of LSFM with greater efficiency (Keller et al. 2008).

The application of LSFM had a deep impact on studies requiring the observation of living cells and tissues over time. Its ability to image samples with minimal photodamage is essential for prolonged studies of developmental biology, such as embryogenesis and organogenesis. Moreover, LSFM revealed to be decisive in neuroscience, where it allowed the detailed mapping of neural circuitry and brain activity in live animals and fixed samples (Chen et al. 2014; Power and Huisken 2017) as well as brain vasculature (Spangenberg et al. 2023). In addition, animal and human cleared brain tissue can be studied at sub-micron resolution, revealing new insights into our knowledge of the brain and critical diseases affecting the nervous system (Di Meo et al. 2024a; Pawłowska, Legutko, and Stefaniuk 2017; Corsetti, Gunn-Moore, and Dholakia 2019).

As LSFM continues to evolve, efforts are concentrated on increasing the imaging depth and resolution, expanding the range of detectable fluorophores, and therefore its applicability. One of the main challenges remains ability to image very large or densely packed specimens, where light scattering and absorption can degrade image quality. The use of multi-photon excitation and non-linear optics may hold the key to overcoming these obstacles (Reynaud et al. 2008). In addition, the integration of LSFM with other imaging modalities, such as magnetic resonance imaging (MRI) and positron emission tomography (PET), offers a multimodal approach to the study of biological structures and functions (Johnson et al. 2023).

This work will report the development of an innovative light-sheet microscope which is able to image large human brain cleared tissue with different wavelengths simultaneously, thus allowing to investigate various various structural characteristics of the sample under examination with micrometer resolution and very high throughput.

## 2.1 Light-sheet fluorescence microscopy. Setup examples and state-of-the-art

### 2.1.1 Light-sheet fluorescence microscopy: an overview

Since its invention in 1903, when Siedentopf and Zsigmondy introduced the technique for the first time in their study "Über Sichtbarmachung und Größenbestimmung ultramikroskopischer Teilchen, mit besonderer Anwendung auf Goldrubingläser.", light sheet microscopy has undergone significant advancements, turning into a powerful tool for biological imaging.

LSFM revealed as a very versatile imaging technique, which can be implemented implemented in already-existing systems or custom-made setups and may be employed in a multitude of studiesto fit specific research requirements.

In a basic setup, the primary light source in a light-sheet microscope is usually a laser beam. The laser light passes through a cylindrical lens, which shapes the beam into a thin sheet, which is usually about a few micrometers thick and illuminates the sample orthogonally to the direction of observation. This orthogonal arrangement is a peculiar characteristic of light-sheet microscopy and is crucial to achieve high-contrast images with reduced background noise, as only the plane of interest is illuminated, and the emitted fluorescence is collected from this plane only (Figure 2).

After the light sheet is generated, it is directed towards the sample via an objective lens, which focuses the light onto the specimen. The sample is usually embedded in a medium that matches its refractive index, reducing light scattering and aberrations that could otherwise degrade image quality. The sample is typically mounted on a motorized stage that can move linearly and/or rotate, allowing for the sequential illumination of multiple planes as the sample moves through the stationary light sheet. This sequential imaging of successive planes allows the reconstruction of a three-dimensional image of the specimen.

The detection pathway in a light-sheet microscope is positioned at a right angle with respect to the illumination plane, typically involving a second objective lens that collects the fluorescence emitted from the illuminated

plane. The collected fluorescence is then directed to a sensitive camera, often a charge-coupled device (CCD) or a scientific complementary metal-oxide-semiconductor (sCMOS) camera, which captures the image. The use of such high-sensitivity cameras is crucial, as they enable the detection of weak fluorescence signals while maintaining the frame speed necessary for capturing dynamic biological processes.

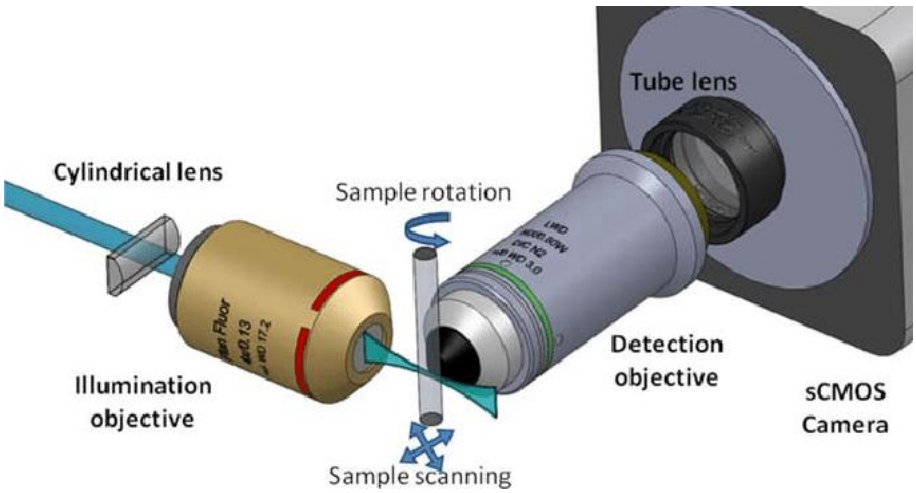


*Figure 2. Basic setup of a light-sheet microscope. (Olarte et al. 2018)*

The setup of a light-sheet microscope also typically includes several components, like adaptive optics, designed to precisely control the light sheet and the stage. In addition, dedicated software is used to control the movement of the stage, synchronizing it with the light sheet and camera

trigger, and to process the images to reconstruct the 3D volume of the specimen.

### 2.1.2 Illumination and detection paths

When focusing a Gaussian beam in the illumination path through the cylindrical lens-objective system, the axial resolution of the LSFM can be related to its beam waist ($2\omega_0$), so that the resulting axial resolution can be defined as:

$$R_{ill\text{-}axial} = 2\omega_0 = 2\frac{\lambda f}{\pi D} = 2\frac{n\lambda}{\pi NA} \qquad (1.1)$$

Where $2\omega_0$ represents the beam waist, $\lambda$ is the wavelength of light, $f$ is the focal length of the illumination lens, D is the beam diameter before the lens, NA is the numerical aperture of the lens and n is the refractive index of the medium.

In a focused Gaussian beam propagating in its fundamental transversal mode ($TEM_{00}$), the Rayleigh range $Z_R$ is defined as the distance along the propagation axis from the beam waist (the location of the smaller beam diameter) to the point cross-sectional area of the beam has increased by a

factor of $\sqrt{2}$ and can be related to the real FOV of the imaging system by defining the Rayleigh range $Z_R$ and the confocal parameter $b = 2\,Z_R$:

$$\text{FOV} = b = 2Z_R = 2\frac{\pi\omega_0^2}{\lambda} \qquad (1.2)$$

which also corresponds to the full width at half-maximum (FWHM) of the intensity profile of a Gaussian beam along its propagation axis (Figure 3).

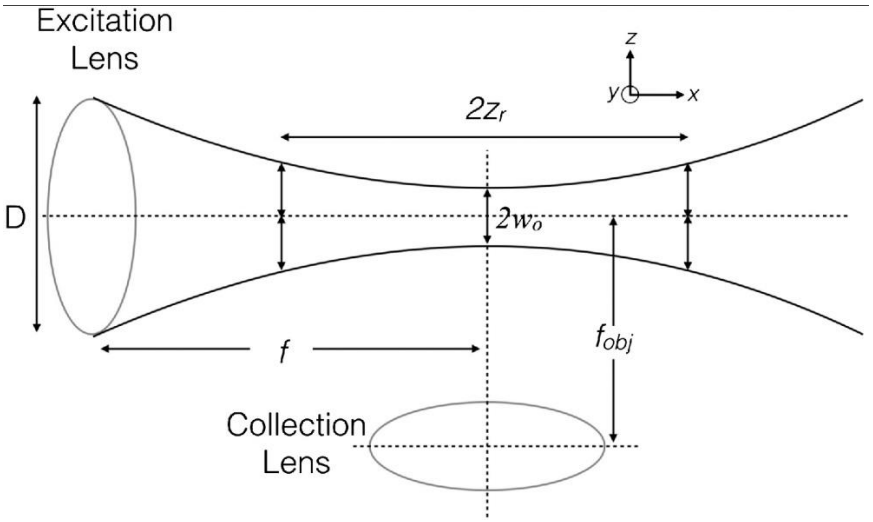


*Figure 3. Schematic illustration of a focused Gaussian beam profile used as illumination beam in a LSFM. (Olarte et al. 2018)*

The lateral resolution of the system is defined by the characteristics of the detection objective lens and can be defined by the Rayleigh criterion as:

$$R_{\text{det-lateral}} = \frac{0.61\,\lambda_{em}}{NA_{det}} \qquad (1.3)$$

Where $NA_{det}$ is the numerical aperture of the detection objective.

The axial resolution of the detection objective is defined as:

$$R_{\text{det-axial}} = 1.78\,\frac{n\lambda_{em}}{NA_{det}^2} \qquad (1.4)$$

According to the above considerations, the resulting axial resolution of the system must be a convolution of the axial resolution (PSF) of the illumination focused beam defined by (1.1) and the detection objective axial resolution defined by (1.4). As a result, the final resolution of the system is improved when the illumination lateral resolution exceeds the detection objective axial resolution.

In addition, it has to be noted that the illumination beam waist (and consequently the axial resolution) and the FOV, represented by the confocal parameter *b*, are inversely proportional according to (1.2) and depend on the incident beam diameter D on the back focal plane of the illumination optics. As a consequence, optimizing the system FOV and axial resolution remains a challenging task.

### 2.1.3 Resolution optimization in LSFM.

In a LSFM setup, matching the lateral resolution with the axial resolution represents an optimal imaging condition. However, shaping a focused Gaussian beam into a light-sheet thin enough to match the lateral resolution of the microscope, comes at the cost of a field of view reduction. This is especially evident when the detection objective's NA is

much higher than the one of the illumination objective. Conversely, when the detection objective's NA is smaller than the illumination one, it is impossible to generate an illumination beam which could fill the entire FOV of the detection objective.

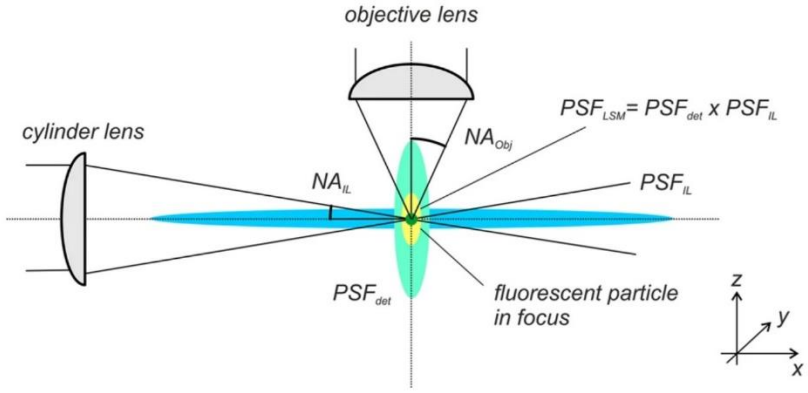


*Figure 4. LSFM point spread function resulting from the convolution of of the illumination PSF and detection PSF. (Becker et al. 2019)*

Figure 4. shows how the PSF of the microscope is the result of the interaction of the PSF of the illumination objective and the PSF of the detection objective. As a consequence of (1.1) and (1.2), obtaining a $2\omega_0$ of the same thickness as the lateral resolution of the detection objective extending for its entire FOV = $2z_R$, is a complex task, in particular when using Gaussian beams and linear excitation. This is especially true when dealing with the objectives' physical encumbrance and working distance. All of these factors imply the usage of high NA, long working distance objectives with correction collars for refractive index mismatch correction within the desired range, according to the immersion medium surrounding the sample. All these characteristics are unlikely to be found in commercially available objectives designed for other imaging techniques such as two photon microscopy or super resolution microscopy. This leads researchers to contact suppliers of expensive custom optics or to buy out-of-the box commercial systems. Only in recent years, the major companies

have started to offer turn-key systems and dedicated objectives specifically engineered for high-performance LSFM.

However, using non-diffractive beams like Bessel beams or multiphoton excitation are very effective ways to reach isotropic resolution and large FOV in LSFM at the expense of a major system complexity and higher costs (Truong et al. 2011).

### 2.1.4 Refractive index (RI) matching

The main advantage of LSFM consists of its ability to image large samples. In order to eliminate spherical aberrations and its detrimental effects on image quality, the optical path between the objectives and the sample requires a continuity in refractive index (RI). This implies that all the elements in the optical path must match the refractive index of the sample and the objectives must be designed to perform at that specific refractive index, and eventually provided with a correction collar to match a range of RI values. Therefore, the refractive index of the immersion media in the specimen chamber and/or holder, as well as the materials of the specimen holders, also need to follow this principle. Thus, the choice of the objectives and all the elements in the imaging optical path is a consequence of the refractive index matching medium the sample is immersed in as a result of the tissue clearing technique (Rocha et al. 2019; Di Meo et al. 2024; Boothe et al. 2017; Machacova et al. 2021).
In a common LSFM design, the illumination and detection objectives are suited for immersion in different media within a specific range of RI values and are sealed in the imaging chamber with leak-proof gaskets.

The sample is directly immersed in the imaging medium and is held in the chamber of the medium or, more commonly, in a transparent cuvette or thin capillary tube containing the RI matching medium used in the clearing process. The type of glass, quartz, or other transparent material the specimen holder is made of, must also match the RI of the surrounding media (Russell and Rees 2020; Desmaison et al. 2013; Laroche et al. 2019). In most scenarios, imaging chambers and specimen holders, as well as tissue clearing techniques and immersion media involved, are custom

optimized to match the type of tissue and research being performed (Figure 5).

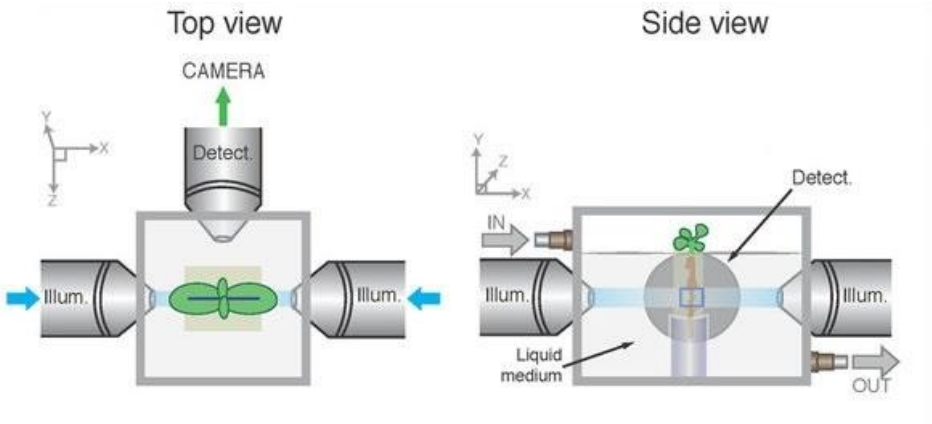


*Figure 5. Schematic of a dual-illumination setup LSFM for imaging living plant seedlings (Berthet and Maizel 2016).*

A mismatch of the RI value in the optical path would arise as serious spherical aberrations as its entity, causing a deterioration in image quality and eventually the impossibility to correctly focus the specimen, in particular as moving further in depth into the specimen, where the effects of spherical aberrations sum to the effects of light scattering by the specimen itself (Hedde et al. 2017).

### 2.1.5 LSFM setups' examples and variations

In recent times, researchers have been developing a large variety of light-sheet microscopes setups and variations from the basic configuration described in 2.1.1 to fit their research requirements. Most of the solutions aim to increase the resolution, in particular axial resolution, while maintaining a large field of view. As described above, axial resolution in LSFM is strictly dependent on light-sheet thickness. Consequently, the use of non-gaussian beams like Bessel beams, two-photon excitation, lattice light-sheets or axial scanning have been implemented to improve axial resolution and obtain, in an ideal scenario, isotropic resolution

(Takanezawa, Saitou, and Imamura 2021; Fahrbach et al. 2013). In addition, multi-view and/or multi-illumination imaging (Figure 6) and deconvolution can also be used, and eventually mixed with the aforementioned techniques. Digitally-scanned light-sheets are also commonly used, in combination with modern sCMOS cameras featuring a rolling shutter, to improve image contrast in the so called “confocal slit configuration”.

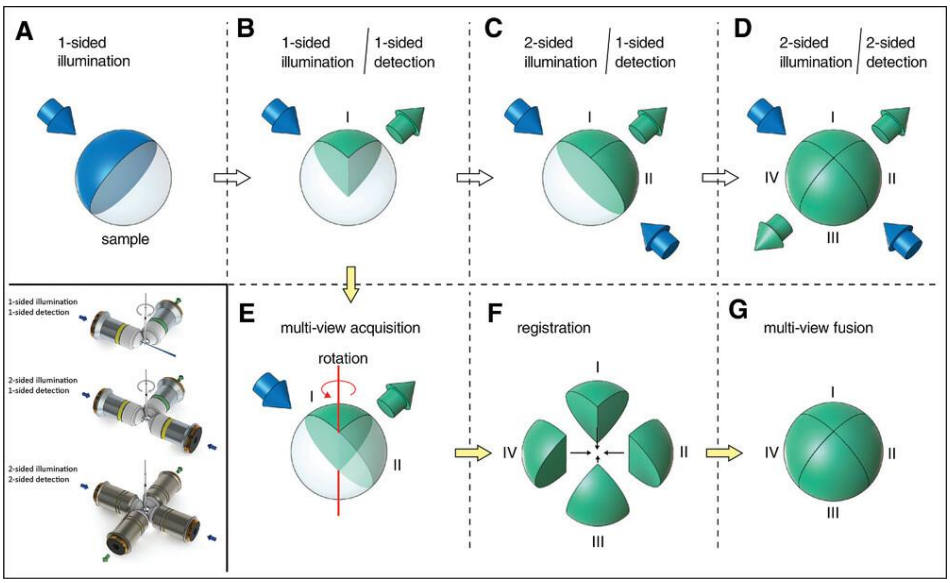


*Figure 6. Multi-view light-sheet microscopy solutions. (A) Lateral illumination of the sample. (B) Basic one-sided illumination and one sided detection. (C) Two-sided illumination is a convenient way of reducing striping artifacts caused by the presence of more dense objects in the sample. (D) Two-sided illumination/detection reduces the image deterioration due to light scattering in thick samples by acquiring half of the sample from each detection objective. (E,F,G) Rotating the sample on its y axis generates a multi-view fused image with increased resolution. (Dyer et al. 2022)*

Imaging speed is also a big concern when a large number of samples need to be acquired or when the size of the samples is particularly big (eg. samples processed with expansion protocols, Pesce et al. 2024; Daetwyler and Fiolka 2023). Therefore, multicolor simultaneous imaging plays an important role in speeding up the acquisition process.

When imaging small samples like live cells, and a very thin light-sheet is required, many custom solutions have been developed which include the use of two high NA objectives, one for generating the light-sheet and the

other for the detection, or a single objective which generates the sheet and detects fluorescence at the same time (Figure 7).

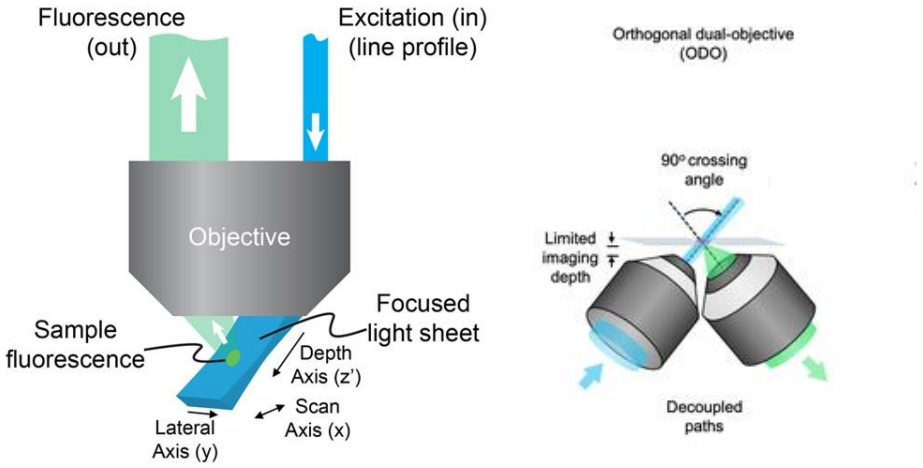


*Figure 7. (Left) Illumination and detection with one single objective and (right) two objectives in an open-top configuration. ('3D Imaging at the Speed of Life with SCAPE Microscopy | Coherent', n.d.; A. Glaser et al. 2020)*

*Digitally scanned LSFM.*

Above all, digitally scanned lateral light sheets, have been one of the major innovations which have hugely spread in laboratories and can be considered the state-of-the-art of LSFM. In such setups, the light sheet is

formed by scanning a thin beam across the whole FOV of the detection objective in synchronous with the rolling shutter of the camera (Figure 8).

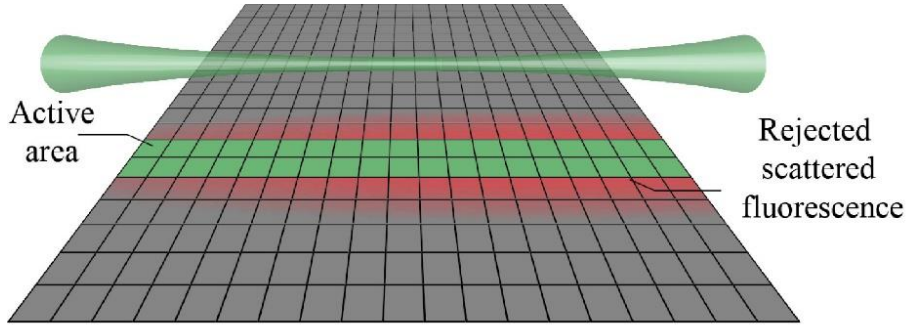


*Figure 8. LSFM confocal slit: camera exposes one or few rows of pixels synchronised with a swept beam. (Marcos-Vidal and Ripoll 2020)*

As a result, only the fluorescence from the thinnest and highest intensity illumination region is recorded by the camera, eliminating the detrimental contribution of out-of-focus and scattered light coming from the outer

regions of the illumination beam, thus increasing image contrast (Marcos-Vidal and Ripoll 2020).

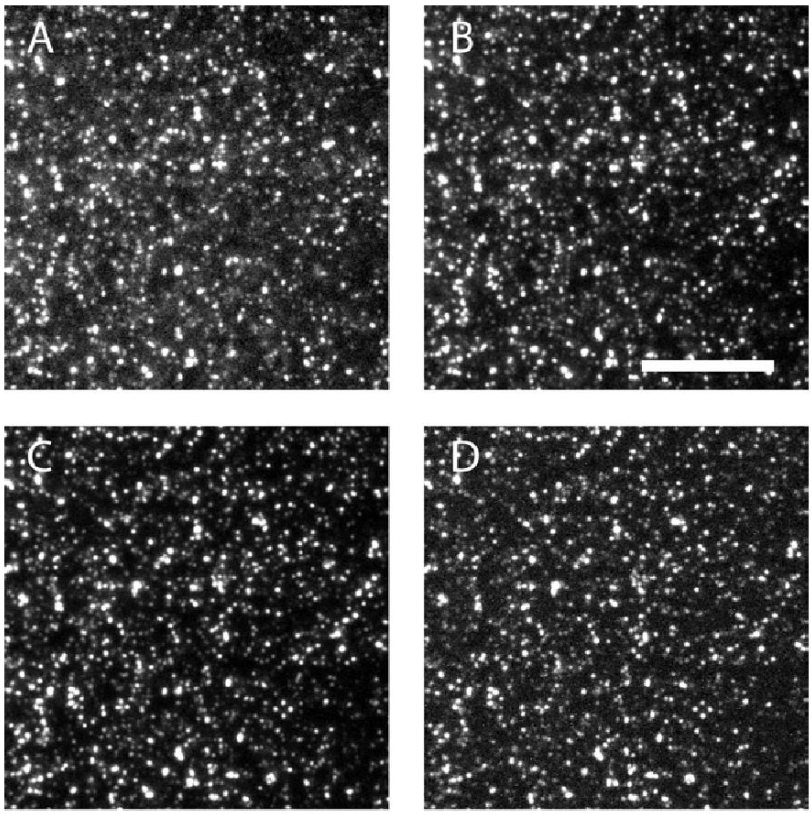


*Figure 9. Imaging agarose-embedded fluorescent beads. Comparison between global shutter (top) and respective confocal slit recording, showing increased signal-to-background (bottom). Scale bar: 50 μm. (Baumgart and Kubitscheck 2012)*

*Axially scanned LSFM.*

Axially swept light-sheets can also be used to obtain a slit-scanning setup and increase the signal-to-background. One possible approach is the use of electronically tunable lens (ETLs) to sweep the beam waist of a cylindrical lens generated light-sheet synchronously with the camera

rolling shutter (Figure 10). However, tunable lens are prone to spherical aberrations due to surface deformation and when their optical axis is not oriented parallel to gravity force and are much slower (around 1kHz) than galvanometric mirrors, which results in lower flexibility and slower acquisition frame rates (Dean et al. 2022).

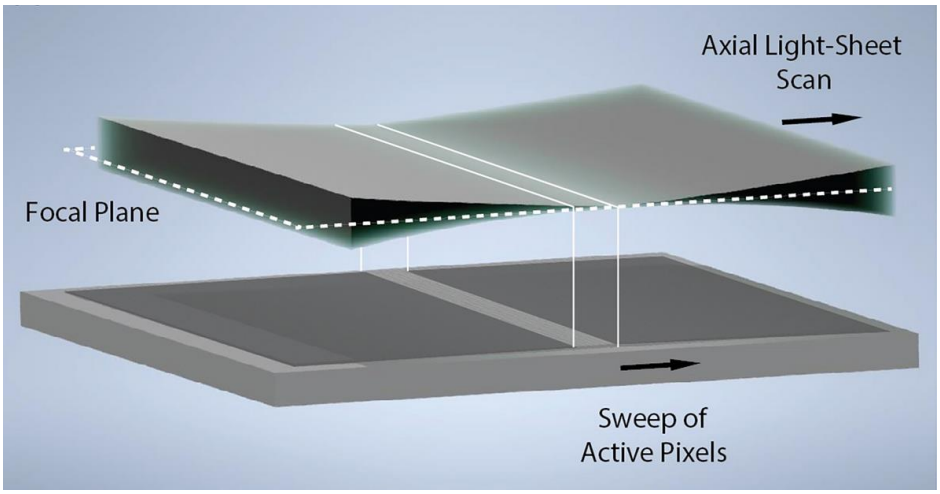


*Figure 10. ETL axially swept light-sheet in a confocal slit setup. (Dean et al. 2022)*

A very practical way to turn around the drawbacks of using an ETL, is to convert the lateral scanning performed by a galvanometric mirror into an axial scanning, thus creating another kind of digitally scanned LSFM (Chakraborty et al. 2020). Such a setup, shown in Figure 11, includes two perpendicular arms, each equipped with a 4F telescope and an objective lens. The remote-focusing arm includes a galvanometric scanning mirror (GSM) and an air objective lens (Figure 11, OBJ1), while the illumination arm is equipped with a pupil-matched water immersion objective (Figure 11, OBJ2). Both arms are aligned so that the GSM is conjugated with the back focal plane of both objectives. The laser foci at various axial positions generated by OBJ2 are monitored by two imaging systems: one for direct transmission measurements and the other for detecting fluorescence in a perpendicular direction. Each imaging system comprises

water immersion objectives, tube lenses, a camera, and suitable optical filters.

A collimated laser beam is reflected by a polarizing beam splitter into the remote-focusing arm, where the GSM scans the beam, inducing lateral movement of the laser focus produced by OBJ1. For discrete axial re-focusing, a step mirror is positioned in the focal plane of OBJ1 (Figure 11, b). When the laser hits a step exactly at the focal plane, the back-reflected beam becomes collimated, creating a laser spot at the nominal focal plane of OBJ2. Notably, as the GSM de-scans the returning beam, no lateral motion is transferred to the focus created by OBJ2, resulting in pure axially scanned motion. If the laser beam is directed to a point out of the nominal focal plane, the resulting focus shifts away from the focal plane (Figure 11, b). The beam in infinity space will then either converge or diverge, leading to axial refocusing of the beam by OBJ2. By accurately matching the pupils of the two objectives and demagnifying the spot of OBJ1 by a factor of 1.33 into OBJ2's focal plane, aberration-free remote focusing is achieved.

For continuous axial re-focusing, the step mirror is replaced with a slightly tilted planar mirror (Figure 11, c). The incoming laser focus is also tilted to be perpendicular to the mirror surface. This tilt is accomplished by slightly shifting OBJ1 relative to the incoming beam. When the laser focus is formed on the mirror surface, a collimated beam is created in infinity space, producing a laser spot at the nominal focal plane of OBJ2 (Figure 11, c). Scanning the beam laterally generates a focus away from the mirror plane, causing the beam in infinity space to converge or diverge, resulting in an axially shifted focus formed by OBJ2. Numerical and experimental results show that with small tilt angles, spherical aberrations are avoided. For this continuous z-scanning method, OBJ1 must have a larger angular aperture than OBJ2 to enable tilting of the laser focus without compromising OBJ2's numerical aperture. The range of axial scanning is approximately proportional to OBJ1's field of view multiplied by the tangent of the mirror's tilt angle, making the technique advantageous when using objectives and scanning systems with a large field of view. Conversely, the step mirror allows for arbitrarily large axial displacements, though larger steps are needed for greater defocus, which

imposes practical limits on the number of steps that can be utilized within a given field of view for the remote objective.

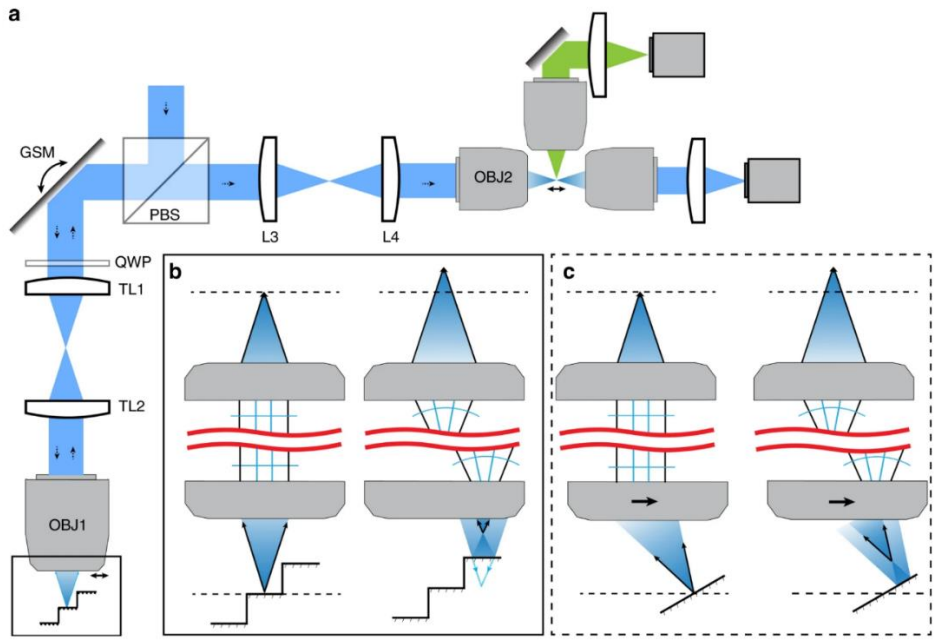


*Figure 11. (a) Axially scanned LSFM optical path scheme. (b) Discrete axial translation with a step mirror or (c) continuous refocusing with a tilted planar mirror. (Chakraborty et al. 2020)*

*Light-sheet theta microscopy (LSTM) and dual-illumination SPIM.*

As a very versatile technique, LSFM has recently developed into a large variety of custom, open-source and out-of-the-box solutions to fit new and unique research needs. Recent light-sheet fluorescence microscopy designs that enable laterally unconstrained imaging include dual-inverted selective-plane illumination microscopy (diSPIM, Figure 14) and light-sheet theta microscopy (LSTM). In LSTM (Figure 12), the collection objective is oriented vertically into a liquid reservoir, while a pair of longer working distance objectives, angled at 60° relative to the vertical

axis, generates the light sheet (Hu, Bolus, and Brown 2018; Migliori et al. 2018).

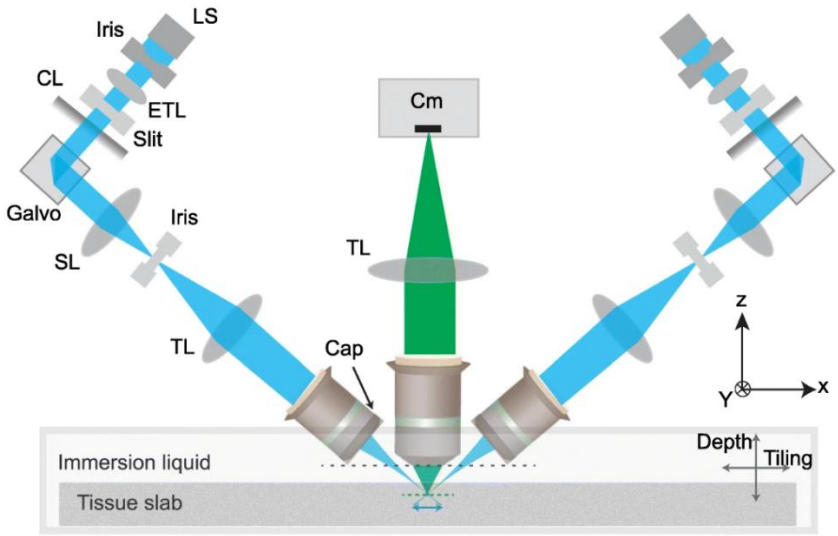


*Figure 12. LSTM optical paths in a confocal slit design. (Migliori et al. 2018)*

In diSPIM, the illumination and collection objectives are positioned at a 45° angle relative to the vertical axis and immersed in a liquid reservoir containing a cleared specimen (Sparks et al. 2020).Another convenient option for imaging large slabs of tissue is the inverted Dual-SPIM configuration, where the system features two symmetrical arms, each holding a multi-immersion objective with correction collars designed to match a range of refractive index values of various immersion media. The optical axes of the two objectives are perpendicular to each other, with their fields of view orthogonally aligned and overlapping at the center. Additionally, the objectives are tilted to 45 °C relative to the horizontal specimen chamber, allowing to fit large samples (Figure 14). A camera is placed at the end of each detection path for image acquisition. In this configuration, each objective alternatively excites the sample and collects the emitted signal, thus enabling a simultaneous two channels excitation and acquisition (Marcos-Vidal and Ripoll 2020). Moreover, it is possible to acquire the same channel from both sides and, after performing deconvolution and fusion processes of the two views, this results in an

increase in the axial resolution of the system and to potentially obtain isotropic resolution, the only drawback being an increase in the time needed for imaging and data processing (Kumar et al. 2014; Swoger et al. 2007; Wu et al. 2013).

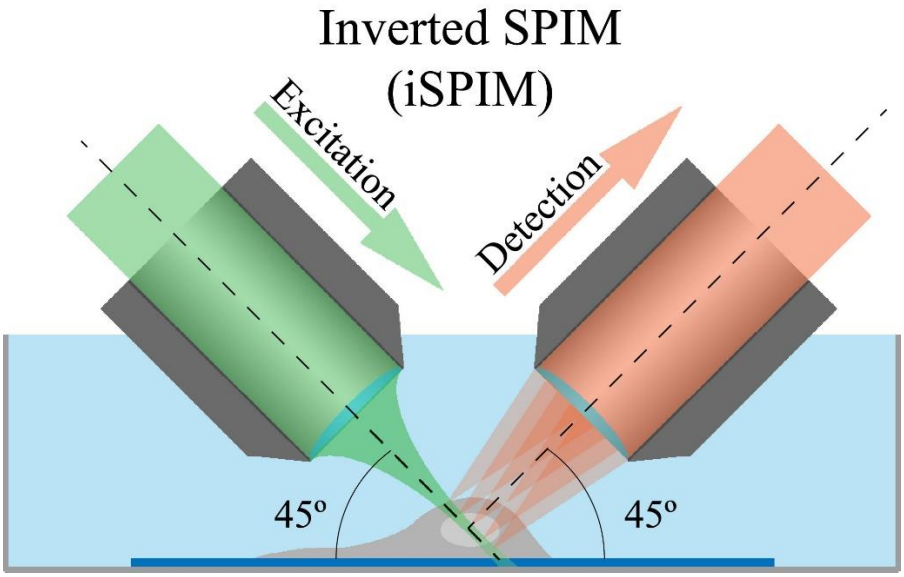


*Figure 13. Dual inverted-SPIM (diSPIM) configuration. Each objective acts both as illumination and detection objective. (Marcos-Vidal and Ripoll 2020)*

*Open-top LSFM.*

Although both diSPIM and LSTM allow for laterally unconstrained imaging, they have several limitations: i) cleared tissues often reach a density similar to the surrounding medium when fully immersed, causing them to float and drift; ii) specimens are usually placed in a large immersion media reservoir, leading to cross-contamination and reagent dilution; iii) immersion objectives may be incompatible with certain corrosive organic solvents used in tissue-clearing protocols; 4) imaging

specimens from above complicates the application of gravity or gentle pressure to flatten their top surfaces, if needed.

When imaging large, cleared samples is required, an open-top layout is often preferred as it allows easy access to the sample holder and manipulation of large specimens. To enhance the usability and throughput of LSFM, open-top light-sheet (OTLS) microscopes have been developed. In OTLS, the illumination and collection objectives are also angled at 45° relative to the vertical axis but are positioned below the cleared specimen, rather than above it (Figure 13). This open-top configuration resembles a flatbed scanner, allowing multiple specimens to be placed on a transparent holder without full immersion. Gravity and surface tension help in stabilizing the specimens, and gentle pressure can also be applied from above to flatten their surface if required. This setup addresses many of the problems associated with diSPIM and LSTM, while also providing flexibility for adding accessory devices on the specimen stage or above the specimens, like micromanipulators or injection systems. However, a drawback of the OTLS configuration, similarly to diSPIM, is that the oblique orientation of the objectives reduces their effective working distance, thereby limiting the imaging depth, unlike in LSTM, where the full working distance of the collection objective is utilized (Figure 13).

Despite its versatility, the OTLS architecture introduces some optical challenges. The off-axis illumination beams and detection arms that must be carefully index-matched at the media interfaces to avoid aberrations. To assure aberration-free imaging, a water prism or solid-immersion lens (SIL) has been proposed as an interface for the beams transitioning from air to a higher-index medium. The water prism provides a normal interface to reduce off-axis aberrations, while the SIL offers a wavefront-matched interface to prevent both off-axis and spherical aberrations. However, these solutions limit specimen scanning to 2D, as specimens cannot be lowered without colliding with the water prism or SIL. Additionally, these methods are less adaptable to varying refractive indices, as the specimen

must match the refractive index of the water prism or SIL material precisely (A. K. Glaser et al. 2019; 2022).

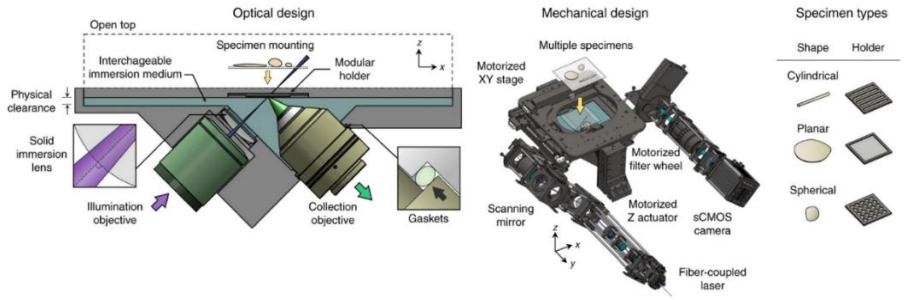


*Figure 14. Open-top LSFM design with a solid immersion lens (SIL). (A. K. Glaser et al. 2019)*

*Open-source LSFM projects.*

In recent years, as an alternative to systems offered by companies or custom-made solutions, which require specialized expertise, open-source LSFM projects started to spread among researchers due to their versatility, relatively low cost and little expertise required to set them up. One of these open-source setups, which was the first one to be released in 2007, is the OpenSPIM project (Greger, Swoger, and Stelzer 2007) that can be found at https://openspim.org/ . The website of the projects contains the parts list and a detailed description of the assembling process, making it possible for any personnel with minimal expertise to build their own setup. In addition, the operating software (µOpenSPIM) was developed as a MicroManager plugin (https://micro-manager.org/) and is characterized by a user-friendly interface. The microscope has a very compact design and can be fit in a case, allowing for easy transportation (Figure 15).

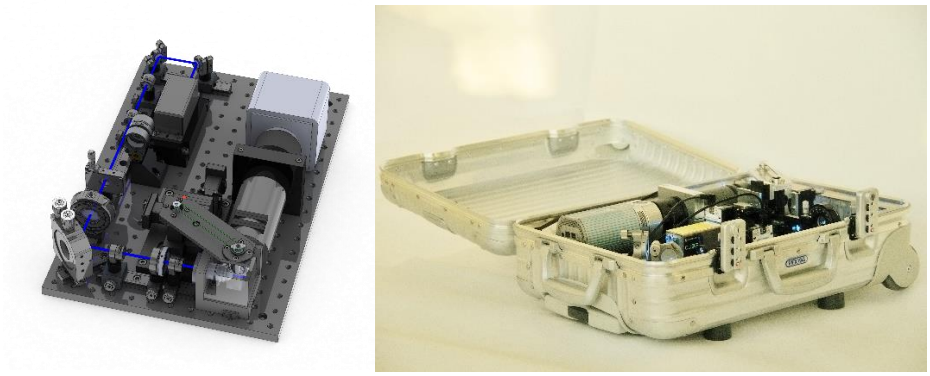

*Figure 15. OpenSPIM LSFM. Left: optical setup. Right: OpenSPIM in a handcase.*

Expansions and upgrades to the basic setup are also available, like the addition of bright-field illumination, a chamber for imaging mice and rat brains, extended FOV and the implementation of a second illumination arm to limit shadowing artifacts through a more homogeneous illumination. Additional open-source projects are currently available, like the MesoSPIM, for large FOV, isotropic resolution imaging (https://mesospim.org/ , Chhetri et al. 2015) including its recently released benchtop version (Vladimirov et al. 2024), and the IsoView LSFM (Chhetri et al. 2015).

The availability of open-source solutions significantly contributed to the spread of LSFM in research, allowing even smaller groups with limited budget and expertise to access this leading microscopy technique.

## 2.2 Application of LSFM in neuroscience

Light-sheet microscopy has increasingly spread in recent years among research groups as a very versatile and valuable tool for imaging large samples in high resolution, allowing scientists to gain deeper knowledge of complex biological processes and structures. Its ability to capture complex dynamic processes in real-time and in 3D has been critical in enhancing our understanding of various biological systems. Additionally,

LSFM has been adopted for clinical diagnostics and cancer research. The applications of LSFM in modern research span numerous disciplines, from developmental biology and neuroanatomy to pathology and immunology.

LSFM has been spreading critically in the past decades in neuroscience as a fundamental tool for investigating the structure and functions of the brain and neurons at cellular level.

The nervous system, made up of a complex network of neurons and supporting cells, is challenging to image, especially when trying to see large areas in 3D. Traditional methods like electron microscopy offer high detail but are limited to small regions of the brain. LSFM allows imaging of entire brain regions or even whole brains in 3D, providing a powerful tool for studying neural circuits and brain structure.

One main use of LSFM in neuroscience is mapping neural circuits. Neurons form complex networks that underlie all brain functions, from sensing to movement and thinking. Understanding how these circuits are built and how they communicate is key to unraveling brain function. LSFM lets researchers image whole neural circuits in model organisms like zebrafish and mice with fine detail. This has greatly advanced our understanding of how different brain regions connect and how these connections support behavior (Hillman et al. 2019).

For example, LSFM has been used to study the visual system of zebrafish, a common model for neuroscience research. By imaging the entire brain of zebrafish larvae, scientists have mapped the neural circuits involved in processing visual information and linked specific brain areas to behaviors. This large-scale imaging is crucial for understanding how the brain integrates and processes sensory information, which would be difficult with traditional microscopy methods (Vladimirov et al. 2014; Kugler et al. 2020; de Vito et al. 2022).

LSFM has also been used to investigate changes in the brain during neurodegenerative diseases. In Alzheimer's disease, for instance, the buildup of harmful proteins like amyloid plaques and tau tangles leads to the breakdown of neural circuits and cognitive decline. Using LSFM, researchers have visualized the spread of these proteins throughout the brain in 3D, offering new insights into how they contribute to disease

progression. This ability is invaluable for finding therapeutic targets and developing treatments to stop or slow down neurodegeneration (Kirschenbaum et al. 2023; Linsley, Reisine, and Finkbeiner 2024).

### 2.2.1 Imaging brain tissue with light-sheet microscopy

Recent developments in brain imaging have had a huge impact on neuroscience, giving us new insights into how the brain is built and how it works. Traditional imaging methods like magnetic resonance imaging (MRI) and positron emission tomography (PET) have been essential for studying large-scale structures and brain activity. However, these techniques can't see details at the cellular level, so they can't fully map complex neural circuits or detect structural issues related to developmental or degenerative brain diseases. Light-sheet microscopy offers a powerful solution by providing high-resolution, three-dimensional (3D) imaging of large brain tissues with minimal damage, fast data collection, and a wide field of view.

Tissue clearing methods like CLARITY, CUBIC, and iDISCO (Tian, Yang, and Li 2021; Vieites-Prado and Renier 2021) are used alongside light-sheet microscopy to make large human brain volumes transparent, enabling the visualization of deep brain structures without cutting the tissue. This approach is crucial for mapping how different parts of the brain connect, understanding developmental and degenerative brain diseases, and conducting large-scale projects like the Human Brain Project (HBP).

The speed of light-sheet microscopy is vital for studying large, optically cleared human brain samples, greatly reducing the time needed to collect images (Zhang et al. 2021; Mazzamuto et al. 2023). This fast imaging is essential for capturing detailed 3D reconstructions of complex neural networks in large brain volumes or organoids.

With its its high spatial resolution, light-sheet microscopy is ideal to visualize tiny structures like axons, dendrites, and synapses within large brain volumes (Fiolka 2021; Colombo, Norton, and Cocucci 2021; Remacha et al. 2020). By using specific fluorescent markers, it can

precisely locate proteins, neurons, and glial cells, contributing to our understanding of the brain's structural organization (Hillman et al. 2019).

Studying the human connectome, the complex network of neural connections in the brain, is crucial for understanding cognition, behavior, and neurological disorders. While diffusion MRI is commonly used to map large-scale brain networks, it doesn't have enough resolution to see the fine details of synaptic connections. Light-sheet microscopy offers a way to visualize the brain's microcircuits in unprecedented detail, bridging the gap between large-scale and small-scale mapping of brain connections (Costantini et al. 2024).

One of the most promising uses of light-sheet microscopy is in studying neurodegenerative diseases like Alzheimer's, Parkinson's, and amyotrophic lateral sclerosis (ALS). These diseases involve the gradual loss of neurons and the buildup of harmful aggregates, such as amyloid-plaques and tau tangles in Alzheimer's disease. Light-sheet microscopy has been used to image these pathological structures in large sections of human brain tissue, allowing researchers to study their distribution and interaction with surrounding cells (Bèchet et al. 2020; Liebmann et al. 2016). Imaging entire 3D brain regions affected by the disease, revealed patterns of amyloid accumulation and its relationship with neuron loss and glial cell activation.

Another significant contribution of light-sheet microscopy is in studying brain development and neurodevelopmental disorders. Human brain organoids have become valuable models for studying human brain development in the lab. Light-sheet microscopy allows researchers to image these organoids at high resolution, observing how neural progenitor cells differentiate, cortical layers form, and synapses develop (Shnaider and Pristyazhnyuk 2021; Jain et al. 2023). It has been fundamental in investigating disorders like autism spectrum disorder (ASD) and schizophrenia. By imaging brain organoids derived from patients with these conditions, researchers have identified structural abnormalities in neural circuit formation and synaptic organization that may explain the

cognitive and behavioral issues observed (Soumier, Lio, and Demily 2024).

Despite these advances, several challenges remain. One major limitation of light-sheet microscopy is its limited penetration depth, which can make it difficult to image deep brain structures in large human samples. Researchers are exploring improvements like multi-photon excitation and adaptive optics to overcome this limitation and extend the imaging capabilities of light-sheet microscopy (Vito et al. 2022; Truong et al. 2011). Another challenge is the massive amount of data generated, especially in whole-brain imaging studies. Processing, storing, and analyzing these large datasets require advanced computational tools and machine learning algorithms. Efforts are being made to develop automated image analysis pipelines to handle the complexity of the data and extract meaningful biological information (Gibbs et al. 2021; Amat et al. 2015).

## 2.3 Optical clearing of brain samples

Biological tissues, like the brain, are opaque due to the presence of different molecules like proteins, lipids and pigments, which limit the depth that conventional optical imaging methods like confocal and two-photon microscopy can reach because of light absorption and scattering. To overcome this, researchers have developed tissue clearing techniques that make tissues transparent, allowing deep imaging of cellular structures without needing to physically cut the tissue.

Tissue clearing has evolved into several categories, each differing in chemical composition, methods, and specific applications to certain tissues. The main categories are based on organic solvents, aqueous or hyper-hydrating techniques, and hydrogel-embedding strategies (Ueda, Ertürk, et al. 2020).

The development of tissue clearing methods is driven by the need to reduce light scattering caused by different refractive indices within biological tissues. These methods aim to make tissues transparent while preserving their molecular and structural integrity, especially for antibody

binding sites (epitopes) needed for fluorescent labeling and imaging. A critical aspect is obtaining an optimal refractive index (RI) matching: a homogenization of the tissue's refractive index with that of the clearing medium. Proper RI matching minimizes light bending and scattering allowing it to pass through the tissue, leading to enhanced transparency.

One of the main challenges in adapting optical clearing techniques to human brain samples is the increased size, density, and myelination compared to rodent brains (‘Author Spotlight: Advancing 3D Cytoarchitecture Analysis - Rapid Volumetric Reconstruction of the Human Brain’, n.d.). Future developments will need to focus on improving the speed and depth of clearing, as well as enhancing compatibility with the unique properties of human brain tissue. Moreover, integrating tissue clearing with advanced imaging methods like light-sheet microscopy and single-cell RNA sequencing will further expand research possibilities, enabling more comprehensive analyses of brain function and pathology (Jiang, Gong, and Yuan 2023).

### 2.3.1 Refractive index matching in tissue optical clearing

When biological tissues and the imaging medium have different refractive indices, light scattering and optical aberrations occur, which greatly reduce imaging resolution and depth. This problem is especially critical in light-sheet microscopy because it requires light to travel uniformly through samples to achieve high-resolution, distortion-free 3D images of cleared tissues.

To understand why matching refractive indices is important in tissue clearing, we need to look at how light interacts with biological tissues. These tissues are not uniform; they consist of components like cell membranes, extracellular matrix, and organelles, each with their own refractive index. As light moves through tissue, it scatters when it hits these structures. The amount of scattering depends on the size, shape, and refractive index of each biological component. Generally, biological

tissues have refractive indices between 1.33 and 1.50, while common clearing media range from 1.44 to 1.56 (Richardson and Lichtman 2015).

A large difference in refractive index between tissue components and the surrounding medium causes light to bend as a consequence of refraction. This bending reduces how deep light can penetrate and leads to image distortions and lower spatial resolution. For example, areas rich in lipids within tissues have a higher refractive index than water-based solutions, causing more light scattering and poor image quality (Tainaka et al., 2014). Matching the refractive index helps minimize these issues by making the tissue's optical properties more uniform.

Effective tissue clearing methods aim to equalize the refractive index across the sample by removing or altering components that cause mismatches. Clearing agents like organic solvents, water-based solutions, and hyper-hydrating methods replace or modify the tissue's internal parts to match the refractive index of the surrounding medium. This process reduces light scattering and improves optical transparency (Ke et al., 2013).

### 2.3.2 Organic solvent-based clearing methods

Organic solvent-based clearing methods are among the most used techniques. They typically involve dehydrating the tissue and then immersing it in an organic solvent with a high refractive index that matches the tissue components, making the tissue transparent. One pioneering method is 3DISCO, widely used for clearing various tissues, including the brain. This technique uses a series of dehydration steps in organic solvents like tetrahydrofuran (THF), followed by clearing in a refractive index-matching solvent such as dibenzyl ether (DBE) (Ertürk et al. 2012).

The iDISCO protocol is an improvement over 3DISCO, incorporating immunolabeling steps to visualize specific molecular markers within the cleared tissue (Renier et al., 2014). iDISCO has been extensively used in neuroanatomical studies and disease models, including Alzheimer's disease. For example, it has been applied to study amyloid plaques and tau

tangles in AD mouse models, offering new insights into disease progression and plaque distribution (Liebmann et al. 2016).

Another solvent-based approach is the BABB (Benzyl Alcohol/Benzyl Benzoate) clearing method. It uses a mixture of benzyl alcohol and benzyl benzoate to dehydrate the tissue and enhance transparency, similar to 3DISCO. BABB is particularly effective for clearing embryos and small organs but is less commonly used for large adult brain samples due to tissue shrinkage and distortion (Azaripour et al. 2018).

Despite their effectiveness, organic solvent-based clearing methods have limitations. They often cause tissue shrinkage and deformation because of the harsh solvents used, which can affect the accuracy of structural and quantitative analyses. Additionally, preserving fluorescent proteins is challenging with these methods, requiring alternative labeling strategies (Baatsen et al. 2021; Li et al. 2018).

### 2.3.3 Aqueous-based clearing methods

Aqueous-based clearing techniques have emerged as gentler alternatives to organic solvent methods. These techniques use water-soluble chemicals to reduce refractive index mismatches within tissues, making them transparent without dehydration or the use of organic solvents. One popular method is Scale, developed by Hama et al. (Hama et al. 2015). It uses urea-based solutions to make the tissue transparent by breaking down lipid bilayers while preserving protein fluorescence.

The CUBIC method, developed by Susaki et al. 2014, uses a combination of aminoalcohols and detergents to remove lipids while maintaining protein fluorescence. This method is advantageous for large-scale 3D imaging, especially for tissues that require fluorescent markers to be preserved. CUBIC has been widely applied to mouse brain clearing and is compatible with light-sheet microscopy (Tainaka et al. 2014). Its

effectiveness and scalability make it a valuable method for clearing large tissues.

Another aqueous clearing process is SeeDB, developed by Ke et al. 2013. It's a fructose-based method designed to preserve tissue structure and protein fluorescence. SeeDB is relatively gentle and works well with multiple rounds of immunolabeling. However, its high viscosity can make the clearing process slow and uneven, especially in larger tissues, and it may not achieve the same level of transparency as methods like CUBIC or 3DISCO (Ke et al., 2013).

### 2.3.4 Hydrogel-based clearing methods

*CLARITY clearing method.*

Hydrogel-based clearing methods offer a unique approach by combining tissue clearing with structural preservation. A significant breakthrough in this area is CLARITY (Clear Lipid-exchanged Acrylamide-hybridized Rigid Imaging/Immunostaining/In situ-hybridization-compatible Tissue hYdrogel). This method embeds the tissue in a hydrogel matrix, which crosslinks proteins and other biomolecules, while lipids are removed using a detergent solution (Chung et al. 2013; Costantini et al. 2015). The hydrogel provides structural support, preserving the tissue architecture and allowing for molecular labeling even after clearing.

CLARITY is particularly suitable for immunolabeling, permitting multiple rounds of antibody staining without damaging the tissue. However, the method is time-consuming and requires specialized equipment like electrophoretic clearing systems (H. Lee et al. 2014). Another challenge is the incomplete removal of lipids in large tissues, which may limit transparency and reduce imaging depth.

This approach has inspired several derivative protocols, such as the Passive Clarity Technique (PACT) and Fast Free-of-Acrylamide Clearing

Tissue (FACT), which have shown better efficiency and tissue preservation compared to CLARITY (Neckel et al. 2016; Xu et al. 2017).

*SWITCH clearing method.*

The SWITCH (System-Wide Control of Interaction Time and Kinetics of Chemicals) protocol was developed to offer a more controllable method for both clearing and labeling tissues. It relies on precise control of chemical interactions by adjusting pH, temperature, and time during the clearing process. This method is highly customizable and suitable for various tissues, including the brain (Murray et al. 2015). By changing reaction conditions, SWITCH ensures uniform distribution of clearing agents and molecular probes, allowing large and complex tissues to be cleared evenly without the need for electrophoresis.

One main advantage of SWITCH is its ability to perform clearing and molecular labeling at the same time. This reduces the overall preparation time and allows for more consistent labeling across the tissue. The protocol has been successfully applied to human and mouse brains to map whole-brain neural circuits at high resolution (Murray et al., 2015). However, its complexity and the need for precise control can be challenging for less experienced laboratories.

*SHORT clearing method.*

The SHORT (Systematic Hydrogel Optimization for Rapid Tissue-Clearing) protocol is a newer innovation designed especially for human brain tissue that combines the SWITCH tissue transformation method with the TDE aqueous clearing. SHORT lowers the tissue autofluorescence and enhances the accessibility of epitopes in combination with clearing and staining processes while preserving the biological structure. It combines hydrogel embedding with bleaching and antigen retrieval steps enabling successful clearing and staining of human brain tissues. SHORT improves upon CLARITY's and SWITCH’s limitations leading to more uniform embedding and better structural preservation (Pesce et al. 2022). Additionally, SHORT retains the benefits of hydrogel-embedding methods, including compatibility with immunostaining and LSFM.

However, like other hydrogel-based techniques, it requires specialized equipment and reagents, which may limit its accessibility.

## 2.4 LSFM high-throughput and data management

Despite its significant advantages, LSFM presents challenges, particularly in managing the massive amounts of data it generates. The high temporal and spatial resolution, combined with multi-channel capabilities and the large pixel density of modern camera sensors, can produce terabytes to petabytes of data in a single experiment (Li et al., 2017). Effective management, storage, and analysis of these large image datasets are crucial for a smooth research workflow.

LSFM captures data in 3D and often in multiple channels for different fluorescent markers, and even 4D data when performing live imaging. Each voxel represents a 3D pixel of information, and modern LSFM systems can capture millions to billions of these voxels at each time point (Wu et al., 2013). This complexity increases data size exponentially compared to traditional 2D imaging methods. As a result, handling these large datasets can become unmanageable using conventional systems (Zhou et al., 2018).

Another challenge is the need for standardization in LSFM data formats and analysis pipelines. The variety of imaging systems and data formats used in LSFM makes it hard to develop universal tools for data management and analysis (Bock et al., 2020). Efforts are underway to standardize data formats, like the Open Microscopy Environment (OME) format, but more work is needed to ensure that LSFM data can be easily

shared and analyzed across different platforms and institutions, improving repeatability.

### 2.4.1 Large data storage

Given the size of LSFM data, efficient storage solutions are essential. Standard hard drives or consumer-level storage options can't handle multi-terabyte datasets effectively. To address this, researchers have developed high-performance storage systems. Parallel file systems like Lustre and GPFS (General Parallel File System) are often used for large-scale image data storage. These systems allow multiple nodes to read and write data simultaneously, greatly improving data throughput. For example, Lustre is commonly used in high-performance computing environments for storing large scientific datasets due to its scalability and fault tolerance (Behnel et al., 2013).

Hierarchical Storage Management (HSM) systems have also been implemented to automatically move data between high-speed, high-cost storage (like SSDs) and high-capacity, lower-cost storage (such as magnetic tapes or cloud storage) based on how often the data is accessed. This approach keeps frequently used data on faster storage while archiving less frequently accessed data on slower, more cost-effective hardware (Rueden et al., 2017).

Another solution for managing large data is data compression. Lossless compression techniques, like using the HDF5 file format (Hierarchical Data Format), are increasingly employed in LSFM to reduce storage requirements while maintaining data quality. HDF5 supports storing multidimensional datasets and is widely used in scientific fields because it efficiently handles large amounts of data. This format is increasingly supported by specific data processing software, enhancing computational speed and throughput in image analysis (Mangalam et al., 2021).

Since raw data, processed results, and experimental metadata need to be preserved and accessible for future studies and reproducibility, research

facilities often set up custom servers and workstations dedicated to LSFM data storage and analysis (Breda et al., 2018).

### 2.4.2 Processing and analysis of large datasets

LSFM datasets require substantial computational power for processing, including 3D/4D data reconstruction (reslicing, stitching), segmentation, counting, tracking, and visualization. Without proper data management workflows, computational bottlenecks negatively impact researchers' ability to analyze their data efficiently (Peng et al., 2021). Real-time analysis remains a significant challenge when working with large LSFM datasets, requiring the installation of dedicated servers which can handle large tasks (Roy et al., 2019).

Processing LSFM datasets requires high-performance computational resources. One of the most promising solutions is the use of Graphics Processing Units (GPUs) for image processing tasks. GPUs represent the faster solution for parallel processing, making them well-suited for handling the intensive tasks involved in LSFM data analysis (Wagner et al., 2020). Libraries like CUDA and OpenCL provide researchers with the tools to develop GPU-accelerated workflows, which can significantly reduce the time required to process large datasets. By leveraging the power of GPUs, researchers can perform complex analyses in a fraction of the time it would take using central processing units (CPUs) of their workstations.

Another approach for processing large LSFM datasets is the use of distributed computing frameworks, such as Apache Hadoop and Apache Spark, which allow researchers to process LSFM data across multiple computing nodes, providing the scalability needed to handle multi-terabyte datasets. These systems break down large datasets into smaller chunks that can be processed in parallel, significantly reducing processing time (Bigas et al., 2016). Distributed computing is particularly useful for

tasks that require the analysis of large numbers of individual images or for high-throughput experiments.

In addition to hardware-based solutions, machine learning has emerged as a powerful tool for managing LSFM data. Machine learning algorithms, particularly deep learning models such as convolutional neural networks (CNNs), have been successfully applied to tasks like image segmentation, feature extraction, and pattern recognition in biological imaging (Caicedo et al., 2019, Checcucci et al. 2024). CNNs, for example, can be trained to automatically identify and segment cells, tissues, or other structures within LSFM datasets, saving researchers significant time and effort. Training these models on large datasets can be computationally expensive but, once trained, they provide a highly efficient way to analyze new data.

Cloud computing is another area where significant progress has been made in managing LSFM data. Cloud platforms such as Amazon Web Services (AWS), Google Cloud, and Microsoft Azure offer scalable storage and computational resources that can be accessed remotely. These platforms provide nearly unlimited storage capacity, allowing researchers to store their LSFM data without the need for expensive local infrastructure. Cloud services also facilitate collaboration by making it easier to share data with colleagues and collaborators around the world (Schindelin et al., 2015). Moreover, many cloud platforms integrate with machine learning capabilities, allowing researchers to develop and perform analysis pipelines that can handle large LSFM data (Stringer et al., 2021). Indeed, international projects create specific platforms, such as EBRAINS or DANDI, for brain data to collect in the same space data related to this subject facilitating the networking of the neuroscience community (https://www.ebrains.eu/ , https://dandiarchive.org/).

Cloud computing also supports interactive exploration and visualization of large datasets. Tools like Jupyter Notebooks or Google Neuroglancer, enable researchers to interactively visualize their data and eventually run analysis pipelines in real-time. These tools can be run in cloud environments, allowing researchers to take advantage of powerful computational resources without needing expensive local hardware (Sofroniew et al., 2022). This combination of cloud computing and

interactive data exploration is very useful for researchers who need to quickly visualize and analyze large LSFM datasets.

## 2.5 Aims of the project

### 2.5.1 Research requirements and proposed solutions

Studying the human brain, due to its large size and complexity, is a challenging task for researchers and dedicated tools are necessary for investigating its structure and functionality. The necessity to visualize neuronal circuits and fibers in centimeter-size brain volumes and, virtually, in the entire human brain, results in the exigence of specific instrumentation to achieve fast volume imaging at cellular or sub-cellular resolution. When high resolution imaging of large human brain samples is required, light-sheet fluorescence microscopy represents the optimal choice.

The “Large Volumetric Mapping with light-sheet microscopy” group, led by Prof. Francesco Saverio Pavone at LENS Department, University of Florence, aims to push forward our knowledge of human and mice brain structure and functionality as well as to a better understanding of neurodegenerative diseases through cutting-edge technologies and thanks to the cooperation between Italian and international partners. In recent years, our group took part in many relevant projects, such as the Human Brain Project, and developed new imaging solutions for high-resolution imaging of brain tissues, new tools for image analysis as well as developing the SHORT clearing protocol for human brain tissue. Among many other systems, a dual-inverted light-sheet microscope was custom-built by the group to image human brain slabs up to 4x4cm in size and 500-700 μm thickness (Figure 14). This system is capable of imaging samples in four colors at a volumetric speed of 0.17 $cm^3/h$ with an isotropic resolution of 3.64 μm after image post-processing, resulting in an imaging time of 5 to 6 hours per sample, depending on slabs size (Pesce

et al. 2022, Di Meo et al. 2024). The setup has been used to image slices derived from blocks of 4x4x2 $cm^3$ of human Broca's area, whole human hippocampus and brain stem in the context of numerous projects.

Considering the large number of slices obtained from sectioning whole human brain areas, imaging speed becomes crucial for limiting the time required for obtaining useful data, especially when respecting projects strict deadlines is fundamental. Additionally, increasing the capacity of placing bigger sized samples in the specimen holder, would reduce the number of slices to be cut for each sample and the handling, clearing and staining processes by the operators, speeding up the research and gaining time to work on additional projects, thus increasing the productivity of the group. A final goal would be the capacity of imaging sections of entire human brain hemispheres or transverse sections of whole brain.

This PhD project focused on the realization of a custom-made light-sheet microscope to fulfill these research requirements. The project was financed by Ente Cassa di Risparmio di Firenze within the Human Brain Optical Mapping project.

An inverted confocal slit design, including one excitation arm and one detection arm, was chosen as the ideal solution. Four excitation lasers are used to illuminate the samples with four digitally scanned light-sheets at the same time, each synchronized with the rolling shutter of one of the four cameras on the detection side, allowing to record images in four colors with a single light-sheet sweep. This peculiar characteristic, in addition to the large field-of-view of the detection objective, allows to speed up the imaging process of one order of magnitude compared to the inverted LSFM mentioned above.

### 2.5.2 Project overview

As increasing the imaging speed was the main goal of the project, the setup has been designed to achieve this requirement in all of its elements.

Firstly, increasing the objective field-of-view represents an effective way to reduce the imaging time, as a wider captured area per frame cuts down the number of frames required to image the sample. Secondly, a very convenient way for imaging in four colors simultaneously was adopted.

The setup has been placed on a 230x120 cm optical bench on self-levelling, vibration isolators. The optical bench is surrounded by a steel cage which allows protective curtains to be placed around the whole setup to isolate it from environmental light during the operation and to shield the users from potentially hazardous laser radiation. Two 120x90x6 cm breadboards (B90120A, Thorlabs) have been placed aligned with the opposite short edges of the optical bench and elevated by pillars in such a way that the longest side of the breadboards results aligned with the shortest side of the optical bench. This positioning results in a "free" space on the optical bench, between the two breadboards, of 30 cm. The left breadboard, with respect to the operator position, hosts the illumination part of the system, including the four laser diodes, the beam combining optics, an acousto-optical tunable filter (AOTF), a diffraction prism, a galvanometric mirror, a scan lens and the tube lens of the illumination objective. The right breadboard is dedicated to the detection objective tube lens, three dichroic beamsplitters and the four cameras with the respective bandpass filters. In between these elevated side breadboards, a large three-axis motorized stage was placed at the center of the optical bench and a 45x30x2.5 cm (PBG3045A, Thorlabs) breadboard was secured on top of the two breadboards vertically. The illumination and detection objectives, mounted on XY stages, have been placed on this vertical breadboard, wich are respectively fixed on a manual and a piezoelectric stage for fine focus adjustment. A large sample holder on top of the three-axis stage is free to move beneath the two elevated breadboards. Figure 16 shows a preliminary study of the setup design.

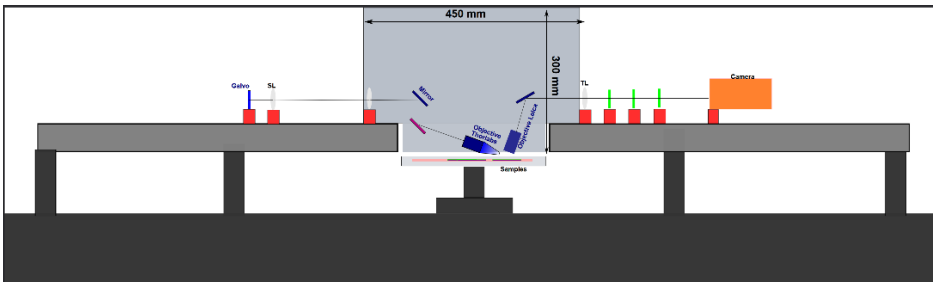


*Figure 16. Preliminary scheme of the setup design. The two lifted, lateral breadboards hold the vertical breadbord where the two objectives are located. A large specimen holder is mounted on top of the three-axis motorized stage.*

# 3. Materials and Methods

In this chapter, the realization of a custom light-sheet microscope for the fast imaging of human brain tissue in four colors will be discussed (quad-SPIM), as well as its software and data processing. The sample optical clearing and antibody labeling will also be discussed.

## 3.1 Excitation path design

### 3.1.1 Laser sources and beams combining

Four excitation laser wavelengths have been chosen to excite the fluorescent dyes in the sample. In particular, 488 nm, 561 nm, 594 nm and 647 nm wavelength laser lines were chosen to excite Alexa fluor 488, 561, 594 and 647 secondary antibodies (Thermo Fisher Scientific) used in conjunction with primary antibodies targeting specific neuron epitopes. The lasers used in the setup are four high performance, low noise, diode pumped solid state lasers (DPSS): the maximum power outputs consist in 100 mW for the 488 nm line (Cobolt 06-MLD 488nm), 100 mW for the 561 nm line (Cobolt 06-DPL 561 nm), 50 mW for the 594 nm line (Cobolt 594 nm 04 series) and 130 mW for the 647 nm line (Cobolt 06-MLD 647 nm). The beam diameter of the lasers is $0.7 \pm 0.05$ mm.

The four laser beams are combined into a single collimated beam before entering the AOTF (AOTFnC-400.650-TN, AA Opto-Electronic), used for line selection and beam blanking. The beams are combined by three 44x32 mm long-pass dichroic filters: a 552 nm cut-off frequency (F552-Di02-32x44-FX, Semrock), a 596 nm cut-off frequency (FF596-Di01-32x44-FX, Semrock) and a 649 nm cut-off frequency (FF649-Di01-32x44, Semrock). Two silver mirrors with VIS anti-reflection coating (PF10-03-P01, Thorlabs) have been placed in front of each laser at an angle of 45° in respect to the optical axis and at a distance of 15 cm from each other to ensure two degrees of freedom for precise alignment of the beams. After the second mirror, the beam is directed towards the respective dichroic filter. The three dichroic filters are positioned at an angle of 45° with respect to the optical axis and to the beam reflected by the second mirror of the respective laser line. Two iris diaphragms (iris 1 and 2, Figure 17) positioned before the AOTF entrance at a distance of 30 cm from each other are used as a reference for fine alignment of the four beams before their entrance in the AOTF.

A half-waveplate on a rotation mount was placed in front of each laser to finely adjust the beam polarization plane at the entrance of the AOTF to maximize the power output of the first-order diffracted beam exiting the AOTF, which is then directed towards the diffraction prism.
A schematic of the excitation path is shown in Figure 17.

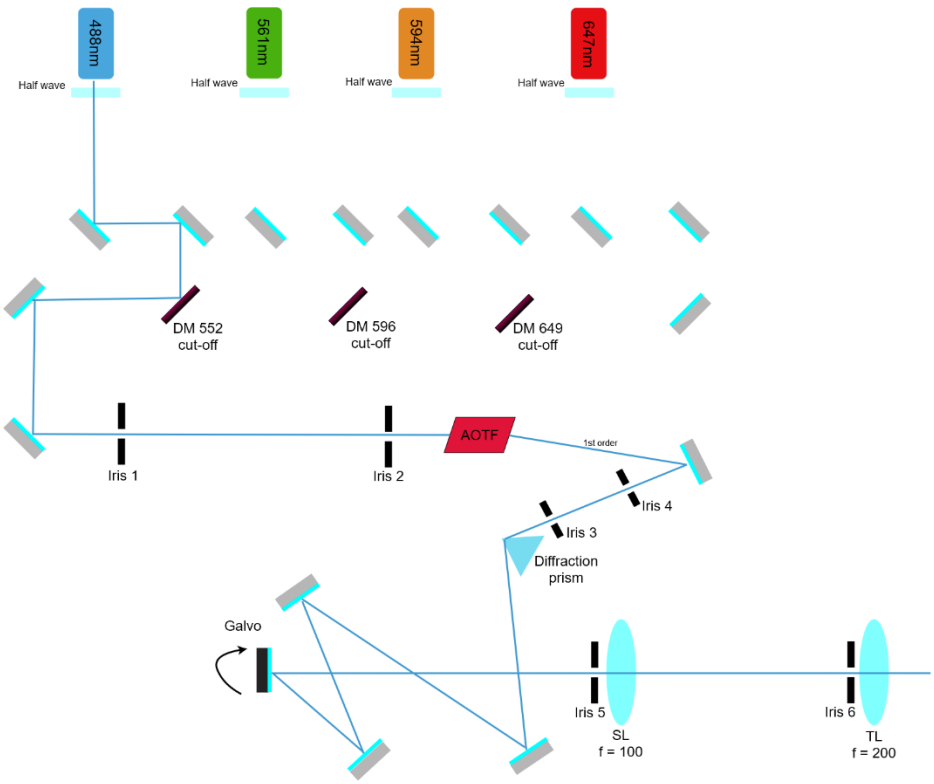


*Figure 17. Excitation path schematic. For simplicity, only the 488 nm beam is shown.*

### 3.1.2 Acousto-optical tunable filter (AOTF)

An acousto-optical tunable filter (AOTF) is a device used to control and filter light based on the interaction between light and sound waves in a crystal. AOTFs are widely used in optical systems because they allow for quick tuning of wavelengths without any moving parts, which makes them faster and more reliable than mechanical filters (Figure 18).

When an acoustic wave is passed through the crystal, it causes the crystal to vibrate and a pattern with alternating high and low-density areas is created as a consequence. These variations result in a change of the refractive index of the crystal, allowing certain wavelengths of light to be diffracted while others can pass through without changing according to Bragg's diffraction law. In practice, the crystal is now acting like a

selective diffraction grating. The desired wavelengths of light which are then diffracted, can be selected by adjusting the frequency of the acoustic wave applied to the crystal. In addition, the output power can be tuned by adjusting the amplitude of the acoustic wave passing through the crystal. As the only diffracted beam remaining at a constant angle at the crystal exit is the first order extraordinary diffracted beam, only this beam is allowed into the optical system. A practical way to filter out the three remaining beams, is to apply two polarizing filters, the first before the entrance of the crystal, and the second one at the exit.

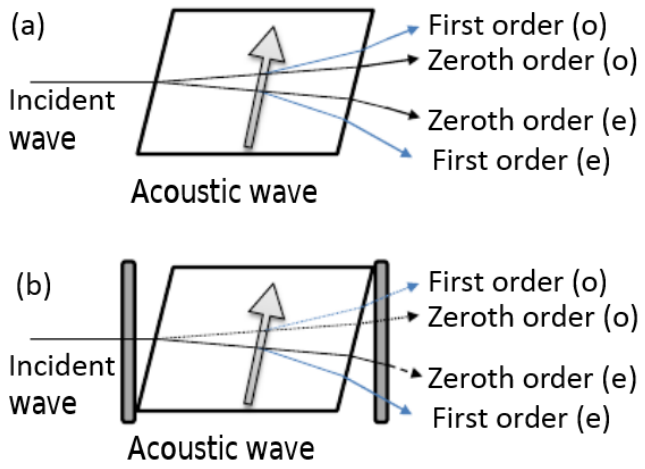


*Figure 18. Effect of Bragg diffraction in an AOTF. (a) When a RF wave is applied to the crystal -arrow- the incident beam is diffracted into four beams: an ordinary zeroth and first order beam and an extraordinary zeroth and first order beam. The only beam that remains at a constant angle at the exit of the crystal is the first order extraordinary diffracted beam. (b) When two linear polarizers are added at the entrance and at the exit of the crystal, the polarizer at the entrance removes the ordinary exit beams and the second polarizer removes the zeroth order extraordinary beam. As a result, only the first order extraordinary beam is maintained (Elash et al. 2015).*

In the setup, no polarizers were used to filter out the unnecessary diffracted beams, which are blocked by a beam stopper instead. The half waveplates in front of each laser can be rotated to finely adjust and maximize the power of the output first order extraordinary diffracted beam, which is then directed towards the diffraction prism by two mirrors.

### 3.1.3 Diffraction prism and beam separation

The key element of the illumination path is the diffraction prism (60° angles, GK7 glass, Thorlabs), located after the AOTF in the optical path and just before the galvanometric mirror. Its role is to diffract the four beams and separate them by an angle before entering the scan lens. As these beams are directed on the back focal plane of the illumination objective by the galvo, four spatially separated digitally scanned light sheets can be projected onto the sample at each galvo movement (Paragraph 2.1.5).
After the four combined beams pass through the prism, they undergo angular separation for the effect of refraction. Refraction happens when a wave travels through the interface between two media with different refractive index. A portion of the light will be reflected, while another portion will be refracted. The portion of reflected and refracted light can be approximately predicted by Fresnel equations.

In general, the deviation angle of the exit wave depends on the angle of the incident beam and on the ratio between the RI of the two media, as described by Snell's law:

$$\frac{sin\,\theta_1}{sin\,\theta_2} = \frac{n_2}{n_1} = \frac{v_1}{v_2} \qquad (3.1)$$

Where $\theta_1$ and $\theta_2$ are the beam incident angle and exit angle with respect to the normal to the interface surface passing through the point of incidence; $n_1$, $n_2$ correspond to the refractive index of the two media; $v_1$, $v_2$ is the velocity of the wave respectively in medium 1 and 2 (Figure 19).

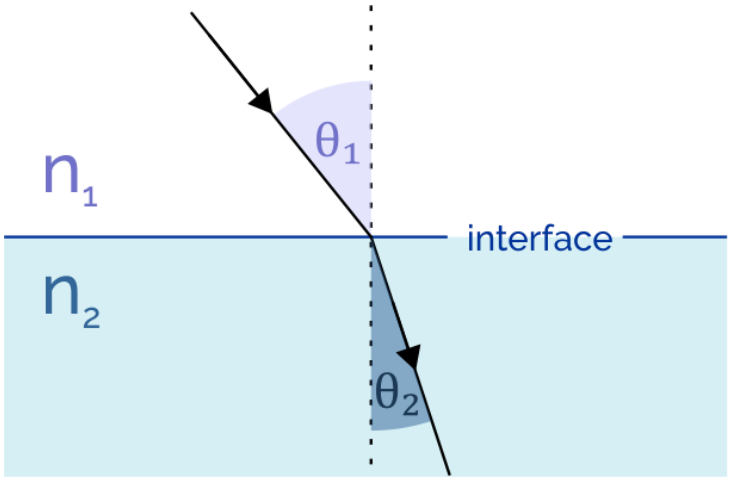


*Figure 19. Graphical representation of Snell's law.*

The refractive index of a medium is defined as:

$$n = \frac{c}{v} \qquad (3.2)$$

Where $c$ is the speed of light in vacuum and $v$ is the velocity in the medium.
Since $c$ is a constant, this implies that the velocity of a wave through a medium is inversely proportional to its RI, $n$:

$$v \propto \frac{1}{n} \qquad (3.3)$$

A crucial phenomenon occurring when light passes through a medium is dispersion, which causes its refractive index to change with the wavelength. The relationship between the wavelength and a medium RI can be empirically approximated by the Cauchy's transmission equation:

$$n(\lambda) = A + \frac{B}{\lambda^2} + \frac{C}{\lambda^2} + \cdots \qquad (3.4)$$

Where A, B, C,… , are material-dependent coefficients. From the equation, it follows that the RI of a medium is inversely proportional to the wavelength. As a consequence, lower wavelength light, like blue light, is refracted by a larger angle than red light.

In the setup, this property was used to split the beam obtained by combining the four laser beams into its fundamental components. By doing this, the four beams reach the galvanometric mirror in four slightly separated points on the y plane of the optical path.
Exciting the sample with four spatially separated light-sheets is fundamental to avoid channels cross-talk and to allow for four color imaging at high speed.

### 3.1.4 Scan system

A galvanometric mirror (Cambridge Instruments) is used to move the beams on the back focal plane of the illumination objective. The mirror is placed at 200 mm from a 50 mm diameter achromatic doublet (F=200 mm) with VIS AR coating (Thorlabs), used as scan lens, thus matching its focal length. Another F=200 mm achromatic doublet was used as tube lens and aligned on the optical axis at a 400 mm distance from the scan lens (Figure 17). The 1:1 ratio of the scan lens and tube lens ensures that no magnification or demagnification is applied to the 0.7 mm laser beams. Two diaphragm irises (iris 3 and 4, Figure 17) are placed respectively in front of the scan and tube lens for beam alignment.

The refracted beams coming from the diffraction prism are then projected onto the galvanometric mirror by a series of three mirrors, which are used to finely adjust the beam alignment on iris 3 and 4. The beam path length between the prism and the galvanometric mirror has been adjusted by varying the distance of these three mirrors to obtain the ideal spatial separation of the four beams on the galvanometric mirror.

The mirror is controlled by an analog signal generated by an input/output board from National Instruments (Paragraph 3.7). The signal is a triangular wave where the ascending portion, with smaller slope, generates the light-sheet by sweeping the beams onto the sample, while the descending ramp, with steeper slope, repositions the mirror to the starting position.

## 3.2 Objectives

The illumination and detection objectives have been placed on a 45x30x2.5 cm vertical breadboard, mounted on adjustable mounts with 6 mm travel range in the *xy* plane of the optical path (ST1XY-S, Thorlabs). The vertical breadboard (PBG3045A, Thorlabs) is secured to the lateral elevated breadboards by two angular brackets (VB01/M, Thorlabs). A super apochromat 2x/0.10 NA objective (TL2X-SAP, Thorlabs) with 56.3 mm working distance was chosen as illumination objective. A Leica HC PL Fluotar 5x/0.15 NA immersion DLS objective with a free working distance of 4.8 mm and a field number of 25 was chosen as detection objective. The latter was selected as it was the only 5x, large FOV, objective designed for glycerol immersion available on the market. A higher NA and higher working distance custom solution could be considered in the future for higher resolution and smaller space constraint. The illumination and detection objectives have been set respectively on a 25 mm travel range manual stage (XNR25P/M, Thorlabs) and a 26 mm travel range piezoelectric stage (Q-545.240, Pysik Instrumente). The stages are respectively used to adjust the light-sheet position and the focusing of the detection objective. The vertical breadboard hosting the objectives is lowered downwards between the two horizontal breadboards to allow the objectives to exceed toward the specimen holder by 6 cm. This guarantees the free movement of the objectives within the specimen holder.

Two pairs of 50 mm diameter silver mirrors (PF20-03-P01, Thorlabs) mounted on the vertical breadboard between the objectives and their respective tube lens are used to finely adjust the alignment of the beam entering the illumination objective and the fluorescence light coming out from the detection objective to the detection path.

As a consequence of the relatively low free working distance of the Leica detection objective, physical space constraints resulted in the need for a lower angle of incidence of the light-sheet with respect to the sample *xy* plane compared to standard dual inverted-SPIM configuration, where the objectives are tilted 45° (Paragraph 2.1.5). By calculating the physical constraints of the objectives and the light-sheet confocal parameter $b=2Z_R$ (equation 1.2, Paragraph 2.1.2), an angle of 20° resulted to be the ideal configuration (Figure 20).

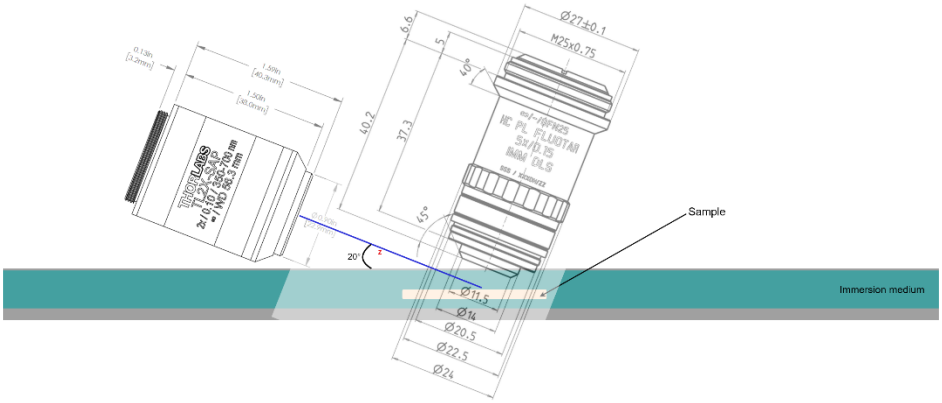


*Figure 20. Schematic of the illumination and detection objective layout. The optical axis of the illumination objective is tilted 20° in respect with the optical bench. The optical axes of the two objectives are normal to each other.*

As exploiting the large FOV of the illumination objective is of primary importance for maximizing the imaging speed, the confocal parameter *b* of the light-sheet beam needs to equal the FOV of the detection objective. The field of view of the detection objective on the camera sensor can be calculated by multiplying the camera pixel size by the number of pixels in the shortest dimension of the camera sensor. The cameras, four sCMOS Hamamatsu Orca Flash 4 v.3, provide a high-dynamic range, low-noise 16-bit sensor counting 2048x2048 6.5 µm pixels. The $FOV_{im}$ can then be calculated as:

$$FOV_{im} = \frac{6.5\ \mu m}{5} \cdot 2048 = 2662\ \mu m$$

Considering the 0.7 mm incident beam diameter entering the back focal aperture of the illumination objective, the confocal parameter can be calculated by substituting (1.1) into (1.2):

$$b = 2\frac{\pi\omega_0^2}{\lambda} = 2\frac{\lambda f^2}{\pi D^2} = 2\frac{0.561 \cdot 56300^2}{3.14 \cdot 700^2}\ \mu m = 2311\ \mu m$$

Where $\lambda$ = 0.561 μm.

The resulting 2311 μm confocal parameter is then compatible with the 2662 μm FOV of the illumination objective.

The 2x/0.10 illumination objective is not suited for immersion. A custom PVC cap with a 0.2mm thick quartz cover glass (RI = 1.46) glued at the end of the cap was designed to minimize the refractive index mismatch aberrations when the beam passes from air (n = 1) to 1.46 RI medium (quartz cover glass, 91% v/v glycerol/water of immersion medium, Figure 21). The effect is minimized as the incidence angle between the beam and the media interface is very close to 0°. According to Snell's law:

$$n_1 \sin\theta_1 = n_2 \sin\theta_2 \quad \text{with } n_1, n_2 \neq 0 \Rightarrow$$

$$\Rightarrow n_1 \sin 0° = n_2 \sin\theta_2 \Rightarrow$$

$$\Rightarrow n_2 \sin\theta_2 = 0 \Rightarrow$$

$$\Rightarrow \sin\theta_2 = 0 \Rightarrow$$

$$\Rightarrow \theta_2 = \arcsin 0 = 0°$$

When the angle of incidence at the interface is 0°, the refraction angle is 0° as well and no refraction occurs.

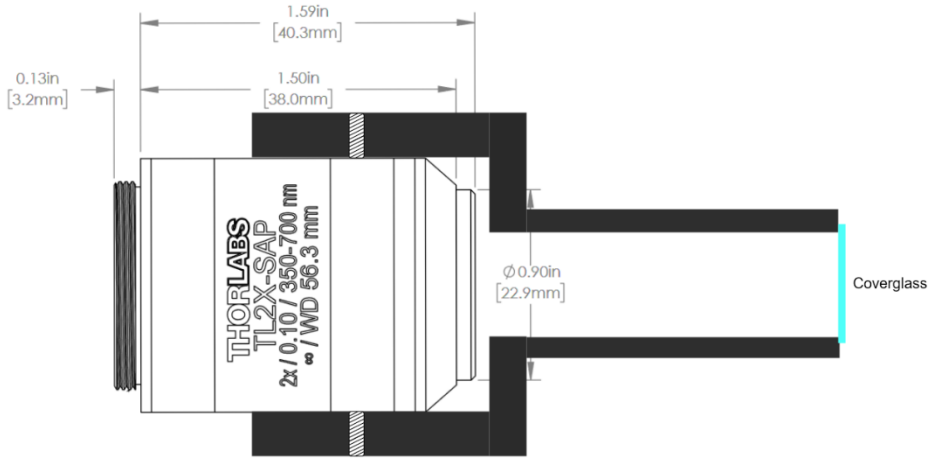


*Figure 21. Custom cap to isolate the illumination objective from the immersion medium and minimize the refraction at air/medium interface. Two plastic screws in the body are used to secure the cap to the objective.*

## 3.3 Detection path

The detection path comprises the detection objective tube lens, three dichroic long-pass mirrors which split the fluorescence signal into four channels, and four sCMOS Hamamatsu Orca Flash 4 v.3 cameras. All these components are mounted on the right elevated breadboard of the setup (Figure 23).
A 75 mm diameter, F=200 mm achromatic doublet (Edmund Optics) was used as the detection objective tube lens and it was aligned with the detection optical path.

Three 25.2x35.6x1 mm dichroic mirrors with cut-off frequencies of 520 nm, 581 nm and 604 nm (Alluxa) split the image into four channels. Figure 22 shows the transmission curves of the dichroic mirrors.

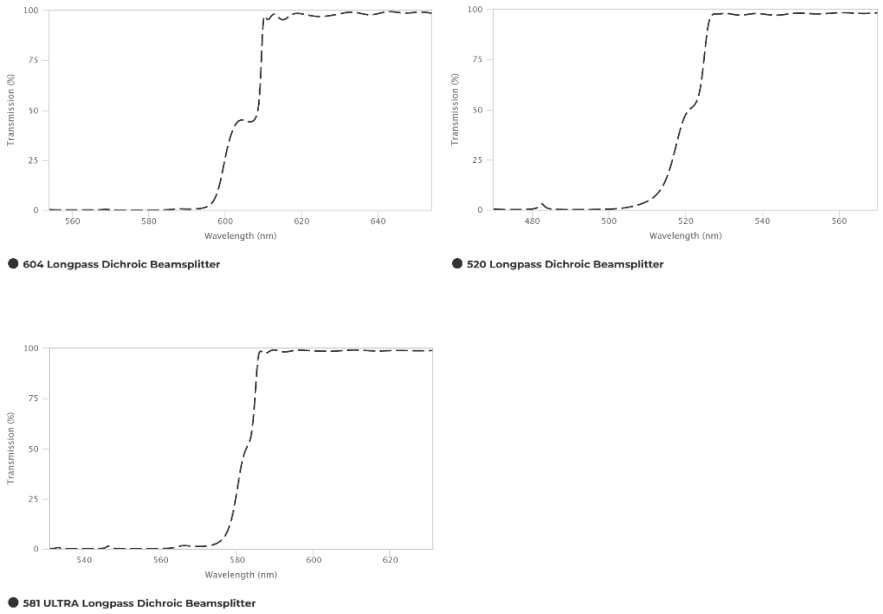


*Figure 22. Transmission curves of the dichroic mirrors used in the detection path.*

A 50 mm diameter band-pass filter was positioned in front of each camera to avoid cross-talking between the four channels. The specifics of the filters are as follows: (i) 520 nm CWL, 36 nm Bandwidth, (ii) OD 6 (67-044, Chroma), (iii) 578 nm CWL, 16 nm Bandwidth, (iv) OD 6 (87-766, Chroma), 623 nm CWL, 50 mm Dia, OD 6 (87-768, Chroma) and 692 nm CWL, 50 mm Dia, OD 6 (67-052, Chroma).

Each camera is mounted on a three-axis manual stage (PT3/M, Thorlabs) for precise positioning and focusing. The importance of fine adjustment of the cameras along the y axis for correct synchronization of their rolling shutter with the scanned light-sheets will be discussed in Paragraph 3.9). All cameras are positioned at the focal plane of the imaging tube lens, at a distance of 200 mm from it.

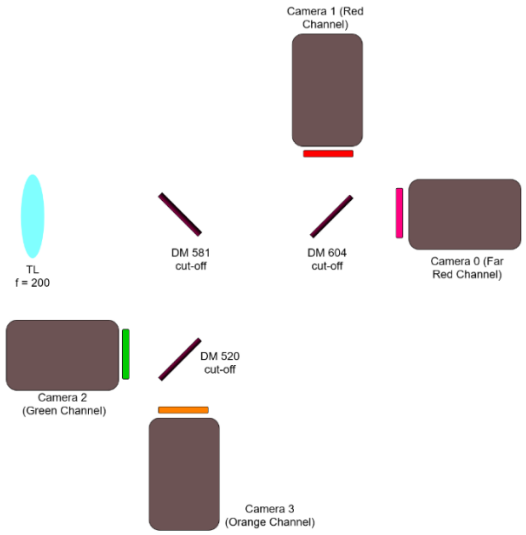


*Figure 23. Schematic of the detection path of the apparatus.*

## 3.4 Stage and specimen holder

The setup is intended to accommodate and image up to eight 60x60 $mm^2$ slides containing brain slices or for hosting whole brain sections. To this purpose, a large assembly of two precision linear stages (M-531.PD, Physik Instrumente) with a travel range of 300 mm were used for *x* and *y* movement of the specimen. A heavy-duty vertical precision stage with 26 mm travel range (L-310, Physik Instrumente) was assembled on top of the *xy* assembly for the vertical movement of the specimen chamber.

A custom specimen holder has been designed and machined from a bulk block of black PVC by the LENS Department mechanical workshop. The holder was entirely grooved to a depth of 20 mm, leaving a 20 mm edge to create a chamber for the immersion liquid. Eight 62x62 $mm^2$ slots were carved in the bottom of the chamber to allocate 60x60 $mm^2$ slides containing the samples. The resulting volume of immersion liquid that can be contained in the chamber is 2 liters.
Figure 24 displays a schematic of the final design of the setup.

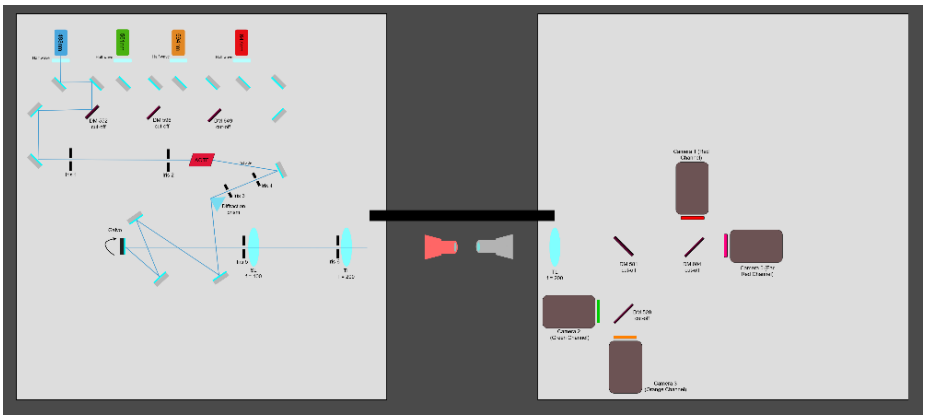

*Figure 24. Schematic of the setup.*

## 3.5 Computer and electronics

Two identical workstations have been installed to control the apparatus, one operating as master workstation with the control software installed, while the second works as a slave computer for the sole data acquisition from two of the four cameras. The two computers communicate via internal LAN connection. This configuration was required as one computer can only operate a maximum of two cameras. The operating system (OS) installed on both systems is Ubuntu v24.04.1.
The computers are server workstations based on two 8-core 4309Y 2.8GHz, 12M Cache Xenon processors (Intel) and 128Gb of 3200 MHz DDR4 RAM. A National Instruments 6738 PCIe DAQ card was installed on the master system to provide the required analog and digital outputs for controlling the system. Digital outputs are used to generate the AOTF blanking signal and the four camera triggers. One analog output is used to generate the triangular waveform for the galvanometric mirror.
The four laser drivers are connected to the workstation via USB ports, as well as the AOTF RF generator and the four stage driver units.
All the power supplies have been secured onto the optical bench and the bench was grounded for safety.

## 3.6 Control software

A custom control software, previously jointly developed by LENS and CNR-INO Departments and already in use on two light-sheet setups of LENS Department, was adapted to control the new apparatus. The software, named "SPIMLab" is freely available at: https://github.com/lens-biophotonics/SPIMlab in its original version intended for controlling the dual-inverted SPIM of the group (Mazzamuto et al. 2023).
The software was developed in C++ language and specific libraries (QtLab) were used to generate the GUI and to allow the communication with the lasers, stages, AOTF and the National Instruments DAQ card.
The software GUI was designed for user-friendly operation.

The main frame includes two cameras views, a top menu for selecting secondary controls, and, at the bottom the stage movement controls, galvo mirror and acquisition parameters controls. The stages controls allow to set the single step movement size and velocity. By clicking on the arrows, or by manually setting the position, the operator can move the stages. The galvo controls allow to set the amplitude, delay and offset of the galvo ramp. The *fraction* parameter sets the time duration of the ascending ramp as a percentage of the total time duration of the triangular wave.
The *acquisition* section of the main window allows to set the scan coordinates on the xy axes for an acquisition, as well as the file name and path, exposure time and binning of the camera sensor.
Figure 25 shows the main frame of SPIMLab.

The top menu opens secondary windows for lasers and AOTF control, *stages* secondary settings and general settings of signal I/O ports for digital/analog signals on the National Instruments DAQ card, including analog output port for the galvo ramp, camera triggers and *x* stage start trigger. The number of cameras (channels) to be acquired can be selected from the *settings* sub-window. The AOTF settings, which allow to select the active laser lines, can be accessed by the *filters* sub-window.
A message log can be consulted for following operational status of the system and possible debug.

SPIMLab has two running modalities. In *free run*, the system displays real-time images of the selected channels (maximum 2 per computer) on the main window and can be used to optimize acquisition parameters and to find the edges of the sample. These edges positions can be used as absolute coordinates for the acquisition in *acquisition* tab (x,y *from … to …*). The *acquisition* button starts an acquisition of the selected channels. A typical acquisition starts acquiring data from the top left corner of the sample. The sample is then moved by the stages in a linear pattern from top to left on the *x* axis and top to bottom on the *y* axis. The x position of the stage is reset to the starting point after each line acquisition terminates. The movement speed and, thus, the sampling on the x/z direction, can be set by changing the *step* value of the *x* axis in the acquisition tab. Similarly, the overlap between two adjacent x lines can be set by changing the *step* value of the *y* axis in the acquisition tab. A 10% overlap between two x lines is recommended for correct post-processing alignment of the images. The system shown in Figure 24 has a 1 mm field of view. The *y step* has been set to 0.9 mm, resulting in a 10% overlap of two successive x lines.
The software automatically calculates the number of frames along the *x* axis and the number of iterations of an horizontal line along the *y* axis based on the acquisitions coordinates set by the user.
The *x* stage moves at a constant speed during the acquisition, resulting in a small skewing of the image pixel frames from the top to bottom of the image. In practice, as the sample is constantly moving, the light-sheet illuminates a slightly displaced portion of the sample while the frame is recorded. However, considering the slow-moving speed compared to the frame rate (45-46 Hz), and the 0.5-1 ms exposure time, this effect remains neglectable.

The software on the slave computer was modified to only display the frames of camera 2 and 3 during free-run operation, and to save the respective data when an acquisition is started from the master side.

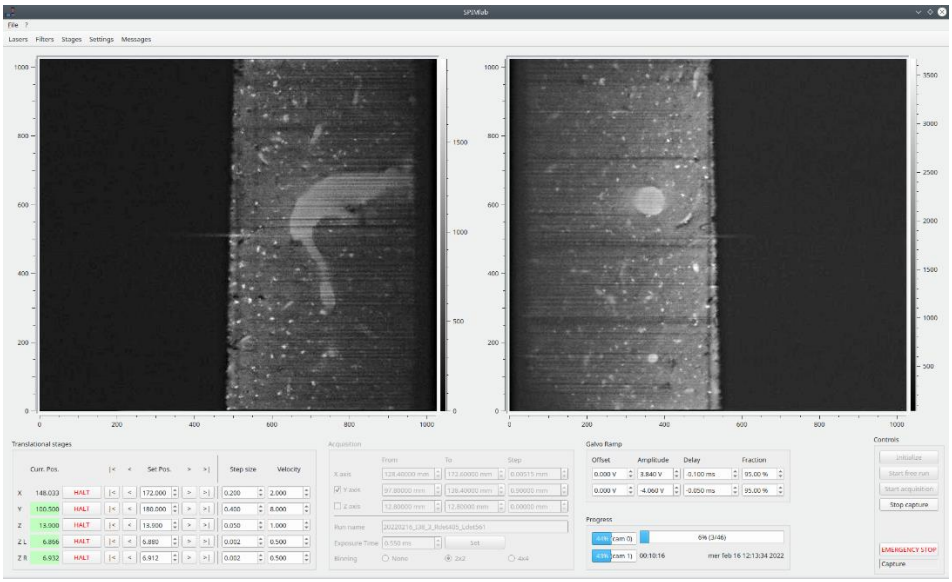


*Figure 25. SPIMLab GUI showing the two camera frames during an acquisition of a cleared human brain 500 µm thick slab on an inverted-dual-SPIM setup.*

## 3.7 Image reconstruction

The raw data is saved during each acquisition in the folder selected by the user in the *acquisition* tab. Every horizontal scan is saved into a new multi-tiff file for each camera and its name contains the stage xyz coordinates. A second file containing the scan metadata is saved in .mhd format for each multi-tiff raw file. This file contains the necessary data for correct image reconstruction by the dedicated software (Figure 26).

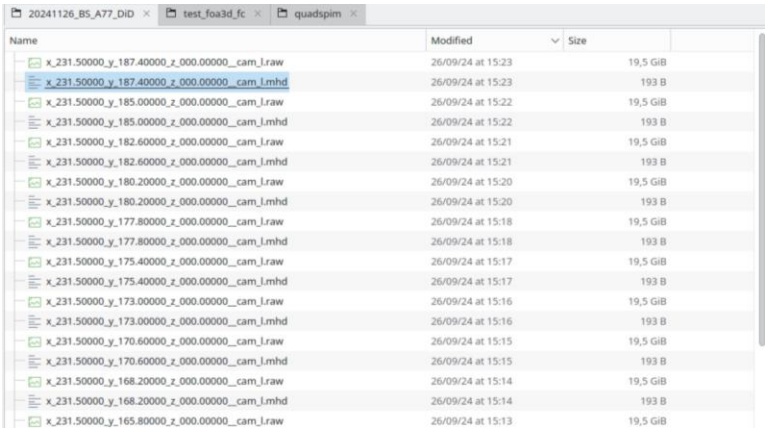


*Figure 26. Files saved during an acquisition from one camera. Each horizontal scan line is represented by a file. Note that the starting x coordinate does not change in the file name, as the starting point on the x axis is unchanged. Oppositely, the y coordinate changes of the user-set value, corresponding to the y displacement for each new line (2.4 mm over a 2.66 mm FOV).*

Multi-tiff raw data contains a large number of frames which represent the light-sheet illumination plane captured by the detection objective in a single horizontal line. However, these images cannot be used for image reconstruction before undergoing a deskewing process. Those images are oriented on the detection objective focal plane, which is 20° tilted in respect to the sample holder and specimen plane. In order to be stitched and obtain a real 3D image of the sample, every horizontal multi-tiff file from an acquisition requires to be retrieved from the illumination plane to the specimen plane through a pixel position re-assignment process by affine transformation and rotation (deskewing). A Python script developed by LENS department, named DualSPIM-reslice, has been used for this operation (https://github.com/lens-biophotonics/biolabtools/tree/master/biolabtools). In addition to deskewing, the script is also capable of performing a scaling of voxel size to achieve an isotropic value. As the axial resolution in a microscope is generally lower than lateral as an effect of diffraction, the script is designed to undersample the lateral voxel size and match it to the axial voxel size (Mazzamuto et al. 2023).

After the deskewing process, image stitching is performed by a custom software developed by LENS department, ZetaStitcher (Mazzamuto et al.

2023). The software was entirely developed in Python and is available at https://github.com/lens-biophotonics/ZetaStitcher. The software has already been used to process the data obtained from the inverted-dual-SPIM previously mentioned (Costantini et al. 2023) and it is capable of stitching files counting up to $10^{12}$ voxels. ZetaStitcher operates the stitching of every horizontal scan line overlapping each other by 10% along the y axis by pixel averaging. The resulting file is a multi-page tiff z-stack where all the frames are aligned with the sample plane (Figure 27). These operations are repeated for each channel.

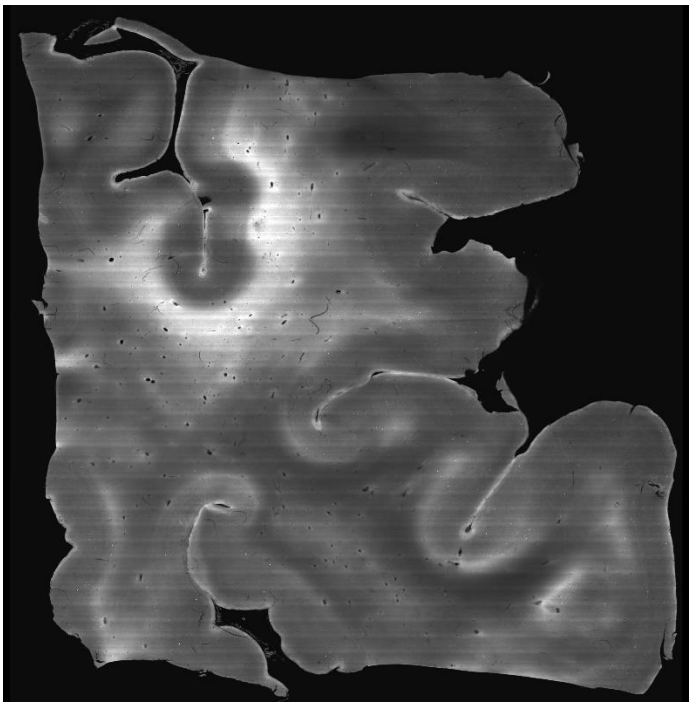

*Figure 27. Single z-slice after reslicing and stitching process.*

## 3.8 System alignment

An accurate alignment of the optical paths is a key requirement for obtaining quality data and evaluating the performance of an imaging apparatus. In particular, the correct alignment of the illumination laser beams is crucial in this system, as a slight misalignment could deny the beams to reach the back focal aperture of the objective in a sub-optimal position. This would lead to uneven illumination, a mismatch of the position of the light-sheets with the detection objective focal plane and make the camera rolling shutter synchronization with the digitally scanned sheets impossible.

### 3.8.1 Illumination path alignment

As mentioned in Paragraph 3.1.1, the four laser beams are aligned and combined with the help of iris 1 and 2 (Figure 17) in order to enter the AOTF in the same spot and with the same angle. This alignment is achieved by turning the two mirrors positioned right after each laser output. However, this alignment is not the most crucial in the illumination path. A crucial condition for correct alignment of the four beams onto the galvanometric mirror, consists in the four beams to be perfectly aligned and overlapping when entering the refraction prism. To achieve this, the effect of refraction of light when passing through the AOTF has to be considered. In fact, as discussed in Paragraph 3.1.2 and 3.2.3, an AOTF acts as a diffraction grating, thus imposing a different exit angle to different wavelength beams. This causes the four combined incident beams to be refracted at different angles at the exit of the AOTF, leading to a misalignment onto the entrance spot on the diffraction prism. This misalignment can be addressed with the help of iris 3 and 4 and the two mirrors in front of each laser. The operation causes the beams to enter the AOTF at slightly different angles, but they can be adjusted to result overlapped and aligned at the entrance spot of the diffraction prism. In practice, iris 1 and 2 are only used for coarse alignment of the beams onto the AOTF entrance.

The diffracted beams leaving the diffraction prism are projected onto the galvanometric mirror through a system of three silver mirrors which are used to align the beams between iris 5 and 6, respectively in front of the scan lens and in front of the illumination objective tube lens. The two lens can be removed when performing alignment. Galvanometric mirror is set to home position during the operation and only the first (647 nm) beam entering the illumination objective FOV is used. The camera 0 trigger (far red channel) is synchronized with the start of the galvanometric mirror ramp and corresponds to the home position of the 647 nm laser beam on the sample and, thus, on camera 0 sensor.

A mirror can be inserted after the galvanometric mirror to deviate the beams onto a wall of the room to check the correct alignment of the four beams. In optimal condition, the beams are aligned on the same plane, corresponding to the *y* plane of the illumination optical path (Figure 28). When not showing perfectly aligned, the beams can be finely adjusted by using the two mirrors in front of each laser.

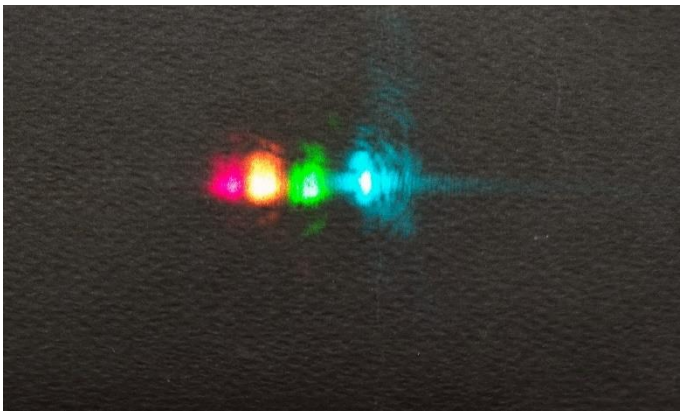

*Figure 28. Projection of the four beams on a cardboard placed 4 meters away from the galvo mirror, showing correct alignment of the beams on the illumination y plane.*

### 3.8.2 Detection path alignment

Camera 0, (far-red channel) was chosen as a reference for the alignment of the detection path as light travels straight from the detection tube lens to the camera sensor, with no reflections involved. Only the two dichroic mirrors between the camera and tube lens add a slight deviation from the original axis, which can be corrected by a slight lateral displacement of the camera on *x* axis.
During the detection path alignment with a test sample, the system was set on *free run* mode and the images from cameras were displayed on the monitors. Each computer of the system is equipped with one monitor where the two respective camera images are being displayed on SPIMLab.

Placing the camera on the exact focal plane of the tube lens is critical to ensure that the detection objective focal distance is exactly 4.8 mm.
For a precise positioning of the camera, an object placed 4 meters away in front of the tube lens was imaged on the camera sensor. The camera was moved on the z axis of the optical path by adjusting the manual stage until optimal focus was reached in the displayed image. If an object at infinite is focused by a lens on a sensor, the focal distance between the lens and the camera is then optimal.

Once correctly aligned, the z position of camera 0 should not be moved to correct image focus. Conversely, the detection objective should be moved along the z axis by actioning the piezo stage from the software.
Afterwards, the alignment of camera 1, 2 and 3 has been completed by adjusting the z manual stage of each camera.

Next, camera height (image *y* position) and lateral displacement (image *x* position) were adjusted by actioning the respective camera manual stage.

### 3.8.3 Objectives alignment

Correct alignment of the objectives is achieved by acting on the manual *z* stage of the illumination objective and their respective *xy* manual stages. The two 50 mm round mirrors between the objectives and their respective tube lens, mounted on the vertical breadboard, are used to align the incident beam on the back focal aperture of the illumination objective with the help of a removable iris screwed on the back of the objective. Similarly, the two silver mirrors behind the detection objective, are used to center the fluorescent light entering the tube lens. Figure 29 shows a view of the objectives' assembly.

Centering the light-sheet waist in the detection objective FOV is crucial for achieving the best illumination condition, namely the highest axial resolution. As the axial resolution of the system is strictly dependent on the light-sheet thickness, having the illumination beam waist at the center of the detection objective FOV is fundamental. To obtain this, the galvanometric mirror was set to a still position in such a way that the beam waist (647 nm laser line) resulted in the middle of the FOV in the image. Afterwards, the position of the waist *z* stage of the illumination objective was adjusted to the optimal position by acting on the manual *z* stage of the objective. The beam waist focus can be adjusted by either tuning the *y* knob of the *xy* stage of the illumination objective, or adjusting the focus of the detection objective by moving the piezo stage.

The image is centered on the camera sensor by adjusting the two mirrors between the detection objective and its tube lens while looking at a test sample on camera 0 (reference camera) in *free run* mode. After achieving the ideal positioning of the image on the far-red camera, the optimal position of the remaining cameras can be achieved by tuning their *xy* position by moving the respective manual stages while looking at the sample in *free run*.

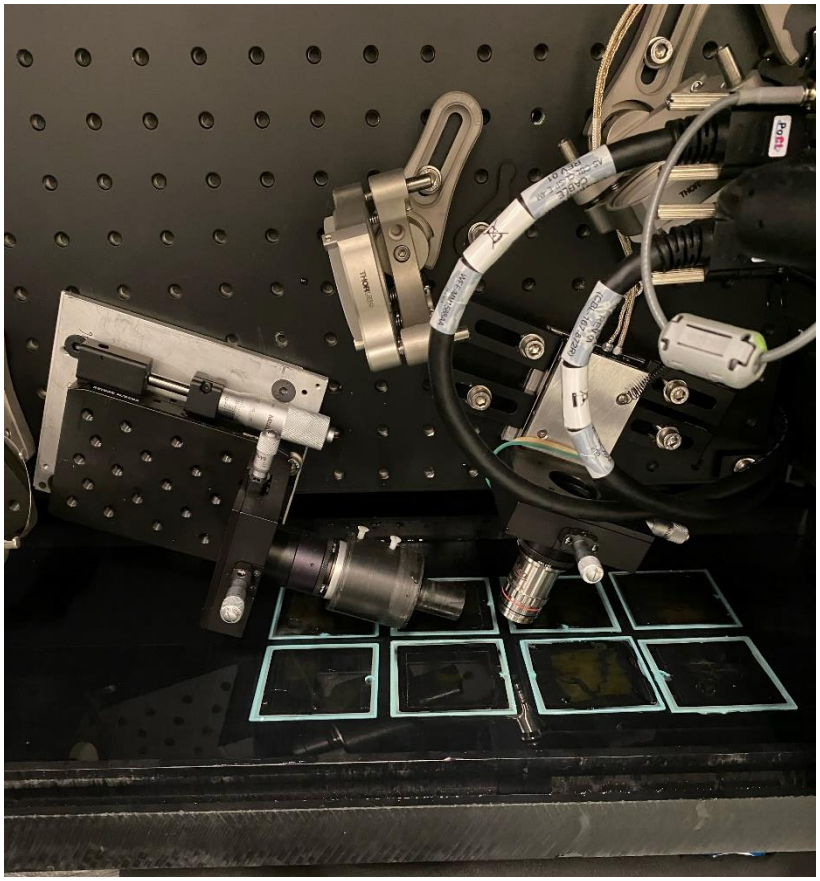

*Figure 2928. Close-up view of the objectives' assembly. Eight samples have been placed in the imaging chamber.*

## 3.9 Synchronization of beams with camera shutters

Synchronization of each of the four excitation beams with the respective channel camera rolling shutter is a key feature of the system.
This was achieved by adding a small temporal delay between the camera triggers, which can be set from SPIMLab main window. This feature was specifically added to the SPIMLab version dedicated to the system (Figure 30).

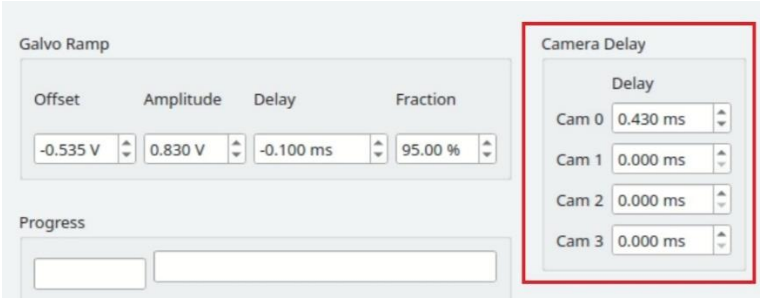


*Figure 30. A "Camera Delay" tab in the main window of SPIMLab allows to set the camera trigger delays.*

The diffraction prism imposes different exit angles to different wavelength beams. As a consequence, the angular distance between each following beam reaching the back focal aperture of the illumination objective, is different. The three delays between the beams result different and need to be adjusted carefully to obtain the optimal synchronization with the shutters.
The value of each delay was found for each channel by trial-and-error for each camera while imaging a test sample in *free run* mode. The 647 nm beam is the first entering the detection objective FOV and the camera 0 trigger goes high simultaneously with the ascending ramp of the galvanometric mirror, starting the registration of the far-red channel image. After the 647 nm channel trigger, the successive three start by the delay set on the software. As each beam enters the FOV of the camera, its trigger goes *high* and the respective camera starts recording an image.

The galvanometric mirror ramp time and slope are calculated by SPIMLab taking into account the exposure time and the sweeping angle (delta V) specified in the settings (Figure 31).

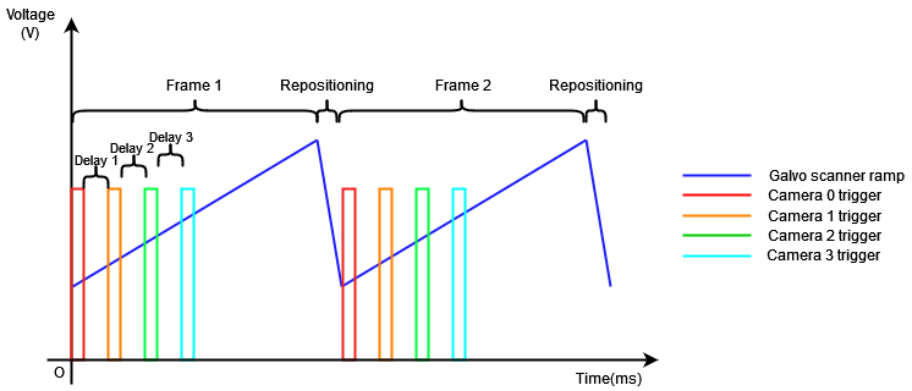


*Figure 31. Graphical representation of galvanometric mirror ramp and camera trigger generation. The far-red camera trigger starts at the same time of the ramp as it represents the first beam illumination the sample. Successively, the other channels camera triggers go high at the set delay and start the acquisition of a frame.*

Four digitally scanned light-sheets are generated onto the samples, slightly separated by a temporal and spatial delay to avoid cross-talk between the channels. This peculiar design allows to record four channels at the same time for each sweep of the galvanometric mirror.

## 3.10 Sample preparation

Human brain tissue slices have been optically cleared with the SHORT protocol (Paragraph 2.3.4) and mounted between a 60x60x1 $mm^3$ optical glass slide and a 60x60x0.1 $mm^3$ quartz slide (RI = 1.46) before imaging.

Human brain tissue slices, previously fixed in formaldehyde, have been cut with a vibratome and optically cleared and stained with the SHORT protocol as follows (Figure 32).

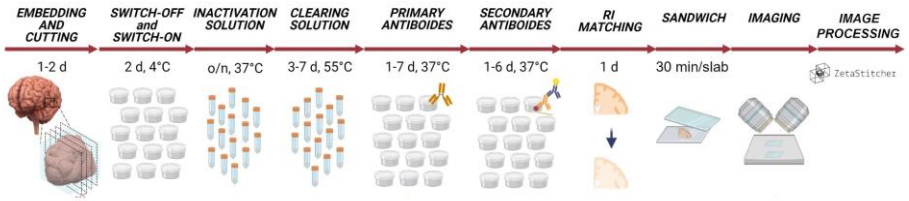


*Figure 32. Schematic of the SHORT protocol phases ('Author Spotlight: Advancing 3D Cytoarchitecture Analysis - Rapid Volumetric Reconstruction of the Human Brain', n.d.).*

*Cutting process*

Samples were embedded into a 4% w/v agarose in PBS pH 7.4 and stored at 4 °C for 24h before cutting. The agarose blocks are then glued to the vibratome support and cut into 500 μm thick slices.
After cutting, the slabs were placed into a PBS 1X pH 7.4 and 0.01% w/v Sodium Azide ($NaN_3$) preserving solution and stored at 4°C.

*Fixation and inactivation*

For homogeneous tissue clearing, the samples need to be transformed into a heat- and chemical-resistant hybrid. For this purpose, a SWITCH-OFF solution is used to firstly disperse the inactivate fixative and a SWITCH-ON is then used to start the fixation process. This relies on the pH sensitivity of glutaraldehyde.

The SWITCH-OFF solution is made in 50% PBS titrated to pH 3.0 with HCl, 25%  0.1M HCl, 25% potassium hydrogen phthalate (KHP) and 4% glutaraldehyde (from 50% stock solution in water). The SWITCH-ON solution consists of PBX 1x pH 7.4 and 1% glutaraldehyde. These solutions need to be fresh prepared under fume hood on ice due to glutaraldehyde toxicity and in dark environment due to its light-sensitivity.
Samples are incubated in the SWITCH-OFF solution at 4 °C for 24h in dark with gentle shaking. Afterwards, samples are incubated in the

SWITCH-ON solution at 4 °C for 24h with gentle shaking in new containers.

To stop the fixation process, an inactivation solution is used. The inactivation solution is prepared with PBS 1X pH 7.4, 4% w/v acetamide, 4% w/v glycine and titrated to pH 9.0 with sodium hydroxide (NaOH) 1M; stock solution can be stored at 4°.
After the SWITCH-ON process, the samples are washed 3 times for 2 hours in PBS 1X pH 7.4 at RT with gentle shaking.
Samples are then incubated in the inactivation solution overnight at 37 °C in a water bath.

After the inactivation, the slabs are washed 3 times for 2 hours in PBS 1X pH 7.4 at RT with gentle shaking.

*Delipidation*

For the delipidation process, samples are incubated in a clearing solution at 55 °C for 6 days. The solution is composed of 200 mM SDS, 20 mM sodium sulfite ($Na_2SO_3$) and 20 mM boric acid ($H_3BO_3$) titrated to pH 9.0 with NaOH 1M. During the incubation period, the solution must be changed every two days. Stock solution can be stored at RT.

*Immunostaining*

After the clearing process, samples need to be washed from SDS and quenched to limit tissue autofluorescence. Antigens also need to be retrieved before antibody staining.
Samples are washed three times during the day at 37 °C with shaking in pre-warmed PBST solution (PBS 1X and 0.1% v/v Triton X-100). The last wash is extended overnight.

For quenching the tissue autofluorescence, the day after, hydrogen peroxide (H2O2) 30% w/w is added to the sample and kept shaking for 45'.
Three 10' washes in PBS 1X pH 7.4 at RT follow this step.

For antigen retrieval, a stock solution is prepared: 10mM Tris base, 1mM EDTA and 0.05% v/v Tween 20, titrated to pH 9 with NaOH 1M. The solution is pre-warmed at 95 °C in tubes inserted in a water bath.
Samples are transferred into the antigen retrieval solution and left at 95 °C in a water bath for 10'.
The tubes containing the samples are then removed from the bath and let cool to RT with gentle shaking. The samples are then equilibrated in PBS at 4 °C before immunostaining.

The antibody solution is prepared in PBST with the addition of $NaN_3$ 0.01% w/v. Samples are incubated at 37 °C for a week in the primary antibodies' solution.
After a week, samples are washed in pre-warmed 37 °C PBST 3 times for two hours with gentle shaking.
Secondary antibodies are added to PBST with $NaN_3$ 0.01% w/v. Slabs are then incubated for six days in secondary antibodies, protected from light, at 37 °C.
After staining, samples are washed in pre-warmed 37 °C PBST three times during the day with gentle shaking. The slabs can be left in the last was solution.

*Refractive index matching*

Before sample mounting and imaging, the refractive index must be matched to the RI of the cover glass and immersion liquid (1.46). This allows to minimize the effect of refraction during the imaging, improving light penetration and thus imaging depth and quality.

A 30% v/v 2,2'-thiodiethanol (TDE) with PBS 1X solution is prepared and samples are transferred there and incubated for 4 hours at RT.
Samples are then moved in a 68% v/v TDE solution in PBS 1X (RI = 1.46) and left there at RT for the weekend. Slices can be stored for a long time in this solution at RT and protected from light.

*Sample mounting*

The slabs are mounted between a 60x60x1 mm glass slide and a 60x60x0.5 mm quartz coverslip, separated by a 56x56x0.5 mm stainless steel spacer.

The two slides are glued with a double component glue in a 1:1 ratio and the inner cavity, containing the sample, is filled with 68% v/v TDE solution in PBS 1X.
The refractive index of the sample, sample mounting medium, coverslip and immersion medium in the imaging chamber are matched and equal to 1.46. This represents the optimal imaging condition.
The mounted samples are now ready to be imaged and can be stored in darkness at RT for a long period (Figure 33).

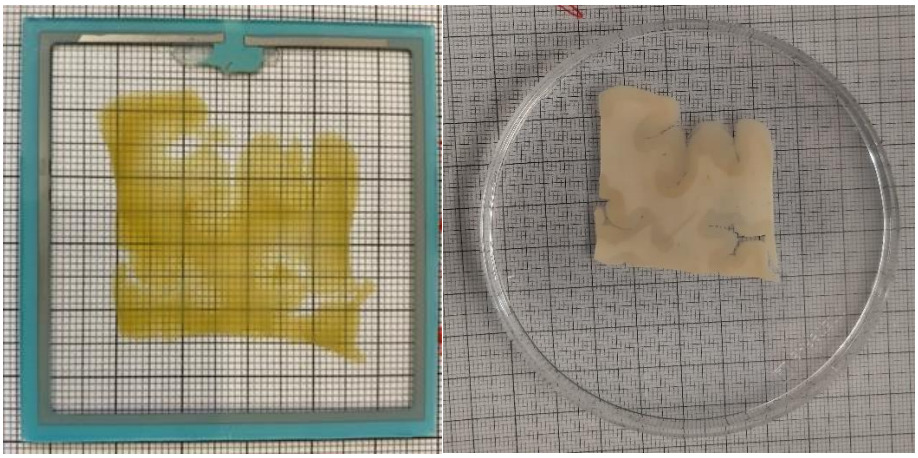

*Figure 33. A human brain Broca's area slice before (left) and after clearing with SHORT (right). The right image shows the slice mounted between the glass slide and quartz slide.*

# 4. Results and discussion

Following the assembling and alignment processes, the system was characterized and its performance evaluated on test samples. A view of the setup is shown in Figure 36.


*Figure 36. Panoramic of the quad-SPIM setup.*

## 4.1 System characterization

Evaluating the performance in terms of resolution and speed of an imaging apparatus is crucial for defining its possible applications. As previously mentioned, the aim of this project is to achieve a significant improvement

in acquisition speed in comparison with the state-of-the-art dual-inverted SPIM already in use at LENS Department. For the purpose, the light-sheet properties have been calculated and the resolution of the system was measured.

### 4.1.2 Light-sheet thickness

While the lateral resolution of a LSFM is strictly dependent on the detection objective's NA according to the Rayleigh criterion (equation 1.3), its axial resolution is defined by the light-sheet thickness (Figure 4) when the latter is smaller than the theoretical axial resolution calculated by equation (1.4).

The theoretical light-sheet waist thickness can be calculated by (1.1) as follows:

$$R_{ill\text{-}axial} = 2\omega_0 = 2\frac{\lambda f}{\pi D} = 2\frac{0.488 \cdot 56300\ \mu m}{3.14 \cdot 700\ \mu m} = 25 \pm 0.1\ \mu m$$

For an excitation wavelength corresponding to 488 nm. As the beam waist thickness of a focused beam is dependent on wavelength of light, this results in a $33.1 \pm 0.1$ μm waist when focusing a 647 nm wavelength light through the illumination objective. As a consequence, the light-sheet waist of the system ranges from $25 \pm 0.1$ μm to $33.1 \pm 0.1$ μm depending on the laser line.

The theoretical axial resolution of the detection objective, can be calculated according to (1.4):

$$R_{det\text{-}axial} = 1.78\frac{n\lambda_{em}}{NA_{det}^2} = 1.78\frac{1.46 \cdot 0.52\ \mu m}{0.15^2} = 60 \pm 0.1\ \mu m$$

Calculated for an emission wavelength of 520 nm (green channel).

Analogously, we can calculate the theoretical axial resolution in the far red channel (692 nm central wavelength emission):

$$R_{det\text{-}axial} = 1.78\,\frac{n\lambda_{em}}{NA_{det}^2} = 1.78\,\frac{1.46\ \cdot\ 0.692\ \mu m}{0.15^2} = 79.9 \pm 0.1\ \mu m$$

The theoretical calculations demonstrate that the beam waist generated by a 0.7 laser beam focused by the illumination objective range from $25 \pm 0.1$ µm to $33.1 \pm 0.1$ µm, demonstrating an improvement in axial resolution by a 2.4 factor compared to the detection objective theoretical axial resolution.

In order to achieve homogeneous axial resolution, the confocal parameter of the light-sheet needs to cover the 2.66 mm FOV of the detection objective.
The confocal parameter of the light-sheet for a 488 nm wavelength excitation beam can be calculated according to (1.2):

$$b = 2Z_R = 2\,\frac{\pi\omega_0^2}{\lambda} = 2\,\frac{3.14\ \cdot\ (25\ \mu m)^2}{0.488\ \mu m} = 2010 \pm 0.1\ \mu m$$

For an excitation wavelength corresponding to 647 nm we can find a confocal parameter value of $2665 \pm 0.1$ µm, which equals the detection objective's FOV.

As expected, the confocal parameter results smaller at shorter wavelengths. However, despite resulting 0.65 mm lower than the detection objective's FOV, a confocal parameter of $2.01 \pm 0.01$ mm is adequate for homogeneous illumination.
The maximum sample thickness which can be imaged by the system is a function of the detection objective's FOV and the light-sheet incidence angle in respect of the sample holder (Figure 37). This can be calculated by:

$$h = FOV_{det} \cdot \sin 20° = 2.66 \text{ mm} \cdot \sin 20° = 0.91 \pm 0.1 \text{ mm}$$

When imaging with lower wavelength excitation light, the confocal parameter is smaller than the detection objective's FOV. However, the system was designed to image 500 µm thick slices of brain tissue. As a consequence, according to the above calculations, the resulting confocal parameter is compatible with the samples' thickness.

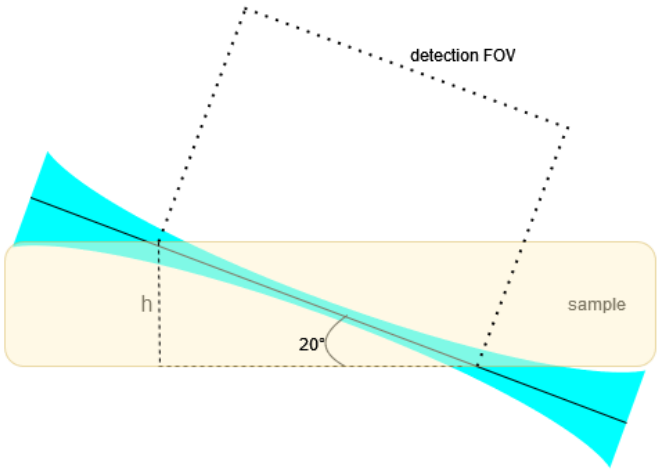


*Figure 37. Representation of the relation between the detection objective's FOV and maximum sample thickness h.*

### 4.1.3 Experimental evaluation of the point spread function of the system

The point spread function (PSF) is a function that describes how an imaging system responds to a point light source or point object, effectively serving as the system's impulse response (Sheppard & Choudhury, 1977). It represents the distribution of light from a single point emitter as it propagates through the optical system and forms an image, which is not represented by an ideal point but, conversely, a blurred spot which assumes a peculiar intensity profile, the Airy disk (Figure 38, top).

Diffraction plays a central role in shaping the PSF and, consequently, affects the resolution of an optical system. The sum of the effects of diffraction and imaging conditions which lead to the formation of the PSF, are referred to as *convolution*. This spreading effect limits the ability of the optical system to distinguish between two closely spaced points, a concept known as the diffraction limit (Abbe, 1873) and lately defined by Rayleigh through equations (1.3) and (1.4).

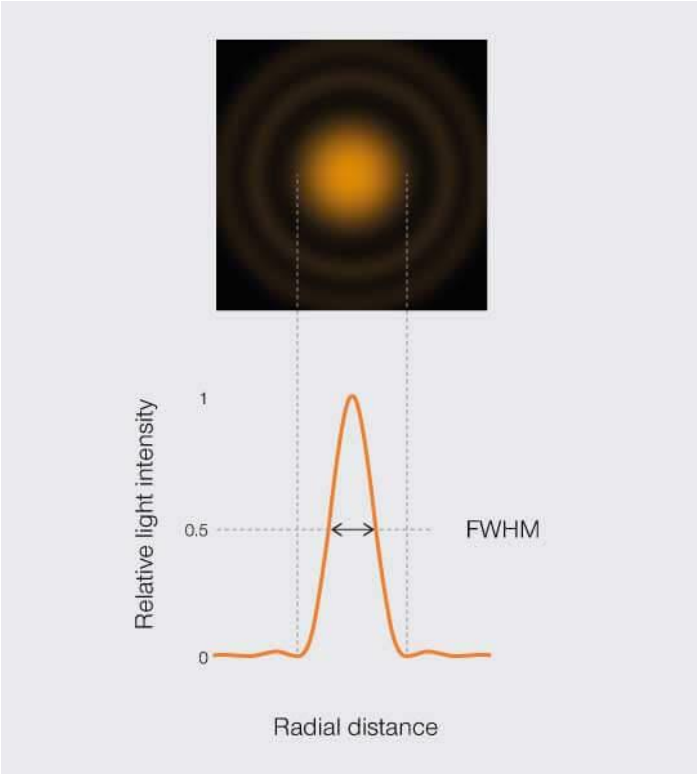


*Figure 38. Top view and intensity profile of an ideal PSF of a point light source affected by diffraction ('How to Measure Resolution? Part Two!', n.d.).*

Theoretical calculations provide an important overview of the most important features of an imaging system, like its resolution and speed. However, the experimental measurements of such parameters can significantly diverge from the theoretical results as a consequence of a variety of hard-to-evaluate variables. In addition to diffraction, spherical and chromatic aberrations caused by imperfections in optics, slight misalignments in the optical paths and the variability of the structure of the samples and imaging physical conditions, are just a few of the possible factors which can affect the resolution of an optical instrument.

The experimental measurement of the point spread function (PSF) represents the gold standard procedure to evaluate the actual resolution of a system under routine imaging conditions. By doing so, the measured PSF

will be the result of the effects of diffraction and other unpredictable factors affecting the convolution of the image through the optical system.

For a correct measurement, sub-diffraction sized fluorescent beads have been used as point light sources. For a comparison, two different sized beads have been used: 500 nm and 1000 nm fluorescent spheres (TetraSpeck, Invitrogen) have been diluted to a 1:10000 v/v concentration in the specimen chamber immersion medium (91% glycerol v/v, RI=1.46). The solutions containing the dissolved beads have been mounted between a square 60x60 $mm^2$ slide and a 60x60 $mm^2$ fused quartz coverslip as described in Paragraph 3.10.

The samples have been excited with each laser line and imaged in four channels for an accurate measurement of the PSF for each emission wavelength. The beads have been sampled with a 730 nm increment along the sample *x* axis, corresponding to a step size of 250 nm along the optical axis of the detection objective and a 686 nm displacement along the detection objective's *x* axis. As a consequence, the voxel size in the images corresponds to 1.3 μm in the *xy* axis and 0.25 μm on *z*. No binning was used on the camera sensors, resulting in a pixel size in the final image of 1.3 μm (Paragraph 3.3), thus representing a sub-optimal sampling according to the Nyquist criterion.

After the deskewing process (Paragraph 3.7), the intensity profile was projected on three lines drawn along the three axes of a bead and then measured with Fiji (https://imagej.net). Afterwards, a gaussian fit was performed on the intensity profile and the corresponding full width at half maximum (FWHM), which can be considered as the PSF, was measured for each axis of the bead. The measurement was performed over a total of 100 beads for each emission channel and each axis on both the 500 nm and 1000 nm diameter beads. The measurements resulting from each channel/axis were averaged to obtain the final value. The results are reported in Table 4.1.

| **1000** nm beads | | | | | | | | | | | |
|---|---|---|---|---|---|---|---|---|---|---|---|
| 488 nm | | | 561 nm | | | 594 nm | | | 647 nm | | |
| X | Y | Z | X | Y | Z | X | Y | Z | X | Y | Z |
| 3.9±0.25 | 2.6±0.31 | 8.7±0.58 | 3±0.17 | 3±0.11 | 6±0.36 | 3.5±0.15 | 2.9±0.17 | 7.4±0.54 | 3.4±0.2 | 2.9±0.19 | 7.4±0.44 |
| | | | | | | | | | | | |
| **500** nm beads | | | | | | | | | | | |
| 488 nm | | | 561 nm | | | 594 nm | | | 647 nm | | |
| X | Y | Z | X | Y | Z | X | Y | Z | X | Y | Z |
| 2.8±0.15 | 2.5±0.17 | 5.9±0.25 | 2.9±0.23 | 2.9±0.26 | 5.6±0.27 | 3.6±0.25 | 2.9±0.27 | 7.6±0.38 | 3.5±0.22 | 3.2±0.21 | 7.7±0.38 |

*Table 4.1. Average velues of the PSF measurements over three axes and in four channels. Values expressed in microns. Measurements error: $\pm STD$.*

The measurements show an anisotropic shape of the PSF of the system. In particular, an anisotropic value of the FWHM in the *xy* plane was registered. The most relevant discrepancy between the *x* and the *y* directions corresponds to 0.7 μm, in 1000 μm beads imaged in the green channel (488 nm excitation) and in 500 μm beads imaged in the orange channel (594 nm excitation).

This anisotropy could be a consequence of the presence of astigmatism in the detection path.

The axial resolution of the setup revealed to significantly exceed the theoretical estimate of light-sheet waist calculation (25-33.1 μm), resulting in values ranging from $8.7\pm0.58$ μm when imaging 1000 μm beads to $5.9\pm0.25$ μm when imaging 500 μm beads in the green channel. The $8.7\pm0.58$ μm axial resolution in the green channel represents an unexpected result, as it revealed lower than the other channels measurements. This is in contrast with the expected better resolution at lower wavelengths.

The smallest PSF in the three dimensions was registered in the green channel ($2.8\pm0.15$ μm along x, $2.5\pm0.17$ μm along y axis and

5.9±0.25 μm along the z axis) when imaging 500 μm beads, in line with expectations.
The expected theoretical lateral resolution, calculated according to (1.3), is 2.1±0.1 μm, 2.3±0.1 μm, 2.5±0.1 μm and 2.8±0.1 μm respectively for the 520 nm, 578 nm, 623 nm and 692 nm emission wavelengths.

Figure 39 shows a projection on the *xz* plane of a 500 nm diameter bead imaged in the green channel and its intensity distribution along the yellow line.

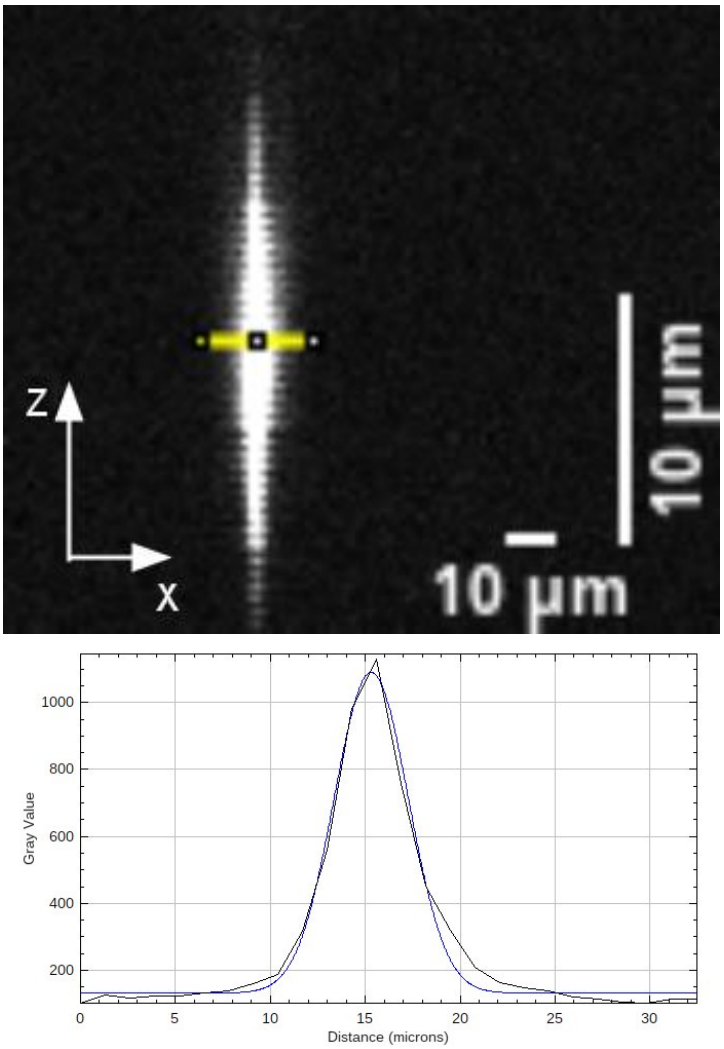


*Figure 39. Top: PSF image of a 500 nm bead imaged in the green channel, projection on xz plane. Bottom: Gaussian curve fitted to the intensity profile of the bead along the yellow line. Note: pixel size in the top picture is anisotropic as the image has only been deskewed, but not rotated in the sample plane.*

The discrepancy between the theoretical resolution calculations and the experimental results can be explained by the non-optimal sampling due to a 1.3 µm pixel size. In fact, according to the Nyquist criterion, a correct sampling of a signal or, as in this case, in an image, requires a sampling frequency at least twice as high as the highest frequency in the sampled signal. As a consequence, a more appropriate pixel size should not exceed

1.05 µm, corresponding to half the theoretical resolution value calculated for an emission wavelength of 520 nm. In addition, the presence of optical aberrations in the detection optical path can also negatively affect the result.

### 4.1.4 Signal-to-background calculation

The signal-to-background ratio (SBR) is a fundamental parameter that quantifies the ability to distinguish the desired signal from the background noise within an image. This ratio is crucial for assessing image quality and optimizing imaging conditions, as it directly impacts the visibility and quantification of microscopic structures or molecules of interest. The SBR is defined as the ratio between the mean intensity of the signal region and the mean intensity of the background region. It can be expressed as:

$$\text{SBR} = \frac{I_{signal}}{I_{background}} \qquad (4.1)$$

where $I_{signal}$ represents the average intensity of pixels within the region of interest (ROI) containing the specific signal, and $I_{background}$ is the average intensity of pixels in an adjacent area devoid of the signal, including the inherent background noise. To calculate the SBR, a ROI must be accurately delineated by selecting pixels that correspond exclusively to the signal. Similarly, the background region should be chosen carefully to ensure it is representative of the noise characteristics without contamination from the signal. High SBR values show a clear distinction between the signal and background, indicating the reliability of quantitative analyses and the detection of fine features within the image. It is important to note that in fluorescence microscopy, the SBR is largely influenced by the staining quantum yield, its specificity for the target and background autofluorescence of the tissue. A low-specificity causes the fluorescent probe to stain unwanted structures in the tissue, resulting in a higher background signal and a lower SBR. Similarly, tissue autofluorescence negatively affects SBR.

SBR was calculated on a 40x40 $mm^2$, 0.500 mm thick human brain Broca's area slab stained with NeuN primary antibody and AlexaFluor 647 secondary antibody. NeuN binds to a specific antigen in neuronal nuclei and perikarya. Data was acquired in 23' from the far-red channel with no binning on camera sensor. Figure 40 displays a MIP of the 3D volume after image reconstruction as described in Paragraph 3.7.

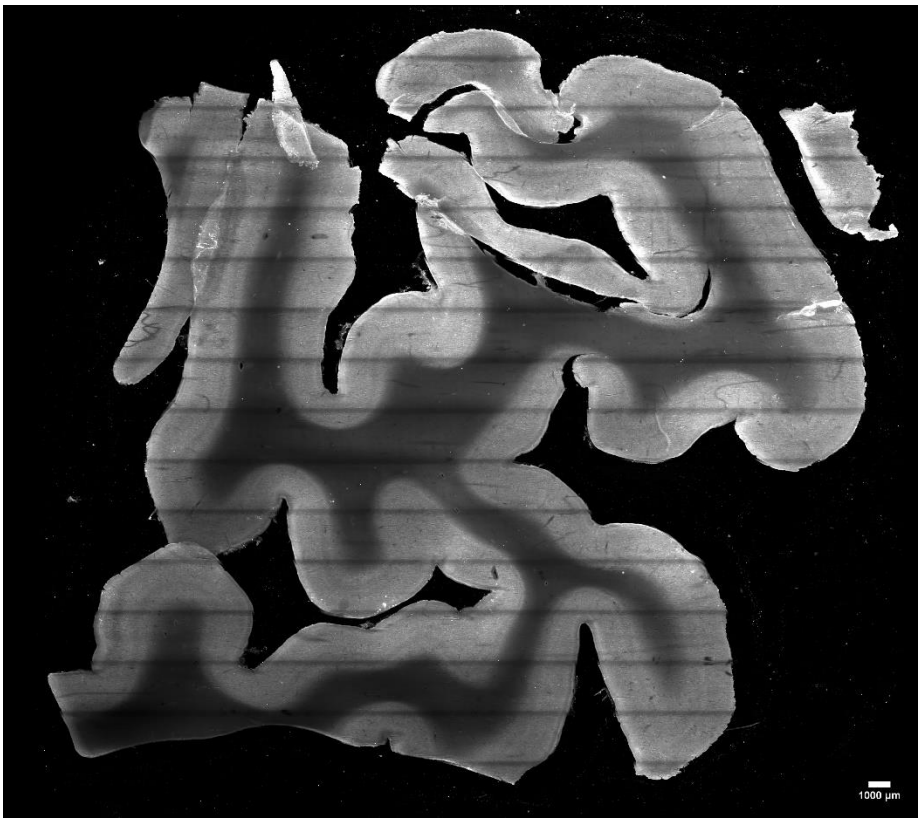


*Figure 40. Maximum intensity projection (MIP) of a human brain Broca's area slab stained with NeuN.*

To calculate the mean intensity signal value, 100 ROIs (e.g. ROI 1, Figure 41) were signal from neurons was present and the resulting mean was averaged to obtain the final value. For background mean intensity value, 10 ROIs (e.g. ROI 2, Figure 41) were selected where no signal from marked neurons occurred and their mean value was averaged to obtain the final value. The average mean value of signal resulted in $2312 \pm 1$ au and

the average calculated mean value of the background was 1360$\pm$1 au. As a result, the SBR in the image revealed to be 1.7$\pm$0.0015.

### 4.1.5 Signal-to-noise evaluation

The signal-to-noise ratio (SNR) in a signal or image is used to evaluate the clarity and quality of an image by comparing the level of the desired signal to the level of background noise. A high SNR indicates that the signal stands out distinctly from the noise, which is essential for accurate visualization and analysis of fine structures. The SNR can be defined as:

$$\text{SNR} = \frac{\mu_{signal} - \mu_{background}}{\sigma_{background}} \qquad (4.2)$$

Where $\mu_{signal}$ is the mean intensity of the signal region, $\mu_{background}$ is the mean intensity of the background region, and $\sigma_{background}$ is the standard deviation of the background intensity, representing the noise level.

The SNR was measured on the same ROIs used for SBR calculation. Standard deviation of the pixel values in the ROIs selected for background signal measurement in Paragraph 4.1.4 were averaged, corresponding to a final value of 83$\pm$1 au.

According to (4.2), SNR equals to:

$$\text{SNR} = \frac{2312\ au - 1360\ au}{83\ au} = 11.47 \pm 0.14$$

Figure 41 shows a ROI selected from the Broca's area sample used for SBR and SNR evaluation. Sub-ROIs 1 and 2 represent respectively an area where signal from a stained neuron was recorded and a background area, where no signal was present. All measurements have been performed in similar selected areas.

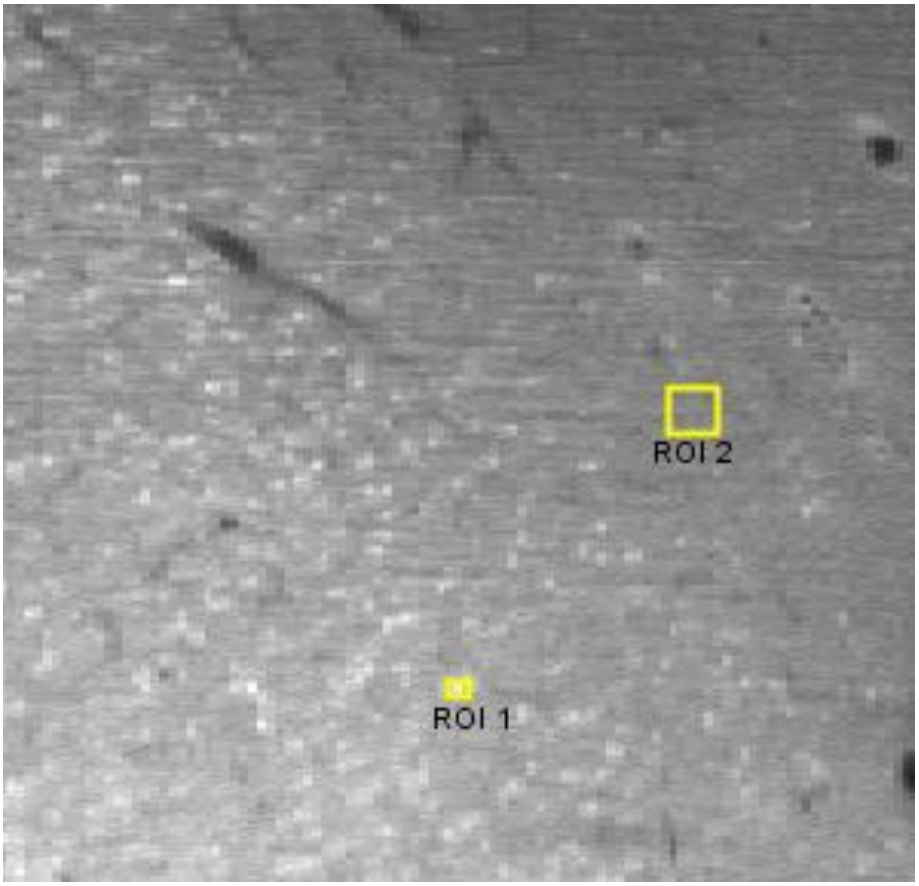


*Figure 41. Region of interest showing neurons labelled with NeuN primary antibody and AlexaFluor 647 secondary antibody.*

### 4.1.6 Evaluation of imaging speed

The imaging speed of the apparatus was evaluated and compared to the dual-SPIM by imaging a 40x40 $mm^2$, 0.5 mm thick human brain Broca's area cleared with the SHORT protocol and stained with NeuN, Calretinin and Somatostatin primary antibodies. The three primary antibodies were conjugated respectively with AlexaFluor 647, AlexaFluor 561 and AlexaFluor 488 secondary antibodies.
The sample was imaged with the two setups for a comparison of imaging speed.
The dual-SPIM at LENS was able to image the sample in three colors in a total of 4 hours and 35' in two subsequence two-channels acquisitions.
The quad-SPIM performance resulted in a 12-fold improvement in speed by acquiring the data in 23' with four channels simultaneously.
In terms of volumetric acquisition speed, the quad-SPIM performed a 2.1 $cm^3/h$ imaging speed in four colors in contrast to the 0.17 $cm^3/h$ of the dual-SPIM previously used by our group at LENS.
The results confirm a critical improvement in imaging speed.

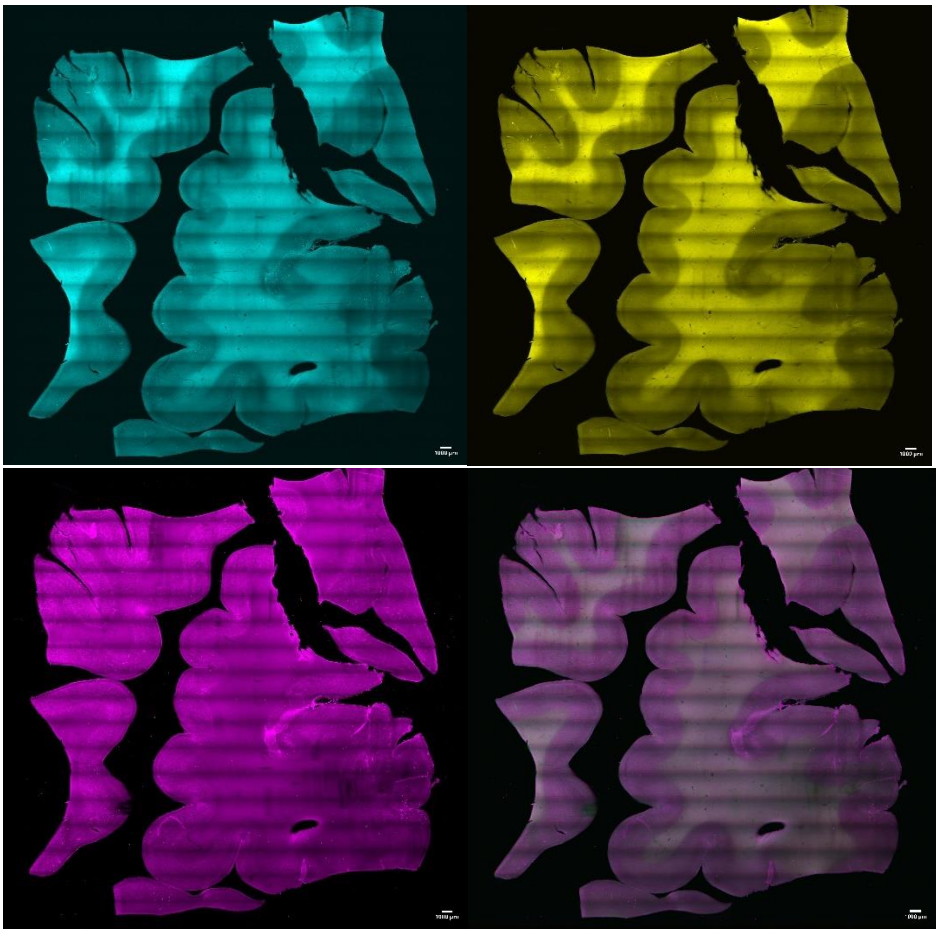

*Figure 42. Three colors MIPs of a human brain Broca's area stained with Calretinin (top left), Somatostatin (top right) and NeuN (bottom left) primary antibodies. Bottom right: three-channels fused image. Vertical stripes represent bleached areas in the sample. Horizontal artifacts have been caused by non-optimal stitching parameters.*

## 4.2 Evaluating fibers dispersion in brain stem tissue with Foa3D

A 500 µm thick slab of brain stem tissue was cleared with the SHORT protocol and stained with DiD (Invitrogen). DiD is a lipophilic dye which stains fiber bundles in brain tissue (Rosario, Howell, and Bhattacharya

2022). The sample was imaged in the far-red channel and, after image reconstruction, the dispersion of fibers was evaluated with Foa3D.
Foa3D is a tool developed by LENS Department, which can measure the fibers dispersion in three dimensions. Dispersion represents the grade of divergence of fibers in a volume.
The same specimen was imaged with the dual-inverted SPIM of the group for a comparison of the results. Figure 43 reports a MIP of the sample imaged through the two systems.

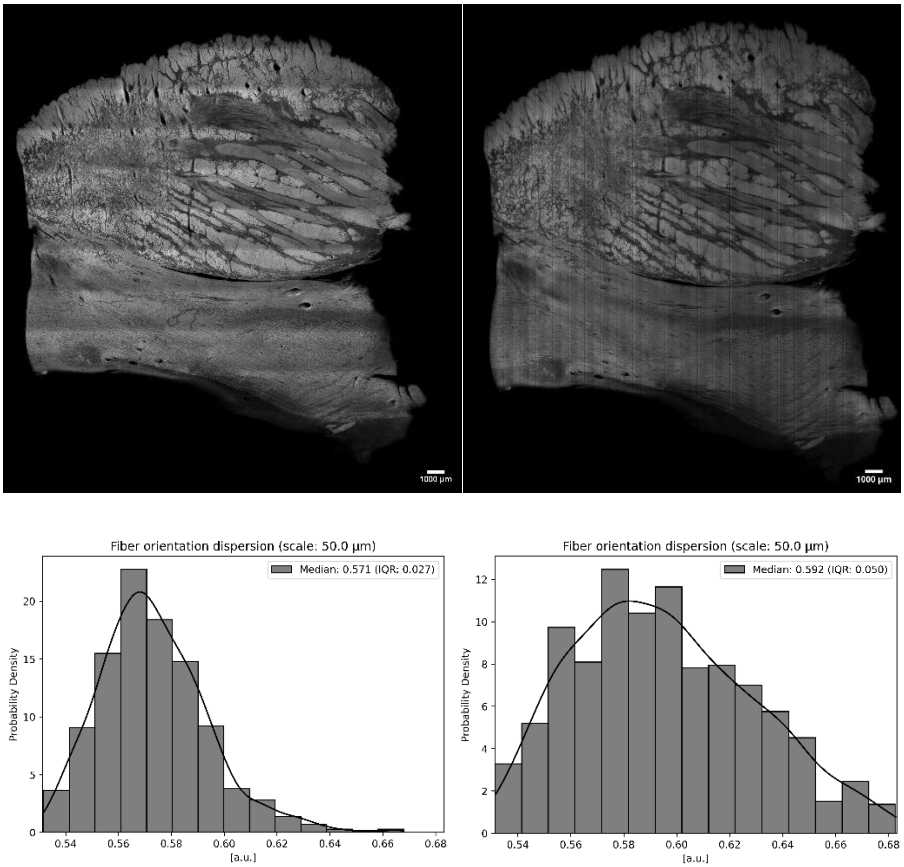


*Figure 43. (Top) MIPs of human brain stem slab imaged through the new apparatus (left) and with the dual-inverted SPIM (right). Below, fiber dispersion values distribution histograms calculated from above images.*

Foa3D analyzes a 3D volume and outputs a volume z-stack where the sampling voxel size in the original image is set by the user beforehand. A

sampling voxel size of 50 $\mu m^3$ was chosen for the analysis. With the processing, the software evaluates the dispersion in 50 $\mu m^3$ voxels and outputs a normalized voxel intensity value (between 0 and 1) inversely proportional to dispersion (Figure 45).

The resulting datasets were analyzed with the SciPy libraries (https://scipy.org/) by a custom Python script and their respective dispersion values distribution histograms were extracted (Figure 43, bottom). A normality test was performed to investigate the type of distribution of dispersion values. The result of a p-value lower than 0.001 ($5.69e^{-17}$ and $4.46e^{-6}$ for the dual-SPIM and quad-SPIM data) revealed that the distribution is not normal.

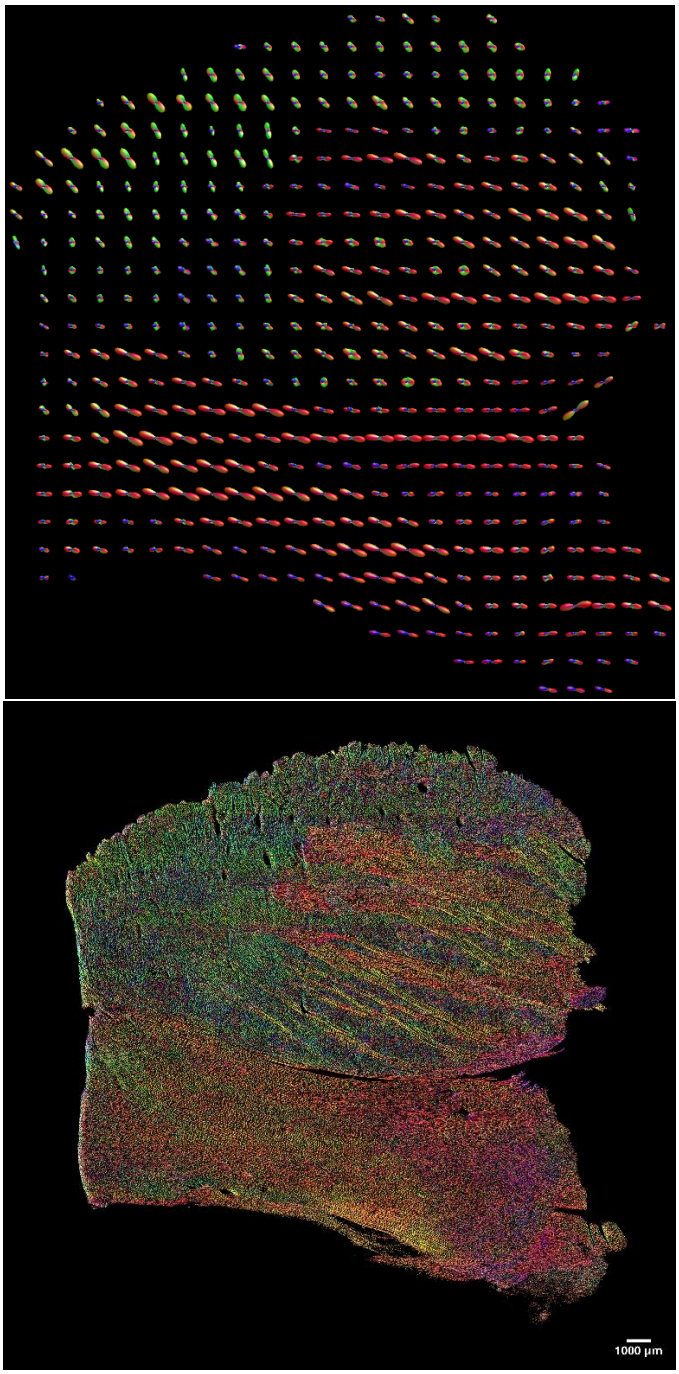


*Figure 44. (Top) Fibers ODFs in a sampling voxel size corresponding to 50 µm$^3$ for the quad-SPIM data (Figure 43, top left). (Bottom) fibers dispersion color map calculated for each voxel of the image.*

Figure 44 shows orientation distribution functions (ODF) calculated for 50 $\mu m^3$ voxels in the brain stem slice 3D volume. Multiple lobes appear in voxels presenting overlapping bundles (Sorelli et al. 2023).

For a comparative study between the two datasets, a Wilcoxon-Mann-Whitney test was performed (Fay and Proschan 2010).
The Wilcoxon-Mann-Whitney is a non-parametric statistical method employed to determine whether two independent samples originate from the same distribution. Unlike parametric tests (e.g. t-test), that require assumptions about the underlying population, the Wilcoxon-Mann-Whitney test operates on the ranks of the data rather than their raw values, making it suitable for ordinal or non-normally distributed data. The test assesses the null hypothesis that the probability of an observation from one population exceeding an observation from the other population is equal to 0.5. This is obtained by ranking all observations from both groups and then comparing the sum of the ranks between the groups. The resulting U statistic, derived from these rank sums, can be used to determine statistical significance through reference to the sampling distribution of U under the null hypothesis.

The determined U-value, from a "*two-sided*" hypothesis, was $3.75e^{-38,}$ assessing that the distributions are not equal. However, the Wilcoxon-Mann-Whitney test does not quantitatively evaluate the distance of two distributions. To quantify the grade of diversity of the two distributions, a Hellinger distance (Hellinger 1909) has been calculated. The possible output values can range between 0 and 1, where 0 represents identical distributions and 1 represents complete dissimilarity.
The resulting Hellinger distance was $0.32 \pm 0.016$, indicating a low grade of similarity. This result could be attributed to the presence of striping artifacts due to non-optimal image stitching which can interfere with Foa3D calculations of dispersion values from the dual-SPIM data.

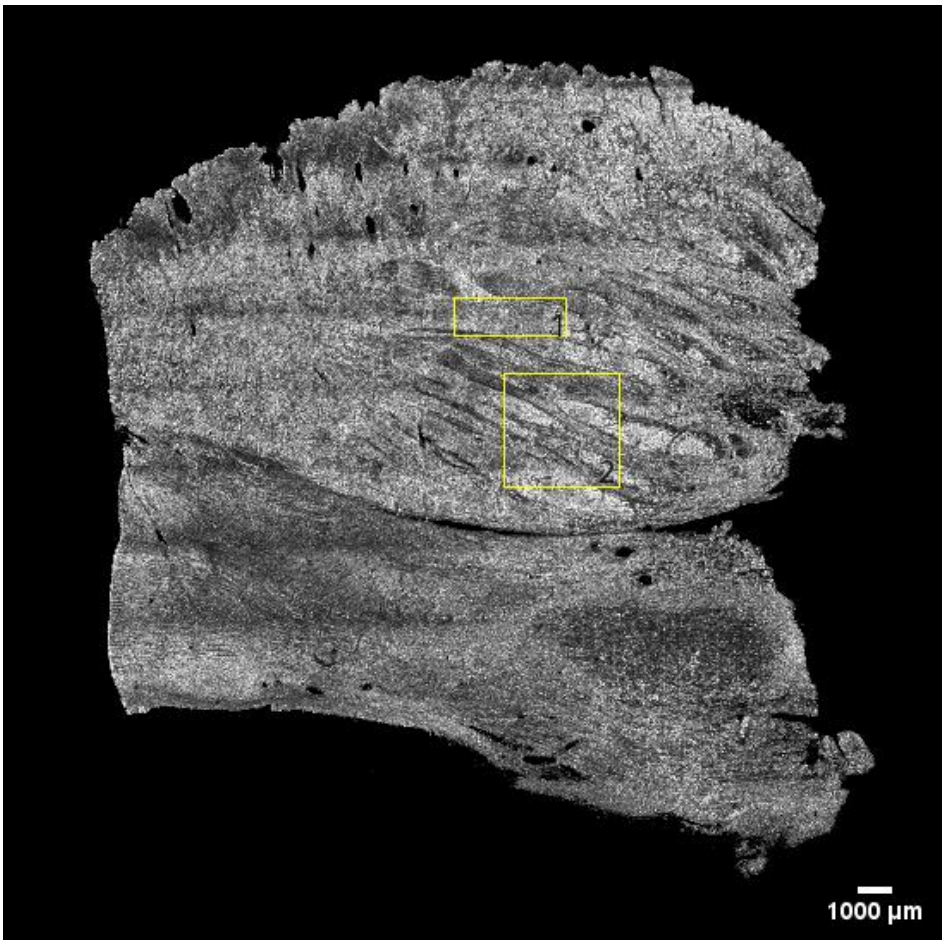


*Figure 45. Orientation Dispersion Index (ODI) representation calculated for a sampling voxel size corresponding to 50 µm³ for the quad-SPIM data. Pixel values range from 0 to 1, where 0 indicates the maximum dispersion. The indicated ROIs were used to evaluate dispersion difference in areas with qualitatively assessed low (ROI 1) and high (ROI 2) divergence.*

At a second time, two ROIs (Figure 45) have been selected from the quad-SPIM ODI data to quantitatively evaluate the dispersion in two areas respectively characterized by a high (Figure 45, ROI 2) and low (Figure 45, ROI 1) fibers divergence. The ROIs have been chosen by a qualitative assessment of the data as shown in Figure 43.
The dispersion distribution p-value in ROI 1 was $4.37e^{-6}$ and $4.82e^{-6}$ in ROI 2, indicating a non-normal distribution. Consequently, a Wilcoxon-Mann-Whitney test was performed on distributions from the two ROIs,

resulting in a U-value of $1.55e^{-46}$ from a "*two-sided*" hypothesis, indicating that distributions are highly dissimilar.
The resulting Hellinger distance between the two ROIs resulted in a value of $0.3 \pm 0.021$, assessing a low similarity. This result is in accordance with the dissimilarity expected in a comparison between regions characterized respectively by low and high dispersion.

## 4.3 Final considerations

The reported results show a significant advancement in imaging performance of LSFM, particularly in terms of speed.
The lateral resolution of the system, ranging from $2.6 \pm 0.31$ μm to $3.9 \pm 0.25$ μm, allows to image neurons at single cell scale. Axial resolution represents the main limitation of the system when imaging samples as thick as 0.91 mm. As discussed in Paragraph 4.1.2, fitting the illumination confocal parameter with the full FOV of the system, limits the light-sheet thickness. However, when imaging samples with a thickness lower than 0.91 mm, it would be possible to reduce the light-sheet thickness by enlarging the beam diameter entering the back focal aperture of the illumination objective, at the cost of a lower confocal parameter and FOV. This can be achieved by mounting a beam expander of the desired ratio in front of the lasers.
The SBR and SNR calculated values are suitable for performing solid image analysis to extrapolate relevant biological data from the images. Though, obtaining a high SBR remains a challenging task when imaging tissues showing high autofluorescence or when low specificity and low quantum yield markers are used. Sample preparation methods should always be optimized to limit these effects for optimal imaging conditions.
The evaluation of fibers' dispersion and its outstanding multicolor imaging speed showed the applicability of the system in investigating crucial biological questions about human brain structure and functionality in large tissue volumes.
Future improvements could take into consideration the addition of further excitation laser lines and the replacement of the illumination and detection objectives with custom high FOV and high NA ones to increase the

resolution of the system, according to research needs. However, employing higher NA objectives would limit the light-sheet confocal parameter and sample thickness.

# 5. Alignment and optimization of a dual-inverted SPIM

The Doctoral Programme in Atomic and Molecular Photonics includes a period of three months to be spent in a foreign institution. The period was spent at the Computational Brain Connectivity lab (CBClab, https://www.cbclab.org/) led by Professor Alard Roebroeck at the Faculty of Psychology and Neuroscience of Maastricht University, Netherlands.
The group focuses on human and mice brain studies, involving the imaging of cleared brain tissue. A dual-inverted SPIM for cleared tissue from ASI (Figure 46) is used for 3D multicolor imaging by the group.
During the permanence, the microscope was disassembled and moved to a different room, thus requiring re-assembling and re-aligning. Afterwards, imaging parameters and modalities have been optimized for multicolor imaging and confocal slit scanning was implemented. In addition, the stability and suitability of a multi-wavelength laser engine (CellX, Coherent) and a supercontinuum laser (SuperK, NKT Photonics) were measured and evaluated.

The ct-dSPIM microscope (Figure 46) is a modular light-sheet microscope developed by Applied Scientific Instrumentation (ASI) for high-resolution imaging of cleared tissue. This dual selective plane illumination microscopy system is designed to capture large biological samples, such as whole mouse brains or tissue slices, providing dual-view imaging. Utilizing ASI's modular components, including motorized stages and 2D micro-electro-mechanical mirror (MEMS), the ct-dSPIM enables the shaping and movement of a light sheet, which allows sub-micron resolution in 3D.
One of the peculiar features of the ct-dSPIM system is its flexibility due to is modular design. Two simultaneous colors can be imaged, light-sheet thickness can be adjusted with optional optics and the confocal-slit

modality can be used to enhance image contrast. It can achieve deep tissue imaging, up to 5 mm into flat samples. It is compatible with various refractive index media, ranging from aqueous to organic, thanks to the availability of custom objectives, which can fit the system specific imaging requirements. Excitation light is delivered to the system through optical fibers, allowing the use of ideally any external laser source. An electrically-tunable lens (ETL) at the exit of the fiber collimator, permits to finely correct the beam divergence and collimation when changing excitation wavelength. The microscope operates in either single-sided or dual-sided mode, where in the dual-sided configuration, images are collected from two perpendicular views, which can be computationally merged to generate a high-quality 3D dataset with isotropic resolution. Two ORCA-Flash4.0 v.3 sCMOS cameras (Hamamatsu) are mounted at the end of each detection path. These cameras are ideal for LSFM, where speed, low noise and rolling shutter capability are key features to obtain high quality images.
The ct-dSPIM's modularity and open system architecture, which supports both proprietary and open-source software like Micro-Manager, make it a very versatile tool for researchers when 3D imaging of large samples and high resolution are required.

*Figure 46. The ct-dSPIM light-sheet microscope in use at CBClab.*

During the period spent at the CBClab, the system was re-assembled and re-aligned. Human brain samples were used to optimize the image while adjusting the alignment optical components.
CellX multi-wavelength laser and SuperK supercontinuum lasers were investigated for stability and power output. The measurements were performed with a PM100USB power meter (Thorlabs) connected to a S120C power sensor (Thorlabs). The optical fiber output was secured to the power sensor. The power output stability was monitored and recorded over a 3 hours period for all laser lines at their maximum and minimum power values. The SuperK was tested for the same laser lines included in the CellX.
All lasers, including the supercontinuum, resulted stable, with an average fluctuation within 2%. However, the maximum power output of the SuperK laser, 15mW for the 638 nm wavelength, resulted sub-ideal for imaging specimens stained with low quantum yield fluorophores. The other laser lines of the SuperK could output a maximum power of only 5mW.
The CellX revealed to be a suitable choice for imaging due to its stability and high power output (up to 70mW).

The ct-dSPIM is capable of imaging in confocal slit modality, but that has never been tested in the past. The camera shutter has been set to global in previous imaging sessions. Consequently, enabling imaging in confocal-slit modality significantly improved image quality in terms of SBR. The system management software, a Micro-Manager plugin, was designed to adjust the synchronization of the camera and the light-sheet beam to achieve a digitally-scanned light-sheet.
A comparison of the two modalities, global shutter and confocal slit, showed a relevant improvement of SBR when imaging human brain tissue stained with Neutral Red marking neurons (Figure 47).

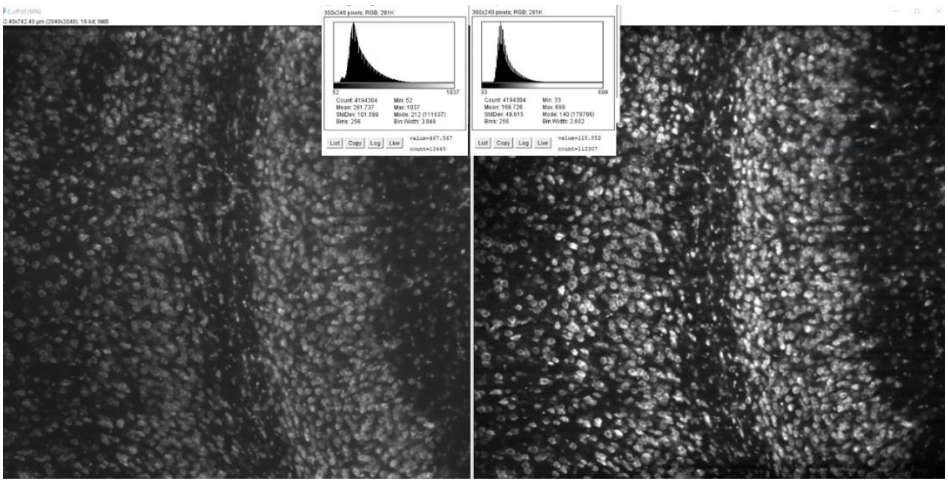

*Figure 47. A frame acquired in global shutter modality (left) and a frame of the same area acquired in confocal-slit mode (right), showing a significative improvement in SBR.*

The experience at CBClab has been fundamental to improve the understanding of LSFM, and to gain fundamental practical knowledge of aligning methods and laser parameters measurement which have been of great importance in the realization of this project.

# 6. Conclusions

This doctoral project has successfully introduced a novel quad-SPIM microscope, which represents a significant advancement in light-sheet fluorescence microscopy technology. The quad-SPIM system has demonstrated remarkable improvements in imaging speed, resolution, and multicolor capabilities, making it an essential tool for large-scale studies of human brain samples at cellular resolution.

The primary performance enhancement of the quad-SPIM system is its 12-fold increase in imaging speed compared to the dual-SPIM setup previously used by the Department. This speed boost enables volumetric imaging at a rate of 2.1 $cm^3/h$ in four colors, vastly outperforming the

previous rate of 0.17 $cm^3/h$. This rapid acquisition is especially critical for imaging large and complex brain samples, reducing the time needed for data collection while maintaining the system's high spatial resolution. This efficiency opens up new opportunities for large-scale studies in neuroscience, particularly those involving mapping neural circuits and investigating neurodegenerative diseases.

Another key feature of the quad-SPIM system is its ability to image in four colors simultaneously in an innovative way. This capability significantly enhances the system's versatility in studying multiple biomarkers within the same sample, facilitating complex biological studies such as tracing neuronal pathways or assessing the interactions between different cell types in brain tissues. Additionally, the system's lateral resolution ranging from $2.6 \pm 0.31$ μm to $3.9 \pm 0.25$ μm, combined with its axial resolution, ranging from $5.9 \pm 0.25$ μm to $8.7 \pm 0.58$ μm, allows for single-cell imaging even in relatively thick samples, providing critical insights into brain architecture at both cellular and subcellular levels.

Compared to the dual-SPIM of LENS Department, the quad-SPIM provides a relevant improvement in acquisition speed, at the cost of a lower resolution, representing an ideal choice for structural or cytoarchitectural studies in large volumes of human brain. In fact, the dual-SPIM setup offers a higher resolution of $1.3 \pm 0.2$ μm and an axial resolution of $7.7 \pm 0.2$ μm, calculated for 561 nm excitation laser line.

A drawback of the single sided illumination-detection design is the impossibility of performing a fusion of the views from two sides to obtain isotropic resolution. The 45° dual-view design of the dual-SPIM allows this process, representing, jointly with its superior lateral resolution, an optimal imaging apparatus for more critical applications, where structures of interest are densely packed and maximum resolution is required to precisely resolve them.

The quad-SPIM microscope has proven to be effective in specific biological applications, such as analyzing fiber dispersion in brain tissue using tools like Foa3D. These applications highlight the system's potential to contribute to crucial research questions in brain structure and function.

Looking forward, the quad-SPIM system holds immense potential for future applications in both fundamental and translational research. Its enhanced speed and multicolor imaging capabilities make it a powerful tool for large-scale mapping projects, such as constructing cellular-resolution atlases of entire brain regions, which are critical for understanding brain connectivity and function. The system's ability to quickly image large samples also makes it suitable for studying neurodevelopmental processes and neurodegenerative diseases in detail, aiding in the development of new therapeutic approaches.

In addition, the system could be further enhanced by integrating additional laser lines and optimizing the light-sheet and detection objectives to achieve even higher resolution. Such advancements would allow researchers to probe deeper into brain tissues and study smaller structures, pushing the boundaries of what is possible in brain imaging. Moreover, by improving sample preparation methods and optimizing data processing pipelines, the quad-SPIM could become an indispensable tool for a wide range of disciplines, including oncology, developmental biology, and regenerative medicine.

In conclusion, the quad-SPIM microscope not only meets the current demands of large-scale, high-resolution imaging but also sets the stage for future innovations in brain research and beyond. Its ability to address complex biological questions in a fast and efficient manner will enhance our understanding of human brain structure and function, providing new insights that could have profound implications for neuroscience and related fields.

# References


‘3D Imaging at the Speed of Life with SCAPE Microscopy | Coherent’. n.d. Accessed 17 August 2024. https://www.coherent.com/web-resources/article/neuroscience-3d-imaging-at-speed-of-life.

Amat, Fernando, Burkhard Höckendorf, Yinan Wan, William C. Lemon, Katie McDole, and Philipp J. Keller. 2015. ‘Efficient Processing and Analysis of Large-Scale Light-Sheet Microscopy Data’. *Nature Protocols* 10 (11): 1679–96. https://doi.org/10.1038/nprot.2015.111.

‘Anionic Nanoplastic Contaminants Promote Parkinson’s Disease–Associated α-Synuclein Aggregation | Science Advances’. n.d. Accessed 17 September 2024. https://www.science.org/doi/10.1126/sciadv.adi8716.

‘Author Spotlight: Advancing 3D Cytoarchitecture Analysis - Rapid Volumetric Reconstruction of the Human Brain’. n.d. Accessed 14 October 2024. https://app.jove.comAuthor Spotlight: Advancing 3D Cytoarchitecture Analysis - Rapid Volumetric Reconstruction of the Human Brain.

Azaripour, Adriano, Tonny Lagerweij, Christina Scharfbillig, Anna Elisabeth Jadczak, Britt van der Swaan, Manon Molenaar, Rens van der Waal, et al. 2018. ‘Three-Dimensional Histochemistry and Imaging of Human Gingiva’. *Scientific Reports* 8 (1): 1647. https://doi.org/10.1038/s41598-018-19685-4.

Baatsen, Pieter, Sergio Gabarre, Katlijn Vints, Rosanne Wouters, Dorien Vandael, Rose Goodchild, Sebastian Munck, and Natalia V. Gounko. 2021. ‘Preservation of Fluorescence Signal and Imaging Optimization for Integrated Light and Electron Microscopy’. *Frontiers in Cell and Developmental Biology* 9 (December). https://doi.org/10.3389/fcell.2021.737621.

Battistella, Eliana, Juan F. Quintana, and Gail McConnell. 2022. ‘Application of Light-Sheet Mesoscopy to Image Host-Pathogen Interactions in Intact Organs’. *Frontiers in Cellular and Infection Microbiology* 12 (June). https://doi.org/10.3389/fcimb.2022.903957.

Baumgart, Eugen, and Ulrich Kubitscheck. 2012. ‘Scanned Light Sheet Microscopy with Confocal Slit Detection’. *Optics Express* 20 (19): 21805–14. https://doi.org/10.1364/OE.20.021805.

Bèchet, Nicholas B, Tekla M Kylkilahti, Bengt Mattsson, Martina Petrasova, Nagesh C Shanbhag, and Iben Lundgaard. 2020a. ‘Light Sheet Fluorescence Microscopy of Optically Cleared Brains for Studying the Glymphatic System’. *Journal of Cerebral Blood Flow & Metabolism* 40 (10): 1975–86. https://doi.org/10.1177/0271678X20924954.

Becker, Klaus, Saiedeh Saghafi, Marko Pende, Inna Sabdyusheva-Litschauer, Christian M. Hahn, Massih Foroughipour, Nina Jährling, and Hans-Ulrich

Dodt. 2019. ‘Deconvolution of Light Sheet Microscopy Recordings’. *Scientific Reports* 9 (1): 17625. https://doi.org/10.1038/s41598-019-53875-y.

Berthet, Béatrice, and Alexis Maizel. 2016. ‘Light sheet microscopy and live imaging of plants’. *Journal of Microscopy* 263 (2): 158–64. https://doi.org/10.1111/jmi.12393.

Blazquez-Llorca, L, M Miguéns, M Montero-Crespo, A Selvas, J Gonzalez-Soriano, E Ambrosio, and J DeFelipe. 2020. ‘3D Synaptic Organization of the Rat CA1 and Alterations Induced by Cocaine Self-Administration’. *Cerebral Cortex (New York, NY)* 31 (4): 1927–52. https://doi.org/10.1093/cercor/bhaa331.

Boothe, Tobias, Lennart Hilbert, Michael Heide, Lea Berninger, Wieland B Huttner, Vasily Zaburdaev, Nadine L Vastenhouw, Eugene W Myers, David N Drechsel, and Jochen C Rink. 2017. ‘A Tunable Refractive Index Matching Medium for Live Imaging Cells, Tissues and Model Organisms’. Edited by Clare M Waterman. *eLife* 6 (July):e27240. https://doi.org/10.7554/eLife.27240.

‘Brain Map - Brain-Map.Org’. n.d. Accessed 17 September 2024. https://portal.brain-map.org/.

Buckner, Eli, Chanae Ottley, Cranos Williams, Angels de Luis Balaguer, Charles E. Melvin, and Rosangela Sozzani. 2018. ‘Tracking Gene Expression via Light Sheet Microscopy and Computer Vision in Living Organisms’. *Annual International Conference of the IEEE Engineering in Medicine and Biology Society. IEEE Engineering in Medicine and Biology Society. Annual International Conference* 2018 (July):818–21. https://doi.org/10.1109/EMBC.2018.8512416.

Chakraborty, Tonmoy, Bingying Chen, Stephan Daetwyler, Bo-Jui Chang, Oliver Vanderpoorten, Etai Sapoznik, Clemens F. Kaminski, Tuomas P. J. Knowles, Kevin M. Dean, and Reto Fiolka. 2020. ‘Converting Lateral Scanning into Axial Focusing to Speed up Three-Dimensional Microscopy’. *Light: Science & Applications* 9 (1): 165. https://doi.org/10.1038/s41377-020-00401-9.

Checcucci, Curzio, Bridget Wicinski, Giacomo Mazzamuto, Marina Scardigli, Josephine Ramazzotti, Niamh Brady, Francesco S. Pavone, Patrick R. Hof, Irene Costantini, and Paolo Frasconi. 2024. ‘Deep Learning-Based Localization Algorithms on Fluorescence Human Brain 3D Reconstruction: A Comparative Study Using Stereology as a Reference’. *Scientific Reports* 14 (1): 14629. https://doi.org/10.1038/s41598-024-65092-3.

Chen, Bi-Chang, Wesley R. Legant, Kai Wang, Lin Shao, Daniel E. Milkie, Michael W. Davidson, Chris Janetopoulos, et al. 2014. ‘Lattice Light-Sheet Microscopy: Imaging Molecules to Embryos at High Spatiotemporal Resolution’. *Science (New York, N.Y.)* 346 (6208): 1257998. https://doi.org/10.1126/science.1257998.

Chen, Chin-Yi, Yen-Ting Liu, Chieh-Han Lu, Po-Yi Lee, Yun-Chi Tsai, Jyun-Sian Wu, Peilin Chen, and Bi-Chang Chen. 2019. 'The Applications of Lattice Light-Sheet Microscopy for Functional Volumetric Imaging of Hippocampal Neurons in a Three-Dimensional Culture System'. *Micromachines* 10 (9): 599. https://doi.org/10.3390/mi10090599.

Chen, Liting, Jiao Meng, Yao Zhou, Fang Zhao, Yifan Ma, Wenyang Feng, Xingyu Chen, et al. 2024. 'Efficient 3D Imaging and Pathological Analysis of the Human Lymphoma Tumor Microenvironment Using Light-Sheet Immunofluorescence Microscopy'. *Theranostics* 14 (1): 406–19. https://doi.org/10.7150/thno.86221.

Chhetri, Raghav K, Fernando Amat, Yinan Wan, Burkhard Höckendorf, William C Lemon, and Philipp J Keller. 2015. 'Whole-Animal Functional and Developmental Imaging with Isotropic Spatial Resolution'. *Nature Methods* 12 (12): 1171–78. https://doi.org/10.1038/nmeth.3632.

Chung, Kwanghun, Jenelle Wallace, Sung-Yon Kim, Sandhiya Kalyanasundaram, Aaron S. Andalman, Thomas J. Davidson, Julie J. Mirzabekov, et al. 2013. 'Structural and Molecular Interrogation of Intact Biological Systems'. *Nature* 497 (7449): 332–37. https://doi.org/10.1038/nature12107.

Colombo, Federico, Erienne G. Norton, and Emanuele Cocucci. 2021. 'Microscopy Approaches to Study Extracellular Vesicles'. *Biochimica et Biophysica Acta (BBA) - General Subjects*, Biogenic, Hybrid and Synthetic Vesicles, 1865 (4): 129752. https://doi.org/10.1016/j.bbagen.2020.129752.

Corsetti, Stella, Frank Gunn-Moore, and Kishan Dholakia. 2019. 'Light Sheet Fluorescence Microscopy for Neuroscience'. *Journal of Neuroscience Methods* 319 (May):16–27. https://doi.org/10.1016/j.jneumeth.2018.07.011.

Costantini, Irene, Jean-Pierre Ghobril, Antonino Paolo Di Giovanna, Anna Letizia Allegra Mascaro, Ludovico Silvestri, Marie Caroline Müllenbroich, Leonardo Onofri, et al. 2015. 'A Versatile Clearing Agent for Multi-Modal Brain Imaging'. *Scientific Reports* 5 (1): 9808. https://doi.org/10.1038/srep09808.

Costantini, Irene, Danila Di Meo, Josephine Ramazzotti, Franco Cheli, Michele Sorelli, Giacomo Mazzamuto, Curzio Checcucci, Paolo Frasconi, and Francesco Saverio Pavone. 2024. 'Light-Sheet Fluorescence Microscopy for 3D Reconstruction of Human Brain'. In *Optica Biophotonics Congress: Biomedical Optics 2024 (Translational, Microscopy, OCT, OTS, BRAIN) (2024), Paper BW3C.4*, BW3C.4. Optica Publishing Group. https://doi.org/10.1364/BRAIN.2024.BW3C.4.

Costantini, Irene, Leah Morgan, Jiarui Yang, Yael Balbastre, Divya Varadarajan, Luca Pesce, Marina Scardigli, Giacomo Mazzamuto, Vladislav Gavryusev, Filippo Maria Castelli, et al. 2023. 'A Cellular Resolution Atlas of Broca's

Area'. *Science Advances*, October. https://doi.org/10.1126/sciadv.adg3844.
Costantini, Irene, Jean-Pierre Ghobril, Antonino Paolo Di Giovanna, Anna Letizia Allegra Mascaro, Ludovico Silvestri, Marie Caroline Müllenbroich, Leonardo Onofri, et al. 2015. 'A Versatile Clearing Agent for Multi-Modal Brain Imaging'. *Scientific Reports* 5 (1): 9808. https://doi.org/10.1038/srep09808.
Costantini, Irene, Danila Di Meo, Josephine Ramazzotti, Franco Cheli, Michele Sorelli, Giacomo Mazzamuto, Curzio Checcucci, Paolo Frasconi, and Francesco Saverio Pavone. 2024. 'Light-Sheet Fluorescence Microscopy for 3D Reconstruction of Human Brain'. In *Optica Biophotonics Congress: Biomedical Optics 2024 (Translational, Microscopy, OCT, OTS, BRAIN) (2024), Paper BW3C.4*, BW3C.4. Optica Publishing Group. https://doi.org/10.1364/BRAIN.2024.BW3C.4.
Costantini, Irene, Leah Morgan, Jiarui Yang, Yael Balbastre, Divya Varadarajan, Luca Pesce, Marina Scardigli, Giacomo Mazzamuto, Vladislav Gavryusev, Filippo Maria Castelli, et al. 2023. 'A Cellular Resolution Atlas of Broca's Area'. *Science Advances*, October. https://doi.org/10.1126/sciadv.adg3844.
Daetwyler, Stephan, and Reto Paul Fiolka. 2023. 'Light-Sheets and Smart Microscopy, an Exciting Future Is Dawning'. *Communications Biology* 6 (1): 1–11. https://doi.org/10.1038/s42003-023-04857-4.
Dando, Malcolm R. 2020. 'The EU Human Brain Project'. In *Neuroscience and the Problem of Dual Use: Neuroethics in the New Brain Research Projects*, edited by Malcolm R. Dando, 75–93. Cham: Springer International Publishing. https://doi.org/10.1007/978-3-030-53790-6_5.
Dean, Kevin M., Tonmoy Chakraborty, Stephan Daetwyler, Gerard Garrelts, Ons M'Saad, Hannahmariam T. Mekbib, Fabian F. Voigt, et al. 2022. 'Isotropic Imaging Across Spatial Scales with Axially Swept Light-Sheet Microscopy'. *Nature Protocols* 17 (9): 2025–53. https://doi.org/10.1038/s41596-022-00706-6.
Desmaison, Annaïck, Corinne Lorenzo, Jacques Rouquette, Bernard Ducommun, and Valérie Lobjois. 2013. 'A Versatile Sample Holder for Single Plane Illumination Microscopy'. *Journal of Microscopy* 251 (2): 128–32. https://doi.org/10.1111/jmi.12051.
'Detailed Atlases of the Human, Monkey, Rat and Mouse Brain - Brain Atlases'. n.d. EBRAINS. Accessed 17 September 2024. https://www.ebrains.eu/brain-atlases/reference-atlases/.
Di Meo, Danila, Josephine Ramazzotti, Marina Scardigli, Franco Cheli, Luca Pesce, Niamh Brady, Giacomo Mazzamuto, Irene Costantini, and Francesco S. Pavone. 2024. 'Optical Clearing and Labeling for Light-Sheet Fluorescence Microscopy in Large-Scale Human Brain Imaging'. *Journal of Visualized Experiments: JoVE*, no. 203 (January). https://doi.org/10.3791/65960.

Dodt, Hans-Ulrich, Ulrich Leischner, Anja Schierloh, Nina Jährling, Christoph Peter Mauch, Katrin Deininger, Jan Michael Deussing, Matthias Eder, Walter Zieglgänsberger, and Klaus Becker. 2007. 'Ultramicroscopy: Three-Dimensional Visualization of Neuronal Networks in the Whole Mouse Brain'. *Nature Methods* 4 (4): 331–36. https://doi.org/10.1038/nmeth1036.

Dyer, Laura, Andrew Parker, Keanu Paphiti, and Jeremy Sanderson. 2022. 'Lightsheet Microscopy'. *Current Protocols* 2 (7): e448. https://doi.org/10.1002/cpz1.448.

Elash, B., A. Bourassa, Paul Loewen, N. Lloyd, and D. Degenstein. 2015. 'The Aerosol Limb Imager: Acousto-Optic Imaging of Limb Scattered Sunlight for Stratospheric Aerosol Profiling'. *Atmospheric Measurement Techniques Discussions* 8 (December):13285–330. https://doi.org/10.5194/amtd-8-13285-2015.

Elgamal, Sara, Federico Colombo, Francesca Cottini, John C. Byrd, and Emanuele Cocucci. 2020. 'Chapter Five - Imaging Intercellular Interaction and Extracellular Vesicle Exchange in a Co-Culture Model of Chronic Lymphocytic Leukemia and Stromal Cells by Lattice Light-Sheet Fluorescence Microscopy'. In *Methods in Enzymology*, edited by Sheila Spada and Lorenzo Galluzzi, 645:79–107. Extracellular Vesicles. Academic Press. https://doi.org/10.1016/bs.mie.2020.06.015.

Ertürk, Ali, Klaus Becker, Nina Jährling, Christoph P. Mauch, Caroline D. Hojer, Jackson G. Egen, Farida Hellal, Frank Bradke, Morgan Sheng, and Hans-Ulrich Dodt. 2012. 'Three-Dimensional Imaging of Solvent-Cleared Organs Using 3DISCO'. *Nature Protocols* 7 (11): 1983–95. https://doi.org/10.1038/nprot.2012.119.

Fahrbach, Florian O., Vasily Gurchenkov, Kevin Alessandri, Pierre Nassoy, and Alexander Rohrbach. 2013. 'Light-Sheet Microscopy in Thick Media Using Scanned Bessel Beams and Two-Photon Fluorescence Excitation'. *Optics Express* 21 (11): 13824–39. https://doi.org/10.1364/OE.21.013824.

Fay, Michael P., and Michael A. Proschan. 2010. 'Wilcoxon-Mann-Whitney or t-Test? On Assumptions for Hypothesis Tests and Multiple Interpretations of Decision Rules'. *Statistics Surveys* 4:1. https://doi.org/10.1214/09-SS051.

Gibbs, Holly C., Sakina M. Mota, Nathan A. Hart, Sun Won Min, Alex O. Vernino, Anna L. Pritchard, Anindito Sen, et al. 2021. 'Navigating the Light-Sheet Image Analysis Software Landscape: Concepts for Driving Cohesion From Data Acquisition to Analysis'. *Frontiers in Cell and Developmental Biology* 9 (November). https://doi.org/10.3389/fcell.2021.739079.

Glaser, Adam, Kevin Bishop, Lindsey Barner, Robert Serafin, and Jonathan Liu. 2020. *A Hybrid Open-Top Light-Sheet Microscope for Multi-Scale Imaging of Cleared Tissues*. https://doi.org/10.1101/2020.05.06.081745.

Glaser, Adam K., Kevin W. Bishop, Lindsey A. Barner, Etsuo A. Susaki, Shimpei I. Kubota, Gan Gao, Robert B. Serafin, et al. 2022. 'A Hybrid Open-Top Light-Sheet Microscope for Versatile Multi-Scale Imaging of Cleared Tissues'.

*Nature Methods* 19 (5): 613–19. https://doi.org/10.1038/s41592-022-01468-5.

Glaser, Adam K., and Jonathan T. C. Liu. 2018. 'Pathology-Optimized Open-Top Light-Sheet Microscopy'. In *Biophotonics Congress: Biomedical Optics Congress 2018 (Microscopy/Translational/Brain/OTS) (2018), Paper MTu2A.4*, MTu2A.4. Optica Publishing Group. https://doi.org/10.1364/MICROSCOPY.2018.MTu2A.4.

Glaser, Adam K., Nicholas P. Reder, Ye Chen, Erin F. McCarty, Chengbo Yin, Linpeng Wei, Yu Wang, Lawrence D. True, and Jonathan T. C. Liu. 2017. 'Light-Sheet Microscopy for Slide-Free Non-Destructive Pathology of Large Clinical Specimens'. *Nature Biomedical Engineering* 1 (7): 1–10. https://doi.org/10.1038/s41551-017-0084.

Glaser, Adam K., Nicholas P. Reder, Ye Chen, Chengbo Yin, Linpeng Wei, Soyoung Kang, Lindsey A. Barner, et al. 2019. 'Multi-Immersion Open-Top Light-Sheet Microscope for High-Throughput Imaging of Cleared Tissues'. *Nature Communications* 10 (1): 2781. https://doi.org/10.1038/s41467-019-10534-0.

Greger, K., J. Swoger, and E. H. K. Stelzer. 2007. 'Basic Building Units and Properties of a Fluorescence Single Plane Illumination Microscope'. *Review of Scientific Instruments* 78 (2): 023705. https://doi.org/10.1063/1.2428277.

Hama, Hiroshi, Hiroyuki Hioki, Kana Namiki, Tetsushi Hoshida, Hiroshi Kurokawa, Fumiyoshi Ishidate, Takeshi Kaneko, et al. 2015. 'ScaleS: An Optical Clearing Palette for Biological Imaging'. *Nature Neuroscience* 18 (10): 1518–29. https://doi.org/10.1038/nn.4107.

Hampson, Karen M., Raphaël Turcotte, Donald T. Miller, Kazuhiro Kurokawa, Jared R. Males, Na Ji, and Martin J. Booth. 2021. 'Adaptive Optics for High-Resolution Imaging'. *Nature Reviews Methods Primers* 1 (1): 1–26. https://doi.org/10.1038/s43586-021-00066-7.

Haydo, Alicia, Andrej Wehle, Christel Herold-Mende, Donat Kögel, Francesco Pampaloni, and Benedikt Linder. 2023. 'Combining Organotypic Tissue Culture with Light-Sheet Microscopy (OTCxLSFM) to Study Glioma Invasion'. *EMBO Reports* 24 (12): e56964. https://doi.org/10.15252/embr.202356964.

Hedde, Per Niklas, Brian T. Le, Erika L. Gomez, Leora Duong, Robert E. Steele, and Siavash Ahrar. 2023. 'SPIM-Flow: An Integrated Light Sheet and Microfluidics Platform for Hydrodynamic Studies of Hydra'. *Biology* 12 (1): 116. https://doi.org/10.3390/biology12010116.

Hedde, Per Niklas, Leonel Malacrida, Siavash Ahrar, Albert Siryaporn, and Enrico Gratton. 2017. 'sideSPIM – Selective Plane Illumination Based on a Conventional Inverted Microscope'. *Biomedical Optics Express* 8 (August):1007–9. https://doi.org/10.1364/BOE.8.003918.

Hellinger, E., 1909. Neue Begründung der Theorie quadratischer Formen von unendlichvielen Veränderlichen. Journal für die reine und angewandte Mathematik 1909, 210–271.

Hillman, Elizabeth M. C., Venkatakaushik Voleti, Wenze Li, and Hang Yu. 2019. 'Light-Sheet Microscopy in Neuroscience'. *Annual Review of Neuroscience* 42 (July):295–313. https://doi.org/10.1146/annurev-neuro-070918-050357.

'How to Measure Resolution? Part Two!' n.d. *@abberior.Rocks* (blog). Accessed 17 October 2024. https://abberior.rocks/knowledge-base/how-to-measure-resolution-part-two/.

Hu, Bihe, Daniel Bolus, and J. Quincy Brown. 2018. 'Dual-View Inverted Selective Plane Illumination Microscopy (diSPIM) with Improved Background Rejection for Accurate 3D Digital Pathology'. In *Three-Dimensional and Multidimensional Microscopy: Image Acquisition and Processing XXV*, 10499:48–55. SPIE. https://doi.org/10.1117/12.2290785.

Huisken, Jan, Jim Swoger, Filippo Del Bene, Joachim Wittbrodt, and Ernst H. K. Stelzer. 2004. 'Optical Sectioning Deep Inside Live Embryos by Selective Plane Illumination Microscopy'. *Science* 305 (5686): 1007–9. https://doi.org/10.1126/science.1100035.

Jain, Akanksha, Gilles Gut, Fátima Sanchis-Calleja, Ryoko Okamoto, Simon Streib, Zhisong He, Fides Zenk, et al. 2023. 'Morphodynamics of Human Early Brain Organoid Development'. bioRxiv. https://doi.org/10.1101/2023.08.21.553827.

Jiang, Tao, Hui Gong, and Jing Yuan. 2023. 'Whole-Brain Optical Imaging: A Powerful Tool for Precise Brain Mapping at the Mesoscopic Level'. *Neuroscience Bulletin* 39 (12): 1840–58. https://doi.org/10.1007/s12264-023-01112-y.

Johnson, G. Allan, Yuqi Tian, David G. Ashbrook, Gary P. Cofer, James J. Cook, James C. Gee, Adam Hall, et al. 2023. 'Merged Magnetic Resonance and Light Sheet Microscopy of the Whole Mouse Brain'. *Proceedings of the National Academy of Sciences* 120 (17): e2218617120. https://doi.org/10.1073/pnas.2218617120.

Jung, Kyesam, Esther Florin, Kaustubh R Patil, Julian Caspers, Christian Rubbert, Simon B Eickhoff, and Oleksandr V Popovych. 2023. 'Whole-Brain Dynamical Modelling for Classification of Parkinson's Disease'. *Brain Communications* 5 (1): fcac331. https://doi.org/10.1093/braincomms/fcac331.

Kairišs, Kristaps, Natalia Sokolova, Lucie Zilova, Christina Schlagheck, Robert Reinhardt, Tilo Baumbach, Tomáš Faragó, Thomas van de Kamp, Joachim Wittbrodt, and Venera Weinhardt. 2023. 'Visualisation of Gene Expression within the Context of Tissues: An X-Ray Computed Tomography-Based Multimodal Approach'. bioRxiv. https://doi.org/10.1101/2023.10.09.561491.

Ke, Meng-Tsen, Satoshi Fujimoto, and Takeshi Imai. 2013. 'SeeDB: A Simple and Morphology-Preserving Optical Clearing Agent for Neuronal Circuit Reconstruction'. *Nature Neuroscience* 16 (8): 1154–61. https://doi.org/10.1038/nn.3447.

Keller, Philipp J., Annette D. Schmidt, Joachim Wittbrodt, and Ernst H.K. Stelzer. 2008. 'Reconstruction of Zebrafish Early Embryonic Development by Scanned Light Sheet Microscopy'. *Science* 322 (5904): 1065–69. https://doi.org/10.1126/science.1162493.

Kingston, Benjamin R., Abdullah Muhammad Syed, Jessica Ngai, Shrey Sindhwani, and Warren C. W. Chan. 2019. 'Assessing Micrometastases as a Target for Nanoparticles Using 3D Microscopy and Machine Learning'. *Proceedings of the National Academy of Sciences of the United States of America* 116 (30): 14937–46. https://doi.org/10.1073/pnas.1907646116.

Kirschenbaum, Daniel, Ehsan Dadgar-Kiani, Francesca Catto, Fabian F. Voigt, Chiara Trevisan, Oliver Bichsel, Hamid Shirani, et al. 2023. 'Whole-Brain Microscopy Reveals Distinct Temporal and Spatial Efficacy of Anti-Aβ Therapies'. *EMBO Molecular Medicine* 15 (1): e16789. https://doi.org/10.15252/emmm.202216789.

Kugler, Elisabeth C., Andrik Rampun, Timothy J. A. Chico, and Paul A. Armitage. 2020. 'Segmentation of the Zebrafish Brain Vasculature from Light Sheet Fluorescence Microscopy Datasets'. bioRxiv. https://doi.org/10.1101/2020.07.21.213843.

Kumar, Abhishek, Yicong Wu, Ryan Christensen, Panagiotis Chandris, William Gandler, Evan McCreedy, Alexandra Bokinsky, et al. 2014. 'Dual-View Plane Illumination Microscopy for Rapid and Spatially Isotropic Imaging'. *Nature Protocols* 9 (11): 2555. https://doi.org/10.1038/nprot.2014.172.

Laroche, Thierry, Olivier Burri, Lalit Kumar Dubey, and Arne Seitz. 2019. 'Development of Sample-Adaptable Holders for Lightsheet Microscopy'. *Frontiers in Neuroanatomy* 13 (March). https://doi.org/10.3389/fnana.2019.00026.

Lee, Hyunsu, Jae-Hyung Park, Incheol Seo, Sun-Hyun Park, and Shin Kim. 2014. 'Improved Application of the Electrophoretic Tissue Clearing Technology, CLARITY, to Intact Solid Organs Including Brain, Pancreas, Liver, Kidney, Lung, and Intestine'. *BMC Developmental Biology* 14 (1): 48. https://doi.org/10.1186/s12861-014-0048-3.

Lee, Suk Hyun, and Hye Joo Son. 2023. 'Second Wave, Late-Stage Neuroinflammation in Cleared Brains of Aged 5xFAD Alzheimer's Mice Detected by Macrolaser Light Sheet Microscopy Imaging'. *International Journal of Molecular Sciences* 24 (23): 17058. https://doi.org/10.3390/ijms242317058.

Li, Yusha, Jianyi Xu, Peng Wan, Tingting Yu, and Dan Zhu. 2018. 'Optimization of GFP Fluorescence Preservation by a Modified uDISCO Clearing Protocol'.

*Frontiers in Neuroanatomy* 12 (August). https://doi.org/10.3389/fnana.2018.00067.

Liebmann, Thomas, Nicolas Renier, Karima Bettayeb, Paul Greengard, Marc Tessier-Lavigne, and Marc Flajolet. 2016. 'Three-Dimensional Study of Alzheimer's Disease Hallmarks Using the iDISCO Clearing Method'. *Cell Reports* 16 (4): 1138–52. https://doi.org/10.1016/j.celrep.2016.06.060.

Lim, Diana H., Jeffrey LeDue, Majid H. Mohajerani, Matthieu P. Vanni, and Timothy H. Murphy. 2013. 'Optogenetic Approaches for Functional Mouse Brain Mapping'. *Frontiers in Neuroscience* 7 (April). https://doi.org/10.3389/fnins.2013.00054.

Linsley, Jeremy W., Terry Reisine, and Steven Finkbeiner. 2024. 'Three Dimensional and Four Dimensional Live Imaging to Study Mechanisms of Progressive Neurodegeneration'. *Journal of Biological Chemistry* 300 (7): 107433. https://doi.org/10.1016/j.jbc.2024.107433.

Luo, Xueting, Benjamin Yungher, and Kevin K. Park. 2014. 'Application of Tissue Clearing and Light Sheet Fluorescence Microscopy to Assess Optic Nerve Regeneration in Unsectioned Tissues'. *Methods in Molecular Biology (Clifton, N.J.)* 1162:209–17. https://doi.org/10.1007/978-1-4939-0777-9_17.

Machacova, Simona, Helena Chmelova, Anna Vavrova, Zbynek Kozmik, and Iryna Kozmikova. 2021. 'Optical Clearing and Light Sheet Microscopy Imaging of Amphioxus'. *Frontiers in Cell and Developmental Biology* 9 (July). https://doi.org/10.3389/fcell.2021.702986.

Marcos-Vidal, Asier, and Jorge Ripoll. 2020. 'Recent Advances in Optical Tomography in Low Scattering Media'. *Optics and Lasers in Engineering* 135 (December):106191. https://doi.org/10.1016/j.optlaseng.2020.106191.

Mazzamuto, Giacomo, Ludovico Silvestri, Giuseppe Sancataldo, Vladislav Gavryusev, Marina Scardigli, Irene Costantini, and Francesco S. Pavone. 2023. 'High-Speed Light-Sheet Microscopy Imaging and Data Post-Processing Using Custom Hardware and Software Solutions'. In *Three-Dimensional and Multidimensional Microscopy: Image Acquisition and Processing XXX*, 12385:10–15. SPIE. https://doi.org/10.1117/12.2650374.

Medeiros, Gustavo de, Raphael Ortiz, Petr Strnad, Andrea Boni, Franziska Moos, Nicole Repina, Ludivine Challet Meylan, Francisca Maurer, and Prisca Liberali. 2022. 'Multiscale Light-Sheet Organoid Imaging Framework'. *Nature Communications* 13 (1): 4864. https://doi.org/10.1038/s41467-022-32465-z.

Migliori, Bianca, Malika S. Datta, Christophe Dupre, Mehmet C. Apak, Shoh Asano, Ruixuan Gao, Edward S. Boyden, Ola Hermanson, Rafael Yuste, and Raju Tomer. 2018. 'Light Sheet Theta Microscopy for Rapid High-Resolution Imaging of Large Biological Samples'. *BMC Biology* 16 (1): 57. https://doi.org/10.1186/s12915-018-0521-8.

Moore, Regan P., Ellen C. O'Shaughnessy, Yu Shi, Ana T. Nogueira, Katelyn M. Heath, Klaus M. Hahn, and Wesley R. Legant. 2021. 'A Multi-Functional Microfluidic Device Compatible with Widefield and Light Sheet Microscopy'. *Lab on a Chip* 22 (1): 136–47. https://doi.org/10.1039/D1LC00600B.

Murray, Evan, Jae Hun Cho, Daniel Goodwin, Taeyun Ku, Justin Swaney, Sung-Yon Kim, Heejin Choi, et al. 2015. 'Simple, Scalable Proteomic Imaging for High-Dimensional Profiling of Intact Systems'. *Cell* 163 (6): 1500–1514. https://doi.org/10.1016/j.cell.2015.11.025.

Mzinza, David Twapokera, Henrike Fleige, Kristin Laarmann, Stefanie Willenzon, Jasmin Ristenpart, Julia Spanier, Gerd Sutter, Ulrich Kalinke, Peter Valentin-Weigand, and Reinhold Förster. 2018. 'Application of Light Sheet Microscopy for Qualitative and Quantitative Analysis of Bronchus-Associated Lymphoid Tissue in Mice'. *Cellular & Molecular Immunology* 15 (10): 875–87. https://doi.org/10.1038/cmi.2017.150.

Neckel, Peter H., Ulrich Mattheus, Bernhard Hirt, Lothar Just, and Andreas F. Mack. 2016. 'Large-Scale Tissue Clearing (PACT): Technical Evaluation and New Perspectives in Immunofluorescence, Histology and Ultrastructure'. *Scientific Reports* 6 (1): 34331. https://doi.org/10.1038/srep34331.

Olarte, Omar E., Jordi Andilla, Emilio J. Gualda, and Pablo Loza-Alvarez. 2018. 'Light-Sheet Microscopy: A Tutorial'. *Advances in Optics and Photonics* 10 (1): 111–79. https://doi.org/10.1364/AOP.10.000111.

Paiè, Petra, Rebeca Martinez Vazquez, Roberto Osellame, Francesca Bragheri, and Andrea Bassi. 2018. 'Microfluidic Based Optical Microscopes on Chip'. *Cytometry Part A* 93 (September). https://doi.org/10.1002/cyto.a.23589.

Parker, Ian, Katrina T. Evans, Kyle Ellefsen, Devon A. Lawson, and Ian F. Smith. 2017. 'Lattice Light Sheet Imaging of Membrane Nanotubes between Human Breast Cancer Cells in Culture and in Brain Metastases'. *Scientific Reports* 7 (1): 11029. https://doi.org/10.1038/s41598-017-11223-y.

Patel, Kripa B., Wenxuan Liang, Malte J. Casper, Venkatakaushik Voleti, Wenze Li, Alexis J. Yagielski, Hanzhi T. Zhao, et al. 2022. 'High-Speed Light-Sheet Microscopy for the in-Situ Acquisition of Volumetric Histological Images of Living Tissue'. *Nature Biomedical Engineering* 6 (5): 569–83. https://doi.org/10.1038/s41551-022-00849-7.

Pawłowska, Monika, Diana Legutko, and Marzena Stefaniuk. 2017. '[Getting an insight into the brain - new optical clearing techniques and imaging using light-sheet microscope]'. *Postepy Biochemii* 63 (1): 8–15.

Pesce, Luca, Pietro Ricci, Giancarlo Sportelli, Nicola Belcari, and Giuseppe Sancataldo. 2024. 'Expansion and Light-Sheet Microscopy for Nanoscale 3D Imaging'. *Small Methods*, March, e2301715. https://doi.org/10.1002/smtd.202301715.

Pesce, Luca, Marina Scardigli, Vladislav Gavryusev, Annunziatina Laurino, Giacomo Mazzamuto, Giuseppe Sancataldo, Ludovico Silvestri, et al. 2022. 'SHORT: A Human Brain Tissue Clearing and Labeling Protocol for 3D Recostruction with LSFM', November. https://www.protocols.io/view/short-a-human-brain-tissue-clearing-and-labeling-p-bysqpwdw.

Photonics, Adam Glaser and Jonathon Liu, University of Washington, Nicolas Reder, Light Speed Micro, Melissa Haahr, Cobolt, a part of HÜBNER. n.d. 'Light Sheet Microscopy Enables 3D Pathology'. Accessed 13 September 2024. https://www.photonics.com/Articles/Light_Sheet_Microscopy_Enables_3D_Pathology/a66546.

Poola, Praveen Kumar, Muhammad Imran Afzal, Youngseung Yoo, Ki Hean Kim, and Euiheon Chung. 2019. 'Light Sheet Microscopy for Histopathology Applications'. *Biomedical Engineering Letters* 9 (3): 279–91. https://doi.org/10.1007/s13534-019-00122-y.

Power, Rory M., and Jan Huisken. 2017. 'A Guide to Light-Sheet Fluorescence Microscopy for Multiscale Imaging'. *Nature Methods* 14 (4): 360–73. https://doi.org/10.1038/nmeth.4224.

'Protocol for Integrating Tissue Clearing and Light-Sheet Imaging to Analyze Cancer Initiation in Mosaic Analysis with Double Markers Mouse Models'. n.d. Accessed 13 September 2024. https://star-protocols.cell.com/protocols/3501.

Remacha, Elena, Lars Friedrich, Julien Vermot, and Florian O. Fahrbach. 2020. 'How to Define and Optimize Axial Resolution in Light-Sheet Microscopy: A Simulation-Based Approach'. *Biomedical Optics Express* 11 (1): 8–26. https://doi.org/10.1364/BOE.11.000008.

Renier, Nicolas, Eliza L. Adams, Christoph Kirst, Zhuhao Wu, Ricardo Azevedo, Johannes Kohl, Anita E. Autry, et al. 2016. 'Mapping of Brain Activity by Automated Volume Analysis of Immediate Early Genes'. *Cell* 165 (7): 1789–1802. https://doi.org/10.1016/j.cell.2016.05.007.

Reynaud, Emmanuel G., Uroš Kržič, Klaus Greger, and Ernst H. K. Stelzer. 2008. 'Light Sheet-based Fluorescence Microscopy: More Dimensions, More Photons, and Less Photodamage'. *HFSP Journal* 2 (5): 266–75. https://doi.org/10.2976/1.2974980.

Richardson, Douglas S., and Jeff W. Lichtman. 2015. 'Clarifying Tissue Clearing'. *Cell* 162 (2): 246–57. https://doi.org/10.1016/j.cell.2015.06.067.

Rieckher, Matthias. 2017. 'Light Sheet Microscopy to Measure Protein Dynamics'. *Journal of Cellular Physiology* 232 (1): 27–35. https://doi.org/10.1002/jcp.25451.

Rierola, Marina, Nataliya I. Trushina, Michael Holtmannspötter, Rainer Kurre, and Lidia Bakota. 2023. 'Lattice Light-Sheet Microscopy and Evaluation of Dendritic Transport in Cultured Hippocampal Tissue Reveal High

Variability in Mobility of the KIF1A Motor Domain and Entry into Dendritic Spines'. *Brain Research Bulletin* 194 (March):13–22. https://doi.org/10.1016/j.brainresbull.2022.12.012.

Rocha, Mariana Diales, Daniel Normen Düring, Philipp Bethge, Fabian F. Voigt, Staffan Hildebrand, Fritjof Helmchen, Alexander Pfeifer, Richard Hans Robert Hahnloser, and Manfred Gahr. 2019. 'Tissue Clearing and Light Sheet Microscopy: Imaging the Unsectioned Adult Zebra Finch Brain at Cellular Resolution'. *Frontiers in Neuroanatomy* 13 (February). https://doi.org/10.3389/fnana.2019.00013.

Rosario, Alexandra, Ashley Howell, and Sanjoy K. Bhattacharya. 2022. 'A Revisit to Staining Reagents for Neuronal Tissues'. *Annals of Eye Science* 7 (March):6. https://doi.org/10.21037/aes-21-31.

Rosch, Richard E., Paul R. Hunter, Torsten Baldeweg, Karl J. Friston, and Martin P. Meyer. 2018. 'Calcium Imaging and Dynamic Causal Modelling Reveal Brain-Wide Changes in Effective Connectivity and Synaptic Dynamics during Epileptic Seizures'. *PLOS Computational Biology* 14 (8): e1006375. https://doi.org/10.1371/journal.pcbi.1006375.

Russell, C.t., and E.j. Rees. 2020. 'An Open-Hardware Sample Mounting Solution for Inverted Light-Sheet Microscopes with Large Detection Objective Lenses'. *Journal of Microscopy* 280 (1): 63–68. https://doi.org/10.1111/jmi.12940.

Salwig, Isabelle, Birgit Spitznagel, Marion Wiesnet, and Thomas Braun. 2021. 'Imaging Lung Regeneration by Light Sheet Microscopy'. *Histochemistry and Cell Biology* 155 (2): 271–77. https://doi.org/10.1007/s00418-020-01903-8.

Santi, Peter A. 2011. 'Light Sheet Fluorescence Microscopy: A Review'. *Journal of Histochemistry & Cytochemistry* 59 (2): 129–38. https://doi.org/10.1369/0022155410394857.

Sorelli, Michele, Irene Costantini, Leonardo Bocchi, Markus Axer, Francesco Saverio Pavone, and Giacomo Mazzamuto. 2023. 'Fiber Enhancement and 3D Orientation Analysis in Label-Free Two-Photon Fluorescence Microscopy'. *Scientific Reports* 13 (March):4160. https://doi.org/10.1038/s41598-023-30953-w.

Spangenberg, Philippa, Nina Hagemann, Anthony Squire, Nils Förster, Sascha D. Krauß, Yachao Qi, Ayan Mohamud Yusuf, et al. 2023. 'Rapid and Fully Automated Blood Vasculature Analysis in 3D Light-Sheet Image Volumes of Different Organs'. *Cell Reports Methods* 3 (3). https://doi.org/10.1016/j.crmeth.2023.100436.

Sparks, Hugh, Lucas Dent, Chris Bakal, Axel Behrens, Guillaume Salbreux, and Chris Dunsby. 2020. 'Dual-View Oblique Plane Microscopy (dOPM)'. *Biomedical Optics Express* 11 (12): 7204–20. https://doi.org/10.1364/BOE.409781.

Swoger, Jim, Peter Verveer, Klaus Greger, Jan Huisken, and Ernst H. K. Stelzer. 2007. 'Multi-View Image Fusion Improves Resolution in Three-Dimensional Microscopy'. *Optics Express* 15 (13): 8029–42. https://doi.org/10.1364/OE.15.008029. 3.042.

Swoger, Jim, Peter Verveer, Klaus Greger, Jan Huisken, and Ernst H. K. Stelzer. 2007. 'Multi-View Image Fusion Improves Resolution in Three-Dimensional Microscopy'. *Optics Express* 15 (13): 8029–42. https://doi.org/10.1364/OE.15.008029.

Tainaka, Kazuki, Shimpei I. Kubota, Takeru Q. Suyama, Etsuo A. Susaki, Dimitri Perrin, Maki Ukai-Tadenuma, Hideki Ukai, and Hiroki R. Ueda. 2014. 'Whole-Body Imaging with Single-Cell Resolution by Tissue Decolorization'. *Cell* 159 (4): 911–24. https://doi.org/10.1016/j.cell.2014.10.034.

Takanezawa, Sota, Takashi Saitou, and Takeshi Imamura. 2021. 'Wide Field Light-Sheet Microscopy with Lens-Axicon Controlled Two-Photon Bessel Beam Illumination'. *Nature Communications* 12 (1): 2979. https://doi.org/10.1038/s41467-021-23249-y.

Tian, Ting, Zhaoyang Yang, and Xiaoguang Li. 2021. 'Tissue Clearing Technique: Recent Progress and Biomedical Applications'. *Journal of Anatomy* 238 (2): 489–507. https://doi.org/10.1111/joa.13309.

Tomer, Raju, Khaled Khairy, Fernando Amat, and Philipp J. Keller. 2012. 'Quantitative High-Speed Imaging of Entire Developing Embryos with Simultaneous Multiview Light-Sheet Microscopy'. *Nature Methods* 9 (7): 755–63. https://doi.org/10.1038/nmeth.2062.

Truong, Thai, Willy Supatto, David Koos, John Choi, and Scott Fraser. 2011. 'Deep and Fast Live Imaging with Two-Photon Scanned Light-Sheet Microscopy'. *Nature Methods* 8 (July):757–60. https://doi.org/10.1038/nmeth.1652.

Ueda, Hiroki R., Hans-Ulrich Dodt, Pavel Osten, Michael N. Economo, Jayaram Chandrashekar, and Philipp J. Keller. 2020. 'Whole-Brain Profiling of Cells and Circuits in Mammals by Tissue Clearing and Light-Sheet Microscopy'. *Neuron* 106 (3): 369–87. https://doi.org/10.1016/j.neuron.2020.03.004.

Ueda, Hiroki R., Ali Ertürk, Kwanghun Chung, Viviana Gradinaru, Alain Chédotal, Pavel Tomancak, and Philipp J. Keller. 2020a. 'Tissue Clearing and Its Applications in Neuroscience'. *Nature Reviews. Neuroscience* 21 (2): 61. https://doi.org/10.1038/s41583-019-0250-1.

Uhlén, Per, and Nobuyuki Tanaka. 2018. 'Improved Pathological Examination of Tumors with 3D Light-Sheet Microscopy'. *Trends in Cancer* 4 (5): 337–41. https://doi.org/10.1016/j.trecan.2018.03.003.

Vieites-Prado, Alba, and Nicolas Renier. 2021. 'Tissue Clearing and 3D Imaging in Developmental Biology'. *Development (Cambridge, England)* 148 (18): dev199369. https://doi.org/10.1242/dev.199369.

Vito, Giuseppe de, Lapo Turrini, Caroline Müllenbroich, Pietro Ricci, Giuseppe Sancataldo, Giacomo Mazzamuto, Natascia Tiso, et al. 2022. 'Fast Whole-Brain Imaging of Seizures in Zebrafish Larvae by Two-Photon Light-Sheet Microscopy'. *Biomedical Optics Express* 13 (3): 1516–36. https://doi.org/10.1364/BOE.434146.
Vito, Giuseppe de, Lapo Turrini, Caroline Müllenbroich, Pietro Ricci, Giuseppe Sancataldo, Giacomo Mazzamuto, Natascia Tiso, et al. 2022. 'Fast Whole-Brain Imaging of Seizures in Zebrafish Larvae by Two-Photon Light-Sheet Microscopy'. *Biomedical Optics Express* 13 (3): 1516–36. https://doi.org/10.1364/BOE.434146.
Vladimirov, Nikita, Yu Mu, Takashi Kawashima, Davis Bennett, Chao-Tsung Yang, Loren Looger, Philipp Keller, Jeremy Freeman, and Misha Ahrens. 2014. 'Light-Sheet Functional Imaging in Fictively Behaving Zebrafish'. *Nature Methods* 11 (July). https://doi.org/10.1038/nmeth.3040.

Vladimirov, Nikita, Fabian F. Voigt, Thomas Naert, Gabriela R. Araujo, Ruiyao Cai, Anna Maria Reuss, Shan Zhao, et al. 2024. 'Benchtop mesoSPIM: A next-Generation Open-Source Light-Sheet Microscope for Cleared Samples'. *Nature Communications* 15 (1): 2679. https://doi.org/10.1038/s41467-024-46770-2.

Wang, Feifei, Zhuoran Ma, Yeteng Zhong, Felix Salazar, Chun Xu, Fuqiang Ren, Liangqiong Qu, Anna M. Wu, and Hongjie Dai. 2021. 'In Vivo NIR-II Structured-Illumination Light-Sheet Microscopy'. *Proceedings of the National Academy of Sciences* 118 (6): e2023888118. https://doi.org/10.1073/pnas.2023888118.

Weigelin, Bettina, Gert-Jan Bakker, and Peter Friedl. 2012. 'Intravital Third Harmonic Generation Microscopy of Collective Melanoma Cell Invasion: Principles of Interface Guidance and Microvesicle Dynamics'. *IntraVital* 1 (1): 32–43. https://doi.org/10.4161/intv.21223.

'Whole-Brain Microscopy Reveals Distinct Temporal and Spatial Efficacy of Anti-Aβ Therapies - PubMed'. n.d. Accessed 17 September 2024. https://pubmed.ncbi.nlm.nih.gov/36382364/.

Wu, Yicong, Peter Wawrzusin, Justin Senseney, Robert S Fischer, Ryan Christensen, Anthony Santella, Andrew G York, et al. 2013. 'Spatially Isotropic Four-Dimensional Imaging with Dual-View Plane Illumination Microscopy'. *Nature Biotechnology* 31 (11): 1032–38. https://doi.org/10.1038/nbt.2713.

Xu, Na, Amin Tamadon, Yaan Liu, Tong Ma, Rehana K. Leak, Jun Chen, Yanqin Gao, and Yi Feng. 2017. 'Fast Free-of-Acrylamide Clearing Tissue (FACT)—an Optimized New Protocol for Rapid, High-Resolution Imaging of Three-Dimensional Brain Tissue'. *Scientific Reports* 7 (1): 9895. https://doi.org/10.1038/s41598-017-10204-5.

Zaeck, Luca M., David Scheibner, Julia Sehl, Martin Müller, Donata Hoffmann, Martin Beer, Elsayed M. Abdelwhab, Thomas C. Mettenleiter, Angele

Breithaupt, and Stefan Finke. 2021. 'Light Sheet Microscopy-Assisted 3D Analysis of SARS-CoV-2 Infection in the Respiratory Tract of the Ferret Model'. *Viruses* 13 (3): 529. https://doi.org/10.3390/v13030529.

Zhang, Zhouzhou, Xiao Yao, Xinxin Yin, Zhangcan Ding, Tianyi Huang, Yan Huo, Runan Ji, Hanchuan Peng, and Zengcai V. Guo. 2021. 'Multi-Scale Light-Sheet Fluorescence Microscopy for Fast Whole Brain Imaging'. *Frontiers in Neuroanatomy* 15 (September). https://doi.org/10.3389/fnana.2021.732464.

Zhou, Xiangda, Renping Zhao, Archana K. Yanamandra, Markus Hoth, and Bin Qu. 2022a. 'Light-Sheet Scattering Microscopy to Visualize Long-Term Interactions Between Cells and Extracellular Matrix'. *Frontiers in Immunology* 13 (January):828634. https://doi.org/10.3389/fimmu.2022.828634.